Modal testing using high speed digital speckle pattern interferometry

Steven Earl

Submitted for the degree of Doctor of Philosophy

Heriot-Watt University

School of Engineering and Physical Sciences

November 2014

Abstract

This thesis introduces the application of a high-speed speckle pattern interferometer (SPI) to perform quantified impact modal testing. The interferometer acts as a non-contact multipoint vibrometer that removes the mass-loading effects of contact transducers to improve measurement accuracy and decreases measurement time by the use of multiple measurement points. A temporal phase-stepped CMOS high-speed SPI system was used to capture the transient vibration response of two overlapping plates, the system had a maximum surface velocity of 1.4 mm/s and the results were compared to accelerometer data and correlated against a finite element model. To extend the surface velocity to 2.7 mm/s a spatial phase-stepped CMOS SPI system was used and compared to the finite element model. Both the temporal phase-stepped system and the spatial phase-stepped system showed high performance for quantified modal testing: showing high correlation for the natural frequencies and the modal assurance criterion correlated over 60% for the first six modes of vibration. The interferometer was improved by the application of spatial phase-stepping but was still limited by the maximum measurable velocity. The thesis also applied the SPI to the novel measurement of traveling waves on a centre-clamped disc. Traveling waves can be caused by structural problems or damage and are difficult to measure without the ability to capture the relative phase across multiple points. This was achieved through the spatial phase-stepped CMOS SPI system and the traveling waves were excited on the disc through a frequency modulated signal that excited the degenerate modes that occurred within 1 Hz of the disc's second resonant frequency. The multipoint system identified the waveshape, direction and was able to show the ratio of standing wave to traveling wave in the measurements.

Acknowledgements

I would like to thank my supervisor Prof. Andrew Moore for his support during this research. His direction and advice on this work has helped get this to the quality it is and what it needed to be.

Dr. Tao Wu deserves my highest gratitude for his advice and knowledge of SPI systems that was critical to the experimental work in this thesis. Also Dr. Jesus Valera for all his help in the lab and for his patience in explaining fundamentals of optics that widened my knowledge of the research area. Thank you.

Finally, I would like to thank my family and friends who have provided their support, warmth and humour over the course of my work on this thesis. Without this emotional support and encouragement it would not be in its final form. They know who they are and I thank them greatly.

ACADEMIC REGISTRY
Research Thesis Submission

Name*:*	Steven Earl		
School/PGI:	EPS		
Version: *(i.e. First, Resubmission, Final)*	**Final**	Degree Sought (Award **and** Subject area)	PhD

Declaration

In accordance with the appropriate regulations I hereby submit my thesis and I declare that:

1) the thesis embodies the results of my own work and has been composed by myself
2) where appropriate, I have made acknowledgement of the work of others and have made reference to work carried out in collaboration with other persons
3) the thesis is the correct version of the thesis for submission and is the same version as any electronic versions submitted*.
4) my thesis for the award referred to, deposited in the Heriot-Watt University Library, should be made available for loan or photocopying and be available via the Institutional Repository, subject to such conditions as the Librarian may require
5) I understand that as a student of the University I am required to abide by the Regulations of the University and to conform to its discipline.

* *Please note that it is the responsibility of the candidate to ensure that the correct version of the thesis is submitted.*

Signature of Candidate*:*		Date:	

Submission

Submitted By *(name in capitals):*	STEVEN EARL
Signature of Individual Submitting:	
Date Submitted:	

For Completion in the Student Service Centre (SSC)

Received in the SSC by *(name in capitals):*			
Method of Submission *(Handed in to SSC; posted through internal/external mail):*			
*E-thesis Submitted (**mandatory for final theses)***			
Signature:		Date:	

Please note this form should bound into the submitted thesis.

Updated February 2008, November 2008, February 2009, January 2011

Contents

1 Introduction **1**

1.1 Background to the project 1

1.2 Organisation of the thesis 2

2 Literature Review **3**

2.1 Modal testing 3

2.1.1 Single degree of freedom 4

2.1.2 Multiple degrees of freedom 6

2.1.3 Modal testing 10

2.2 Laser transducers for vibration measurement 17

2.2.1 Laser Doppler vibrometers 18

2.2.2 Speckle pattern interferometry 24

2.2.3 Laser transducers to measure traveling waves 32

2.3 Chapter summary 35

3 Modal testing using HSSPI with temporal phase-stepping **37**

3.1 Experimental system 37

3.2 Simulation work 42

3.3 Sound pulse excitation 45

3.3.1 Test setup for acoustic excitation 45

3.3.2 Single frequency excitation 46

3.3.3 Pulse excitation 48

3.4 Test object for modal testing 50

3.4.1 Accelerometer tests and results 51

3.4.2 Multipoint vibrometer tests and results 53

3.5 Discussion 56

3.6 Chapter summary 57

4 Modal testing using HSSPI with spatial phase-stepping **59**

4.1 Experimental system for experiments 59

4.1.1 Binary grating alignment 63
4.2 Simulation work 64
4.3 Test object for modal testing 69
4.4 Results 70
4.5 Discussion 73
4.6 Chapter summary 75

5 HSSPI application to measuring traveling waves 76
5.1 Background to traveling waves 77
5.2 Simulation work 79
5.3 Experimental system for experiments 92
5.4 Results 92
5.4.1 Single frequency excitation 92
5.4.2 Frequency modulation excitation 97
5.5 Discussion 105
5.6 Chapter summary 106

6 Conclusion and Future work 107
6.1 Future work 108

Appendices 109

A Orthogonality and mass-normalisation of modal parameters 110

B Measurement points 115

C FM signal sidebands 116

Glossary of terms

$\alpha(\omega)$	Receptance Frequency Response Function
$\alpha_{jk}(\omega)$	Receptance at location/mode j, k
Φ	Mass normalised modeshape / eigenvector
A	Region A
B	Region B
$\bar{A}$	Mean intensity from region A
$\bar{B}$	Mean intensity from region B
Δ	Relative phase difference between object and reference beam
η	Interferometer sensitivity factor
η_r	Damping factor for the r^{th} mode
γ_O	Visibility of the speckle modulation
λ	Wavelength of laser
λ_K	Wavelength of traveling wave
ω	Frequency
ω_c	Carrier frequency
ω_{FM}	Modulation frequency
ω_r	Natural frequency for the r^{th} mode
Φ_O	The object phase
Φ_R	The reference phase
Ψ	The eigenvector for an undampded system,
$\{\psi\}_r$	The eigenvector for the r^{th} mode
ψ_O	Random speckle phase
Ψ_A	The analytical modeshape
Ψ_X	The experimental modeshape
θ	The angular position of a circular object
${}_rA_{jk}$	Modal Constant
D_a	Lens aperture diameter
f	Excitation frequency
h	Hysteric damping factor
I_O	Object bias intensity
K	Spatial wave number
k_r	Modal stiffness of mode r
m_r	Modal mass of mode r
ω_r	Resonant frequency of mode r
t_e	Frame exposure time
t_n	Time instant at frame n

V_{Nyq}	Nyquist velocity limit
w_+	Displacement a traveling wave in the clockwise direction
w_-	Displacement a traveling wave in the anti-clockwise direction
w_0	Vibration amplitude

List of publications

Conference papers

- S. Earl, T. Wu, J.D.C Jones, A.J. Moore, P. Daborn, A. Tribe, P. Hayden, P. Ind and G. Smith,
  "Impact testing with a high-speed multipoint vibrometer",
  IMAC-XXVI: Conference & Exposition on Structural Dynamics, 2008, Florida, USA. ISBN: 0-912053-98-4

- S. Earl, T. Wu, J. D. C. Jones and A. J. Moore,
  "High-speed multipoint vibrometer for modal analysis",
  Proc. SPIE 6345, Seventh International Conference on Vibration Measurements by Laser Techniques: Advances and Applications, 634512 (June 21, 2006), ISBN: 9780819464217

- S. Earl, T. Wu, J. D. C. Jones and A. J. Moore,
  "Modal analysis with a CMOS multipoint vibrometer",
  Photon 06 (Manchester) 87-88 (Institute of Physics, Bristol, 2006) No ISBN

Journal

- S. Earl, T. Wu, and A. J. Moore,
  "Impact modal testing with multipoint CMOS vibrometers"
  In preparation for submission to the Journal of Sound and Vibration:

  - Show results of complete impact modal testing using temporal phase-stepped HSSPI and spatial phase-stepped HSSPI.
  - Compared and correlated against accelerometer and a finite element model for both natural frequency and modal assurance criterion.

Chapter 1

Introduction

1.1 Background to the project

Modal analysis is an important technique that experimentally quantifies the dynamic properties of a structure, which can then help understand how to design structures with extended life-cycle and lower noise emissions. The dynamic properties can be extracted from a measure of the input excitation and the structure's response to this. The accuracy of the measured response directly affects the quality of the extracted dynamic properties. Established measurement techniques based on the use of contacting transducers need to be fixed to the surface of interest, which can affect the response of the structure through additional mass and stiffness, they are also typically single point measurements: so have poor spatial resolution meaning tests must be repeated over many measurement points. Laser Doppler vibrometers overcame these mass-loading effects and laser scanning devices have been used as a way of simplifying the movement between measurement points. However, these are still single point measurements requiring the time-consuming process of performing point-by-point measurements and critically cannot measure the relative phase between each measurement point. Full-field interferometers provide an alternative measurement technique, by providing high spatial resolution with no mass-loading but cannot provide the time-resolved measurements needed for some vibration testing conditions, due to their low sampling rates compared to vibration periods. With the use of high-speed cameras the temporal resolution can be increased with the sacrifice of some spatial resolution can extend the temporal resolution further and be resolved with the use of phase-stepping techniques. Implementation of CMOS high-speed cameras offer additional flexibility in the detector to rapidly switch between full-field measurements for high spatial resolution and then to smaller user-defined regions of interest that offer high temporal resolution for faster dynamic measurements.

This thesis extends the applications of CMOS high-speed speckle pattern interferometer (HSSPI) developed at Heriot-Watt University [1, 2] to perform quantified impact modal testing and exploits the parallel measurement ability to the detection and measurement of traveling waves.

1.2 Organisation of the thesis

Chapter 2 presents the background knowledge for this thesis, starting with an overview of modal analysis and its applications that are used as part of the experimental work in this thesis. There are a breadth of contact and non-contact vibration measurement transducers and so this thesis focuses on the development of laser techniques that are developing towards similar conclusions: a balance of temporal resolution and spatial resolution is essential for vibration measurement transducers. These laser techniques are laser Doppler vibrometry and speckle pattern interferometer (SPI) and the thesis focuses on their application to vibration measurement and modal testing. Finally an overview of how these techniques have been applied to the measurement of traveling waves are presented.

Applying the higher measurement abilities of HSSPI are demonstrated in Chapter 3 through the use of temporal phase-stepped HSSPI to perform impact modal testing of 2 plates overlapping at their edge. The response measurements are presented and are correlated against an FE model and accelerometer results to compare the quality and capability of temporal phase-stepping HSSPI. A discussion on the velocity limits and its effect on modal testing results are then discussed.

To overcome the velocity limits set by temporal phase-stepping, Chapter 4 demonstrates the use of spatial phase-stepping HSSPI to extend the system's dynamic range. Impact modal tests are performed on the same 2 overlapping plates as the temporal system and correlated against the FE model to show the benefits of the extended dynamic range, these results are presented and then discussed.

Chapter 5 demonstrates the application of the parallel multipoint ability of HSSPI to the measurement of traveling waves on a centred-clamped disc. The results show the direction and shape of the standing and traveling waves measured by HSSPI. The results are then discussed in comparison to other techniques for measuring traveling waves.

The conclusions of this thesis are presented in Chapter 6 providing an overview of the results in the following chapters and finishes with a discussion on the direction future research work could take.

Chapter 2

Literature Review

An overview of modal analysis is introduced to understand how vibration response data can be applied to create dynamic characteristic models of structures. The Chapter then leads to an overview of the different laser transducers and their applications to vibration analysis this focuses on laser Doppler vibrometry and speckle pattern interferometry. The developments and limitations of these laser systems are presented as are cases where they have been directly applied to successful modal testing. The applications of these techniques to identify and measure traveling waves are then discussed.

2.1 Modal testing

Most structures have an infinite number of natural frequencies that can be excited to produce a response in the structure. The frequency at which these occur are dependent on the physical characteristic of the structure: the shape and the internal properties, stiffness, mass, and damping. These characteristics also dictate the shape the vibration takes when excited at a particular natural frequency, known as the natural modeshape. The modern approach to understand how these vibration frequencies and modeshapes occur is to develop a combination of analytical modelling with field testing and to correlate them against each other. The field tests analysis are quantified using modal testing [3] which uses the vibration response data collected from experimental tests to then extract the modal properties of damping, natural frequencies and modeshapes. The modal model is then compared and correlated to the analytical model.

The rest of this Section introduces the parameters that are important to modal testing. An introduction of vibration as a single degree of freedom system and its properties are then expanded to introduce multi-degrees of freedom systems. This background then shows how it can be used to simplify the measurement of real structures that have infinite degrees of freedom. The modal testing process is then dis-

cussed, which includes different excitation methods, the process to extract modal properties and finally methods for correlation to enable the comparison to analytical models.

2.1.1 Single degree of freedom

Real life structures rarely fall into a single degree of freedom (SDOF) model, but the fundamental properties and characteristics of the SDOF approach can be scaled and coupled with other models to understand more complex structures. In this Section these characteristics are introduced and how they apply to modal analysis.

A SDOF system can be simplified to three components, a mass, a spring and a damper (MSD) seen in Figure 2.1. The MSD model has a mass, m, the spring a stiffness, k and a structural damping, h. In the cases considered here the damping characteristics of the structure are hysteric. This type of damping gives a closer representation of real structures when testing. Hysteric damping is independent of frequency for energy loss within the system [4] and provides the most simple solution for the extension of SDOF theory to multiple degrees of freedom theory for modal analysis.

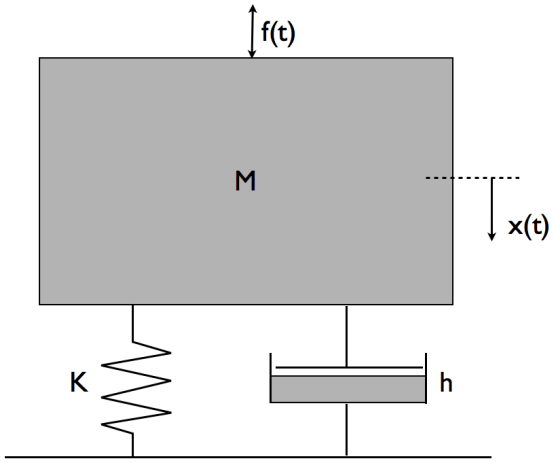

Figure 2.1: SDOF model showing components: Mass, Spring, Damper(MSD)

Assuming that for small deflections the spring will have a linear relationship between the force and displacement, and similarly the damper will have a linear relationship between force and velocity. For large deflections these assumptions cannot be made. The equation of motion for the MSD model seen in Figure 2.1, excited from an harmonic excitation force of f(t)=$Fe^{i\omega t}$ would have an expected system response of x(t) = $Xe^{i\omega t}$ and can be represented as [3]:

$$(-\omega^2 m + k + ih)Xe^{i\omega t} = Fe^{i\omega t} \tag{2.1}$$

where the structural damping, h, introduces a complex part, i, that adds phase correction to the velocity's phase so that is in-phase with the force's phase. As $\dot{X}e^{i\omega}$ can be seen as the differential equivalent of $i\omega Xe^{i\omega t}$ we can rearrange 2.1 to describe the equation of motion in terms of velocity by replacing X with $\dot{X}/(i\omega)$ giving:

$$(\omega^2 m + k + ih)\frac{\dot{X}e^{i\omega t}}{i\omega} = Fe^{i\omega t} \tag{2.2}$$

this can then be rearranged to give the velocity response per unit force, know as the frequency response function (FRF):

$$\frac{\dot{X}(\omega)}{F(\omega)} = Y(\omega) = \frac{i\omega}{k - m\omega^2 + ih} \tag{2.3}$$

The FRF is effectively a response model for a SDOF system where both the parameters velocity and force are complex to ensure both amplitude and relative phase information is retained. Having the FRF in terms of velocity is known as the mobility response function. Plotting the mobility against frequency can be seen in Figure 2.2, this shows the absolute response and phase. The peak seen in the figure is located at the frequency that gives the maximum system response, and this point is known as the system's resonant frequency. Another characteristic of the resonant frequency location is the 180 degree phase change at this frequency. Both these properties can be used to define a true natural frequency in a SDOF system. The width of the peak is a function of the damping present in the system - the higher the damping the wider the sideband of the peak, the lower the damping the thinner the sideband of the peak. Analysis can be performed on the SDOF system to extract the modal properties (natural frequencies, modeshape, damping and modal constant). This can be achieved from SDOF extraction techniques such as the circle fit methods and the line-fit methods [5] both of which use the real and imaginary parts of the response, these methods are discussed later in Section 2.1.3. SDOF provides a useful method to understand the properties of modal analysis and how they relate to each other. To understand how this approach can be used for modal testing this analysis must be extended to systems with multiple degrees of freedom.

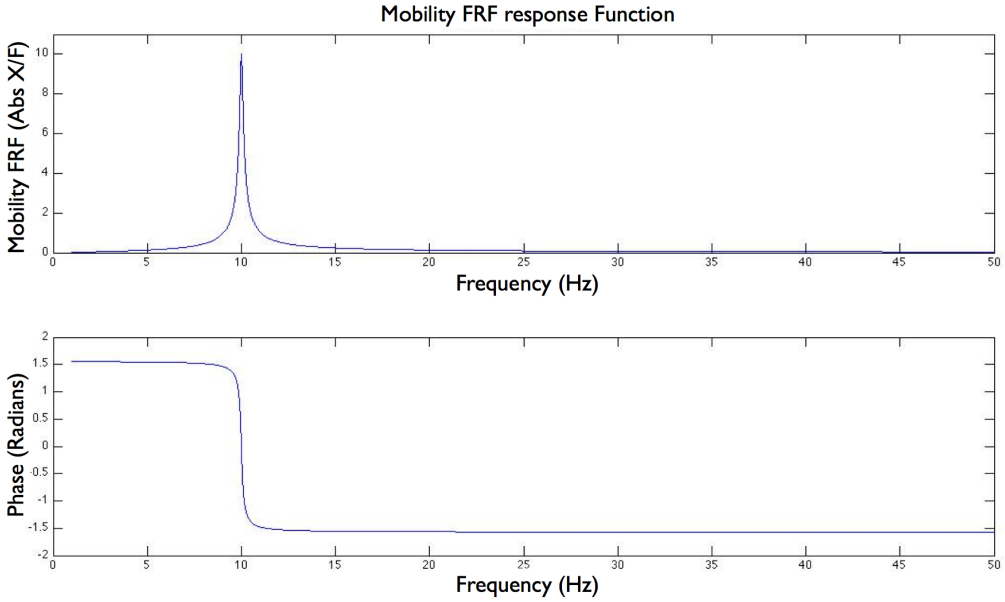

Figure 2.2: SDOF Mobility FRF, with m = 0.5, k = 50 and h = 1

2.1.2 Multiple degrees of freedom

The application of SDOF theory to multiple degrees of freedom systems (MDOF) vibration models, provides an opportunity to demonstrate how this concept can be used to analyse more complex structures. In this Section the SDOF model is used to create a two degree of freedom system model, that provides the basis to demonstrate a universal approach to MDOF modelling, used practically to perform modal testing.

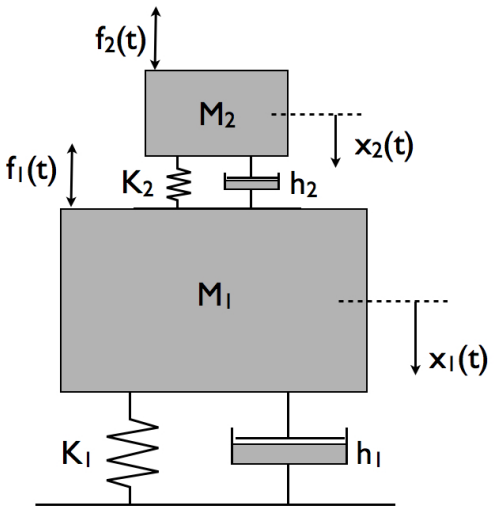

Figure 2.3: Two degree of freedom system diagram, including 2 mass elements(m_1,m_2), 2 spring systems (k_1,k_2) and 2 damping factors (h_1,h_2)

Figure 2.3 shows a two degree of freedom system where each part of the system has its own mass, m, stiffness, k, and damping, h, both parts are coupled together and therefore have an effect on each others movement. To understand how this system would respond to the forces, f_1 and f_2, the equations of motion must be formed [3]:

$$m_1\ddot{x}_1 + (h_1 + h_2)\dot{x}_1 - h_2\dot{x}_2 + (k_1 + k_2)x_1 - k_2x_2 = f_1 \tag{2.4}$$

$$m_2\ddot{x}_2 + h_2\dot{x}_2 - h_2\dot{x}_1 + k_2x_2 - k_2x_1 = f_2 \tag{2.5}$$

this can be represented in matrix form:

$$\begin{bmatrix} m_1 & 0 \\ 0 & m_2 \end{bmatrix} \begin{Bmatrix} \ddot{x}_1 \\ \ddot{x}_2 \end{Bmatrix} + \begin{bmatrix} h_1 + h_2 & -h_2 \\ -h_2 & h_2 \end{bmatrix} \begin{Bmatrix} \dot{x}_1 \\ \dot{x}_2 \end{Bmatrix} + \begin{bmatrix} k_1 + k_2 & -k_2 \\ -k_2 & k_2 \end{bmatrix} \begin{Bmatrix} x_1 \\ x_2 \end{Bmatrix} = \begin{Bmatrix} f_1 \\ f_2 \end{Bmatrix} \tag{2.6}$$

and then simplified into matrix notation:

$$[M]\{\ddot{x}\} + [H]\{\dot{x}\} + [K]\{x\} = \{F\}e^{i\omega t} \tag{2.7}$$

assuming harmonic excitation and with the same approach to SDOF hysteric damping in Equation 2.1 we can reproduce the matrices as below:

$$[M]\{\ddot{x}\} + i[H]\{x\} + [K]\{x\} = \{F\}e^{i\omega t} \tag{2.8}$$

Characteristics of the damped MDOF system can be achieved by considering the condition of no excitation, this produces a response solution in the form of:

$$x = Xe^{i\lambda t} \tag{2.9}$$

where the solution of λ can be complex; this solution substituted into Equation 2.8 leads to the complex eigensolution that form the two matrices that contain the eigenvectors and the eigenvalues. The r^{th} eigenvalue solution in its complex form can be described as:

$$\lambda_r^2 = \omega_r^2(1 + i\,\eta_r) \tag{2.10}$$

where ω_r is the natural frequency and η_r is the damping factor for the r^{th} mode. The eigensolution has the orthogonality properties whose solution can be seen in appendix A. The orthogonal properties imply that the modal vectors are linearly independent

and can be used in any vector space.

$$[\Psi]^T[M][\Psi] = [m_r] \quad ; \quad [\Psi]^T[[K + iH][\Psi] = [k_r] \tag{2.11}$$

Where $[\Psi]$ is the eigenvector matrix for the undampded system, which is equal to a damped system when damping is linearly proportional: The modal mass and the complex stiffness parameters are fully dependent on the normalisation of the eigenvalues and they must satisfy:

$$\lambda_r^2 = \frac{k_r}{m_r} \tag{2.12}$$

These are the same for the mass-normalised eigenvectors and their conditions:

$$\{\phi_r\} = (m_r)^{-1/2}\{\Psi\}_r \tag{2.13}$$

Now the general characteristic of MDOF system has been identified, these are used to develop an expression for a forced response. Assuming a harmonic excitation, the equation of motion based on the systems response as Equation 2.8 would produce:

$$\left([K] + i[H] - \omega^2[M]\right)\{X\}e^{i\,\omega t} = \{F\}e^{i\,\omega t} \tag{2.14}$$

This rearranged for the unknown response X:

$$\{X\}e^{i\omega t} = \left([K] + i[H] - \omega^2\,[M]\right)^{-1}\{F\}e^{i\omega t} \tag{2.15}$$

can take the form of the response function in terms of displacement (known as receptance)

$$\{X\} = [\alpha(\omega)]\,\{F\} \tag{2.16}$$

where $[\alpha(\omega)]$ is an NxN matrix of the receptance FRF and is the response model for the system. This matrix must satisfy the same principles of orthogonality demonstrated in appendix A as in Equation 2.11, to give:

$$[\alpha(\omega)] = [\Phi]\,[(\lambda_r^2 - \omega^2)]^{-1}\,[\Phi]^T \tag{2.17}$$

where each element of the matrix contains $\alpha_{jk}(\omega)$ that takes the form:

$$\alpha_{jk}(\omega) = \sum_{r=1}^{N} \frac{(\phi_{jr})\,(\phi_{kr})}{\omega_r^2 - \omega + i\,\eta_r\,\omega_r^2} \tag{2.18}$$

substituting Equation 2.13 into this, it takes the form:

$$\alpha_{jk}(\omega) = \sum_{r=1}^{N} \frac{(\Psi_{jr})\,(\Psi_{kr})}{m_r(\omega_r^2 - \omega + i\,\eta_r\,\omega_r^2)} \tag{2.19}$$

in this form it can be simplified to introduce a modal parameter, the modal constant ${}_rA_{jk}$

$$\alpha_{jk}(\omega) = \sum_{r=1}^{N} \frac{{}_rA_{jk}}{(\omega_r^2 - \omega + i\,\eta_r\,\omega_r^2)} \tag{2.20}$$

where the modal constant represents the contribution for the r^{th} mode from other modes in the system. To be consistent with our SDOF example we can represent the FRF in terms of velocity giving the mobility FRF as:

$$Y_{jk}(\omega) = i\,\omega\,\alpha_{jk}(\omega) = \sum_{r=1}^{N} \frac{i\,\omega\,{}_rA_{jk}}{(\omega_r^2 - \omega + i\,\eta_r\,\omega_r^2)} \tag{2.21}$$

This can be directly applied to the 2DOF example in Figure 2.1 by the choice of arbitrary parameters for the first mass, m_1=0.5 kg, stiffness, k_1=10 N/m and the structural, h_1=1 and for the second mass. m_2=0.25, stiffness, k_2=40 N/m, and structural damping h_2=1. It is possible to graphically represent the FRF using Equation 2.21 as seen in Figure 2.4. This shows the FRF system response of the 2 DOF in the solid blue line, showing the 2 natural frequencies of this system. To understand how the individual SDOF characteristics contribute to produce the the MDOF system, the equivalent SDOF model for m_1 is shown as the dashed red line and for m_2 the dashed green line.

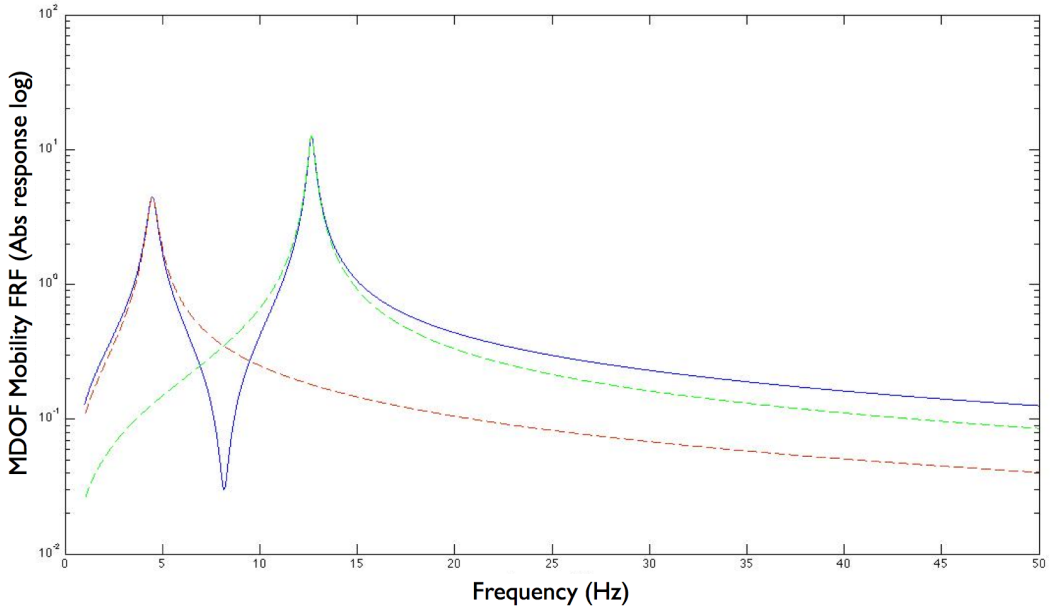

Figure 2.4: MDOF Mobility FRF, with m_1=0.5, k_1=10 and h_1=1; m_2=0.25, k_2=40, h_2=1. The solid Blue line is the FRF for the 2DOF system. the dashed red is the individual contribution from m_1 and the dashed green line is the contribution from m_2

Analysis of the MDOF was discussed to show how a matrix system can be developed to represent any system. This approach can be extended to include the measurement of engineering structures by using the measurement points of interest on the structure to capture the dynamic response. A measurement point can be seen as a single degree of freedom, that contributes to the response characteristics of the structure and to the structure's FRF matrix. As engineering structures in general have an infinite degree of freedom the challenge for the vibration engineer is finding the balance between capturing enough measurement points that sufficiently represent the structure whilst minimising measurement testing time.

2.1.3 Modal testing

Successful modal testing requires the measurement of the excitation force and the measurement of the system's response to this force (usually velocity, acceleration or displacement). This force and response can then be used to create a FRF matrix to represent the system's response model, which with the use of Equation 2.21 means that the system's modal parameters can be extracted.

For successful modal testing to take place, considerations of the type of excitation and the type of response measurement must be taken. It is then important to understand which modal parameter extraction techniques is to be used and how this data compares and correlates against existing theoretical models or other experimental response models.

Modal excitation

There are multiple ways to excite structures and these can be set into two groups: contact and non-contact. Non-contact methods include electromagnets and laser pulses [6, 7]. It is difficult to get an an exact and accurate measure of the input force from these methods, so they were not used for testing within this thesis and therefore are not discussed in detail here. The contact group include impact hammers and shakers that can be powered through electromagnetic, hydraulics and mechanical means.

The most common method for modal testing is through an electromagnetic shaker, where the shaker input signal is used to excite the magnetic field in a coil that then is used to power the drive part of the shaker, normally attached to the test structure. The input signal to the shaker can be a continuous signal (sinusoidal, random, sweeps) or transient (pulse, chirp, bursts) which can be produced from a signal generator and sent through an amplifier to power the shaker. The biggest benefit to using a shaker is the ability to control the input signal's frequency and amplitude, that provides a controlled and customisable approach to excitation. To have a measure of the force the shaker applies to the structure, a force transducer is attached to the structure using a rod known as a stinger. Trying to use the shaker above the resonance of its own excitation coils produces non-linear excitation of the force transmitted into the structure and therefore the shaker has a useful frequency range that testing must be applied within. This range can be overcome by choosing larger shakers.

Another popular method for contact modal testing is through the use of an impact hammer. This is classed as a contact device but the hammer contact with the surface is only at the moment of impact, meaning after the initial impact the test object vibrates freely. Impact hammers have the force transducer built into the hammer head to measure the force of the impact. The magnitude of the force is proportional to the mass of the head, the larger the mass, the higher the force that can be applied.

The duration of the impact is in part what defines the useful frequency range of this type of excitation [8, 9], the shorter the duration of the pulse the larger the frequency range that can be excited. The duration of the pulse is dictated by the stiffness of the hammer tip, where tips with high stiffness, such as metal, produce much shorter pulses than that of rubber and plastic. The hammer tests offer a fast way to perform modal testing over a range of frequencies and many measurement points, but the accuracy of the testing is based on the skill of the vibration engineer. The engineer needs experience to apply a force of approximately the same magnitude for each impact. This impact has to be low enough to stay clear of any non-linearities that can be introduced from high levels of impact force. Later in this thesis both hammer and shaker tests are used. The hammer was used in an attempt to get close

to free-vibration conditions for modal testing as possible and the shaker was used due its ability to control both frequency and amplitude of the excitation.

Regardless of the method used for modal excitation the key quantity needed is an accurate measurement of the force that can then be used with the system's measured response to extract the modal parameters.

Modal parameter extraction

The FRFs collected from modal testing have modal properties that can be extracted. These properties are known as the modal parameters and include the resonant frequency, the modal constant and the damping factor. To extract these parameters from experimental data mathematical curve fitting and extraction techniques are applied to the data. These extraction techniques are then used to build a modal model that describes the dynamic properties of the test object. Modal extraction methods generally fall into either SDOF or MDOF techniques, which both have their appropriate applications and benefits. This Section provides an overview of techniques used in this thesis for modal analysis and outlines their benefits and their limitations.

SDOF curve fitting methods SDOF methods have the benefits of high accuracy for each individual mode and are essential in cases of close modes to be analysed, the two most popular techniques are discussed here, known as the circle fit method and the line fit method.

The circle fit method: The circle fit method exploits the form the FRF takes when plotted on the complex plane as seen in Figure 2.5, which plots the 2DOF system from the previous Section (Figure 2.4). Plotting the FRF on the complex plane forms a circle for each DOF in the system. The curve fitting process fits a circle to the data points and uses the point of maximum absolute response to identify the resonant frequency. The damping is calculated with an iterative approach, which identifies linearities between frequency points either side of the resonant frequency as a function of the resonant frequency. If the tests were performed within the linear limits of modal testing, this value should be constant across all ranges of the iterations and the constant value is the damping factor. Finally the modal constant is calculated from the diameter of the circle fit. This process is then repeated for every mode to be analysed in the system. This approach is particularly useful when the modes to be analysed are close to each other or the analysis requires manual input from the engineer. This method is used for modal analysis in Chapter 4.

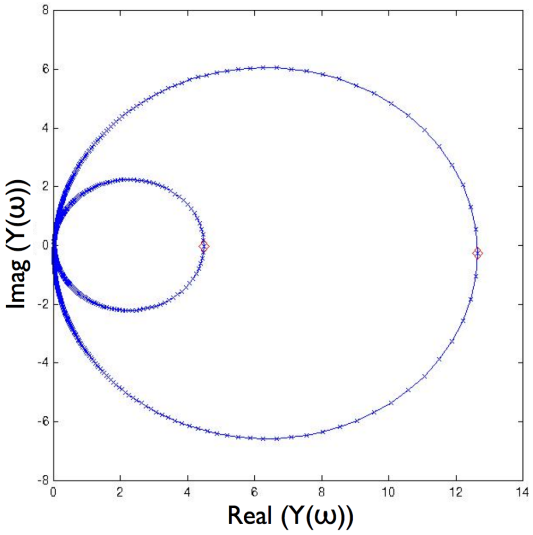

Figure 2.5: Nyquist plot of 2DOF from Figure 2.4, the blue crosses represent frequency points, the 2 red markers indicate the 2 natural frequencies of the system

The line fit / inverse fit method: Line fit method uses a similar approach to the circle fit method but uses the reciprocal of the SDOF FRF (Equation 2.3), which when plotted on the complex plane produces a straight-line. The method fits to the experimental data and where the data intersects the imaginary axis (where the real part is zero) identifies the damping factor. The process then curve fits the deviation of the real part to the theoretical reciprocal FRF to extract the mass and the stiffness, used to identify the resonant frequency. This approach is best for situations of real modes and not when the modes are far apart, typically at least 6 data points above and below the resonant frequency without using any data points that are on other resonant modes. Again this approach is then repeated for every mode to be analysed. This approach is used to validate the circle fit estimations in Chapter 4.

The long analysis time required for each mode and then again for each FRF (over hundreds of FRFs for some testing) needed to be analysed means that other approaches for large amounts of data are required.

MDOF curve fitting methods MDOF approaches provide much faster analysis to extract both multiple mode parameter extraction and multiple FRFs at the same time. Its approach is useful for structures that have closely coupled modes, where contributions from the other modes would be missed form SDOF analysis. In practice a combination of both SDOF and MDOF need to be used as a way to provide confidence in the analysis process.

Non-Linear least-square fit method: NLLS expresses the FRF as a series of partial fractions to be solved as an iterative optimisation process, the solutions of the coefficients from the partial fractions give the modal parameters. As with most

iterative methods, this process needs a good initial estimate of the parameter locations to be successful, provided through user interaction of the method.

Rational fraction polynomial: RFP is the most used method for modal extraction. It treats the FRF as a rational expression that can be expressed as a fraction polynomial series. The solution to this series leads to the formation of a linear set of equations, that solved provide the modal parameters. The approach provides rapid extraction for multiple FRFs however requires many repeat analyses and checks to ensure accuracy and to identify computational assumptions that create non-existent results.

Another method for lightly damped structures uses series expansion curve fitting that uses an undamped FRF expression as the weighting factor. This approach is used for systems that have very low damping factors and not used in this thesis but is mentioned for completeness.

Both NLLS and RFP MDOF methods were used in Chapter 3 to identify the modal parameters, this was supported by the circle fit method to valid modal parameters that were analysed.

Correlation of modal data

Modern computer aided engineering software and finite element (FE) packages are highly capable of predicting a structure's theoretical vibration response model. Modal testing is used to complement this activity by providing field data of the actual structure to build a modal model. Therefore there is a need to compare the theoretical and experimental results in a quantifiable way that is representable of both sets of models, this is known as correlation. Correlation is normally performed on the natural frequencies and the modeshapes of a structure; the natural frequencies to ensure both models responses occur within the same excitation ranges; the modeshape to understand how the modal parameters (damping, stiffness and modal constant) of the models contribute to the movement at each frequency. Both correlations are needed to ensure there is no systematic errors in the theoretical modelling or the testing. Doing only one correlation can provide misleading confidence as a high correlation in natural frequencies does not automatically give a high correlation in modeshape.

An overview of the two correlation types, natural frequency excitation and modal assurance criterion are given below.

Natural frequency correlation: The natural frequency correlation gives the degree of correlation of the natural frequency data between the theoretical and experimental datasets. It is not just the comparison of the frequency by frequency values, but uses the correlated mode pairs (CMP). This gives a more representative correlation by only comparing frequencies that have similar or matching modal properties.

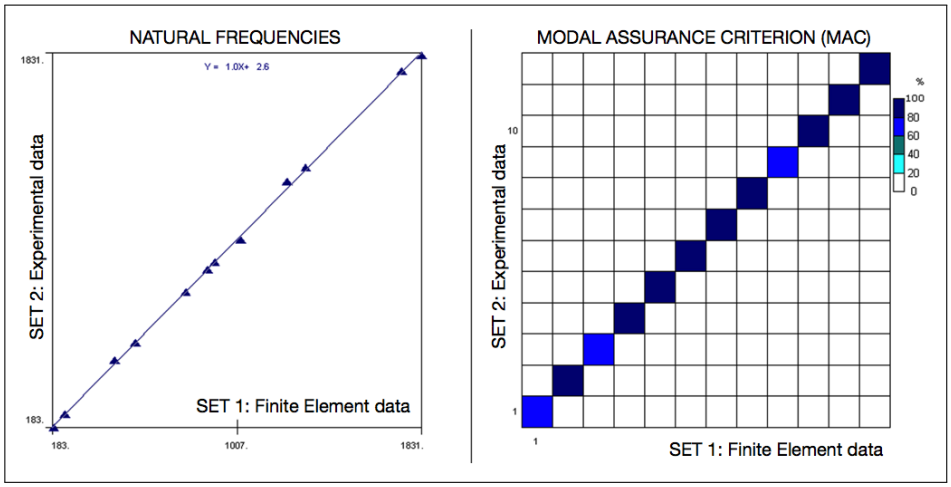

Figure 2.6: Example of correlation methods from experimental results from Chapter 3 captured with an accelerometer: (Left) Natural frequency correlation. (Right) Modal assurance criterion (MAC), Where set 1 is the experimental data and set 2 is the finite element data. Both data sets show what would be expected from well correlated data, the natural frequency comparison show all frequencies correlating on the gradient of 1 and the MAC results show all modes the gradient of 1 and high correlation of over 80% for each mode.

The correlation fits a best-fit line to the frequency pairs. A correlation result from accelerometer tests from Chapter 3 can be seen in graphical form in the left image of Figure 2.6. If the frequency pairs match perfectly then the slope of the straight line has a gradient of 1. If all the frequency pairs are close to the line-fit then it is considered to be a good correlation and if a high scatter from the best-fit it is considered a poor correlation. If the frequency pairs are close to the best-fit line but the gradient is not equal to 1, this is still considered good correlation but suggests a systematic problem in the test data or an assumption error in the theoretical model. The natural frequency correlation alone is not enough to know the root of the errors and assessment is usually complemented with the aid of the modal assurance criterion.

Modal assurance criterion: The modal assurance criterion (MAC) [10, 11] is one of the key types of correlation used in modal testing. It measures the linearity between two sets of paired modeshapes. A MAC is the general term that combines two parameters used to measure correlation, the modal scale factors (MSF) and the actual modal assurance criterion, where the correlation process gets its general name. The contribution of the first parameter, MSF, does not provide any indication of the quality of a fit to modes, but does give the slope of the correlation and is defined from:

$$MSF(X, A) = \frac{\sum_{j=1}^{n} (\Psi_X)_j (\Psi_A)_j^*}{\sum_{j=1}^{n} (\Psi_A)_j (\Psi_A)_j^*} \tag{2.22}$$

this is equally valid in an alternative form that uses the experimental data set as the reference set:

$$MSF(X,A) = \frac{\sum_{j=1}^{n}(\Psi_A)_j(\Psi_X)_j^*}{\sum_{j=1}^{n}(\Psi_X)_j(\Psi_X)_j^*} \tag{2.23}$$

where Ψ_A is the analytical modeshape and the Ψ_X defines the experimental modeshape, n defines the number of DOFs within the datasets. The $*$ indicates the complex conjugate. The second parameter is the MAC, which provides a measure of the least-squares deviation from the above slope. and can be defined by:

$$MAC(A,X) = \frac{|\sum_{j=1}^{n}(\Psi_A)_j(\Psi_X)_j^*|^2}{\left(\sum_{j=1}^{n}\left(\Psi_X\right\}_j\{\Psi_X\}_j^*\right)\right)\left(\sum_{j=1}^{n}\{\Psi_A\}_j\{\Psi_A\}_j^*\right)} \tag{2.24}$$

or written in terms of the finite data sets from modal testing

$$MAC(A,X) = \frac{\left|\{\Psi_X\}^T\{\Psi_A\}\right|^2}{\left(\{\Psi_X\}^T\{\Psi_X\}\right)\left(\{\Psi_A\}^T\{\Psi_A\}\right)} \tag{2.25}$$

This measurement produces a scalar quantity. When the modeshapes match perfectly (i.e. when Ψ_A=Ψ_X) the MAC (from Equation 2.25) provides a solution of 1 (100%) giving the highest correlation possible. A MAC is usually represented in graphical form as seen in the right image of the accelerometer data in Figure 2.6 taken from the experimental data in Chapter 3.

In practice errors may appear from the testing or the theoretical models so that a correlation above 90% is considered to be well correlated and above 80% as acceptable. Below 20% is considered non-correlation and less than 10% is judged to be no correlation at all. Errors can contribute to poor modal correlation and can come from a range of areas that include unexpected non-linearities in the test object, poor measurements and poor extraction of modal parameters, and errors from the assumptions made for the theoretical modelling. Figure 2.7A shows the MAC results when there is high correlation of where the frequencies of the mode shapes occur but poor correlation of the mode shapes themselves and B shows an example of when there is possible spatial aliasing in the results, non-linearities in the test structure, noise in the data or a poor choice of DOF in the correlation.

The MAC can also be used before modal testing as a planning tool, where the MAC properties are used to find optimal sensor locations (to avoid spatial aliasing of measured data) and give an accurate estimate of the minimum number of measurement points for a valid test [12]. Using the MAC as a planning tool can lead to reduced testing times and more accurate test data. Both the natural frequency corre-

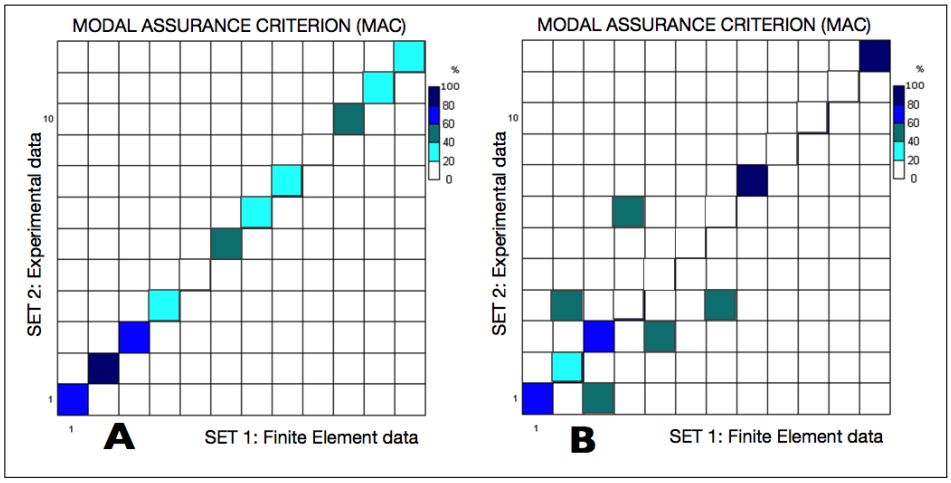

Figure 2.7: A) a MAC where the mode shapes occur at similar frequencies but poor shape correlation. B) a Mac showing an example of how the data may look with common data problems. Both images are graphical reconstructions and not from real data

lation and MAC are used to assess the quality of the experimental data in Chapters 3 and 4.

2.2 Laser transducers for vibration measurement

Vibration measurement technology can be grouped into contact and non-contact devices. Contact devices include accelerometers [13], contact vibrometers [13] and strain gauges [14], all of which need to be physically attached to a surface where the vibrations is to be measured. This contact can introduce errors through surface coupling where the bonding / attachment to the surface can influence how the a structure vibrates, producing unrepresentative data. These errors increase the smaller the vibrating object is. The cabling involved in these types of transducers makes them unpractical for rotating devices or environments that could be hazardous, both for hardware and personal safety.

Non-contact devices include optical devices, acoustic sensors/microphones and capacitance probes. These devices all result in measurements that have no effects on the structures they are measuring. This thesis focuses on laser methods for vibration measurements to allow a direct comparison of the different laser techniques used to capture experimental data to other laser based devices. The laser techniques, themselves can be grouped into two groups: single point techniques and multi-point techniques. Single point devices have high temporal resolution capable of capturing most excitation methods, but lack spatial resolution to capture relative instantaneous phase. Multi-point devices have high spatial resolution, capable of capturing full-field data at single frequencies (at the expense of a large data demand) but lack the temporal resolution to separate and identify frequencies from anything other than

single frequency excitation. The challenge for laser device development for vibration measurement is to find the balance between spatial and temporal resolution to ensure a system captures the best functionalities of both single point and spatial techniques.

The next two sections discuss different laser vibration transducers and their applications to vibration analysis and modal testing. The advantages and capabilities of each technique is summarised and particular applications of laser transducers to demonstrate each system's abilities.

2.2.1 Laser Doppler vibrometers

One of the most popular laser transducers for vibration measurement are laser Doppler vibrometers (LDV) [15]. LDV uses a focused laser beam to illuminate a single point on a vibrating component. Using the Doppler shift between the reference beam and the returning reflected light, from the illuminated vibration point, the velocity at that location can be measured. More advanced LDV systems can move the measurement point using mechanised mirrors to quickly move between other test points of interest. LDV was developed further to introduce the concept of continuous scanning LDV [16] that can measure thousands of test points during its scanning path. In this Section the applications of LDV and scanning LDV to measure vibration and its applications to modal analysis are discussed.

Single point laser vibrometry

The rapid development of LDV systems has proved LDV as a reliable measurement device in industrial applications due to its high temporal dynamic range, over 10MHz [15]. These applications extend from exploring different excitation methods [17–21] to structural damage detection [22] and noise reduction in the automotive industry [23–25] by using the system to measure acoustic intensity. Researchers at Ancona have applied the LDV technique to understanding the dynamic characteristics of composites and health sector materials [25–28].

The fundamental set-up of LDV was developed further into a tri-axial LDV system that enabled multiple axis measurements this captures three vectors from in-plane vibrations translated to the x, y and z components of vibrations. Bell et al [29] gave detailed analysis of how multi-axis devices actually measure velocity and its limitations, which led to an understanding of how LDV could be used to sense pitch and yaw. These results from Bell's research [29] have been used to adapt the tri-axial vibrometer with mechanical modifications to the system and then applied to measure torsional, pitch and yaw vibrations of rotating machines [30–33]. Bell's research extended original work from Miles et al [34] in early torsional and bending vibration measurement of rotating machines that used a dual beam system with 2 DOF. The tri-axial LDV system provided cross-sensitivity that has a sensitivity over 6 DOF.

Scanning laser vibrometry

LDV itself is a single point device and to measure other points, the device has to be physically moved between points of interest. Developments of the original LDV have brought the introduction of the scanning LDV (SLDV) [35]. Stanbridge et al [16, 36–38] developed this approach to measure vibrations in rotating machines and turbine blades, ranging from 0.1 m to 0.5 m in diameter. SLDV exploits the fact that the point of measurement from the laser beam can be changed by mechanically controlled mirrors that move the focused beam to points of interest, this stepped approach can be seen in left image in Figure 2.8. The system can then be used to automatically scan between as many points as required (limited by storage capacity and field of view). SLDV's adoption of a 3 beam system to allow multi-axis measurements [35] has led to it replacing the single point LDV over the last 5 years in some applications. This replacement is in part due to developments in signal post-processing and the adoption of the technology for automated assembly line testing.

Figure 2.8: The difference between measurements taken from stepped line scans (Left) and continuous line scans (right) [32]

Signal processing developments of the SLDV signals led to continuously scanning LDV (CSLDV) [32], shown in the right image of Figure 2.8. CSLDV has shown benefits for both in-plane vibrations of structures (large structures and micro-structures [39]) and rotating machinery such as turbine blades [40–45]. CSLDV continually scans over a harmonically vibrating surface at a uniform speed where the LDV output is modulated. The data envelope provides an operating deflection shape (ODS), the response to the excitation force, as a function of time across the distance along the chosen scan line. Scanning in this way dramatically reduces the data acquired by LDV, as CSLDV uses polynomial extraction to calculate the vibration pattern from the response data [46]. This increases the spatial resolution of the LDV technique to compliment its existing high temporal resolution [47].

Different scan paths are used for particular applications [48, 49]. An example of a conical scan path is seen in Figure 2.9, showing the laser path on the right and the frequency domain result of single frequency excitation of a rotating disc on the left, the sidebands in the signal are produced from the rotation of the disc. Conical

scans are useful for rotating discs as the laser scan is synchronised to the relative motion of the disc, giving a method to measure out-of-plane vibrations. Straight line scans are typically used in beam structures, however, velocity discontinuities can be introduced from straight line scans due to the change of direction at the end of each scan. This can be reduced with the use of a sinusoidal path scan to ensure there is no sudden change of velocity from the sudden change of direction of the scan. Martarelli [48] describes that uncertainties of CSLDV measurements can be introduced from when the scanning laser spot does not align with the spatial position of the control software's reference grid.

Both miscalibration of the system's software and mechanics, and moving complex shapes with many reference planes produce serious errors.

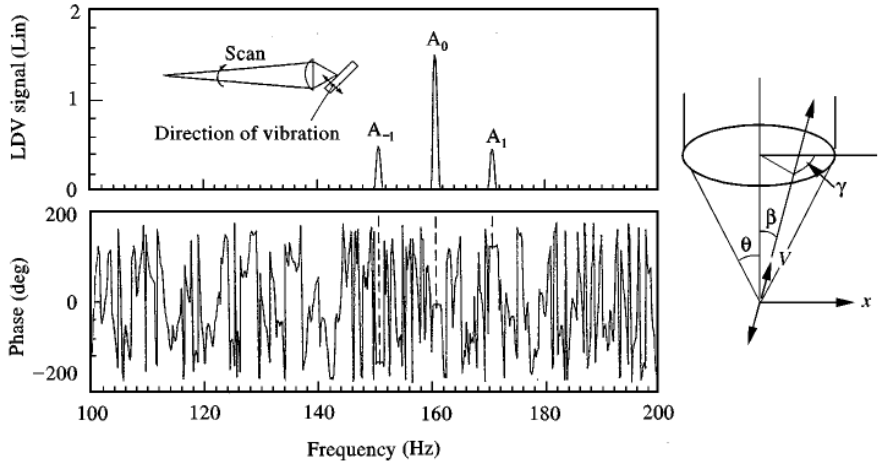

Figure 2.9: An example of a conical scan (right) the effect of the scanning beam can be seen by the sidebands in the frequency domain of the signal (upper left) [16]

Development of both software and firmware for control of CSLDV systems has enabled complete automated vibration analysis of test objects [41, 50, 51]. These developments allow faster measurement times and increased accuracy of the data due to self calibration functions and test optimisation software. The benefits of these developments were demonstrated by Brehmer et al [51] where 441 points were measured in 5 seconds of a 0.5 m square plate. This automation has been applied to damage detection [52–54] as well as the detection of non-linearities brought by these damages [55]. LDV, CSLDV have demonstrated, through their adoption and performance, the essential part they play in vibration testing for both research and industry. Research that focused on algorithm development and refinement [15, 32, 51, 56–59] over hardware developments demonstrates the advanced role LDV devices play in laser vibration measurement.

The LDV and SLDV have demonstrated their broad use and applications but further developments in areas such as dynamic resolution and spatial resolution can

further extend their applications [15]. The resolution for the majority of mechanical applications is by far sufficient; currently this resolution typically sits between 0.3 mm/s and 0.001 mm/s, this can be lowered further by increasing frequency bandwidth of the Doppler system. Errors from the speckle noise can be overcome to an extent through post processing and signal analysis [60]. The spatial resolution is limited by the fact that LDV and SLDV are single point devices. CSLDV provides some solution to extend the spatial resolution by synchronisation to a single frequency [47]. By knowing the excitation frequency, the tracking frequency and the path, the system can then correlate its mathematical path to the excitation frequency. The spatial data is then extracted using polynomial expansion. When the data is not a single frequency this is an issue; because the system can no longer cross-correlate the signals, and the lack of parallel measurement means the relative phase between measurements points is lost.

Multipoint laser Doppler vibrometry

Research in LDV and SLDV have developed systems which have increased spatial measurement abilities [61–63] has led to LDV multipoint systems; this was normally through either complex optics or what are effectively multiple LDVs in a single housing. A notable development was by Kilpatrick et al [64] where researchers developed a matrix laser vibrometer (MLV) that was a 16 x 16 parallel channel 2D vibrometer. The MLV can be seen in Figure 2.10, where its parallel square array has increased spatial resolution but retains all the temporal resolution of standard LDV. The spatial-temporal resolution was demonstrated with sinusoidal chirp frequency tests on a circular plate with frequency range of 1kHz to 50kHz exciting maximum surface velocities of ± 10 mm/s. The tests demonstrated that the MLV was sufficient to capture temporal data that shows how the material responded to the excitation but also the complex waves in the frequency domain. These results from the MLV demonstrate the benefits of measurements with a balance of spatial and temporal resolution and provide a benchmark to compare to other full-field techniques introduced in Section 2.2.2.

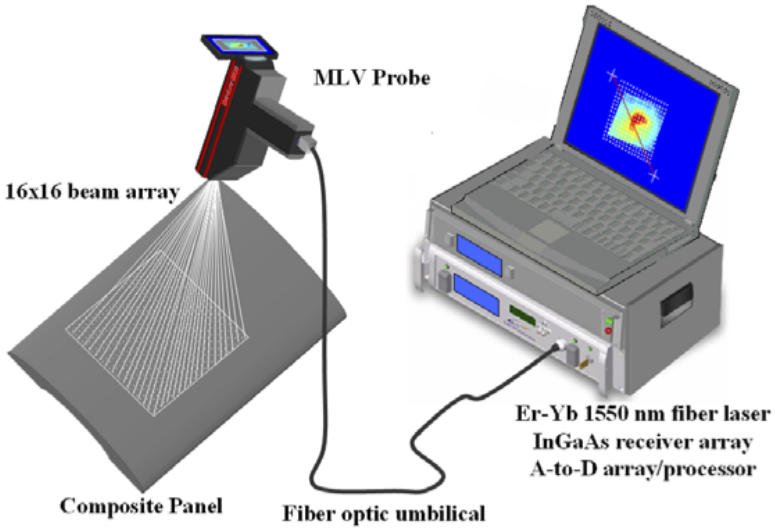

Figure 2.10: A 16 x 16 channel multi-pixel laser vibrometer developed by Kilpatrick et al [64]

Modal testing using laser Doppler vibrometers

As mentioned in Section 2.1 modal analysis is used to extract modal parameters from vibration test data; that is then used to define the dynamic characteristics of a test object. In this Section the application of LDV techniques to perform modal testing is reviewed.

LDV has the widest and most successful applications to modal testing of all non-contact devices and is also by far the most popular, in part due to its reliability as a measurement device but also the development of the post processing hardware such as decoders and data loggers. This made it possible for LDV to integrate with existing software for vibration analysis and modal analysis for industry needs.

Single frequency tests

Modal testing researchers Ewins and Stanbridge focused their work on the industrial applications of LDV and SLDV to modal testing. Martarelli & Stanbridge [16, 48, 65] and Martarelli & Ewins [65] focused initially on the effects of different scanning paths and calibration of the system had on the accuracy of performing modal analysis. Experiments were conducted on large square structures using different line scans and were correlated against an FE model. When the paths were calibrated well both natural frequencies and modal damping were calculated to an acceptable 5% from theoretical models and over 90% for the MAC. When the paths were poorly calibrated these increased to still within 5% for the natural frequency correlation but over 10% for the modal damping and the MAC reduced to 60%. The paper demonstrated the SLDV applications to modal analysis and extended what could be achieved using the high sensitivity of SLDV measurement signal. The sensitivities identified in Martelli's work [65] was extended by Ewins & Stanbridge [46, 66–68] to understand how the

continuous signals of the SLDV behaved during different scan paths. The analytical components of the raw signal from SLDV could be exploited to extract the Fourier coefficients and related to the modal parameters using polynomial extraction. The research enabled the SLDV to work as CSLDV and extract the complex (real and imaginary parts) of vibration to produce the operating deflection shape (ODS) of the vibrating object. The ODS at 495Hz from one of these extractions can be seen in Figure 2.11. The raw data was used to extract the eigenvectors of the test objects at each frequency, but was not compared to a finite element model or other methods to give a quantitative comparison of the modal parameters.

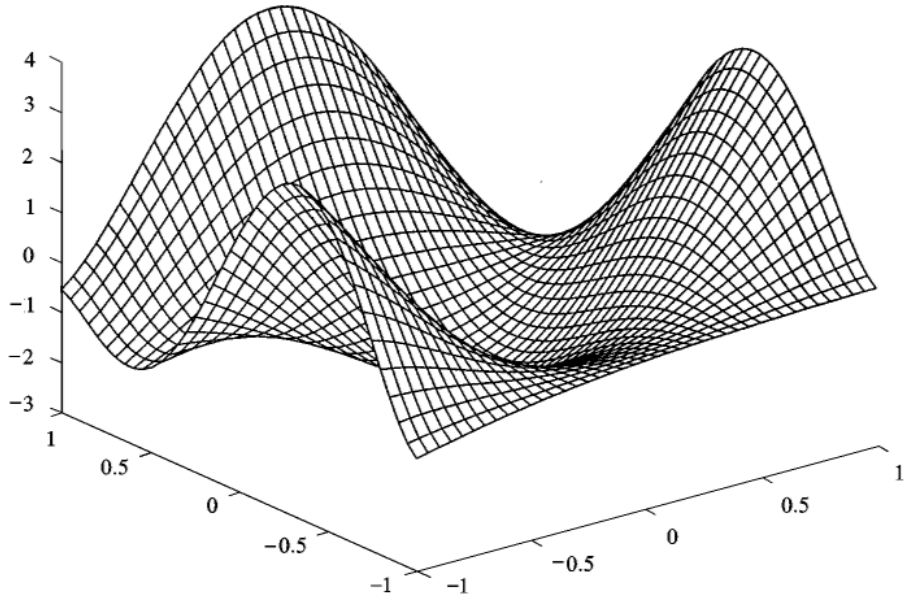

Figure 2.11: SLDV area ODS at 495 Hz from polynomial extraction of CSLDV data from [67]

The results from Standbridge et al [68] demonstrated the applications of the SLDV and CSLDV on large plates that are usually of a simple shape. Di Maio et al [32] applied CSLDV to perform modal testing on the tail cone of a LINX helicopter. Successfully extracting the first 8 modeshapes of the tail cone, with the natural frequency correlation to be within 0.5Hz of the analytical model and over 90% correlation of the MAC. This research by Di Maio et al [32] enabled the modal properties to be extracted directly from the CSLDV data with polynomial extraction of the continuous data captured. Polynomial extraction is a powerful tool but can fail if any unexpected discontinuities appear on the scan path (eg. holes, high levels of damping), meaning paths must be carefully selected and planned before any tests. Other industrial applications of CSLDV have ranged from loudspeaker parameter extraction [69], to noise, acoustic and harshness applications [70], complete modal analysis of wind turbines [71] and human skull modal characteristics [72].

Multi-frequency tests / ring down tests

The applications described so far were limited to single frequency sinusoidal testing, meaning that to capture true modal data stepped-sine tests, through ranges of frequencies of interest, are needed; accumulating heavy data requirements and rigorous (and time consuming) data analysis. Both Standbridge and Ribichini [73, 74] applied the CSLDV system for impact modal testing, where the extraction of polynomial coefficients are used to extract the vibration data to perform modal testing. In both cases the researchers successfully applied the technique to extract modal parameters of a plate structure. The spatial benefits this approach brings does have limitations; the scan-rate must be set short enough to allow a full scan to be completed before the transient vibration is approximately the same as the noise floor.

Both the single point measurements of LDV and SLDV and the approach used to extract vibration coefficients with CSLDV means that relative phase of multiple points cannot be measured simultaneously, which make it impossible to capture the relative phase of complex vibration waveforms. Kilpatrick's [64] MLV overcomes this with the introduction of 16 x 16 array and is used to measure a circular plate's response to sinusoidal chirp excitation. The MLDV tests were used to only identify the location of first 5 natural frequencies of the plate but has the technical ability to be extended to perform full modal testing to extract other modal parameters at these frequencies.

This Section has shown the applications of LDV for both general vibration measurement and quantified modal analysis. In most cases LDV has been developed to the same performance level as traditional contact devices. Their temporal resolution allows the dynamic range to capture most industrial vibration needs, but generally at a single point. The spatial resolution has been increased by the scanning techniques and polynomial extraction; but this is mostly applicable to single frequency analysis and any case where parallel measurement of multipoint is needed is of limited use. MLV overcame these limitations but is currently limited to a 16 x 16 array. In situations and conditions that are within their wide remit LDV devices have shown their diversity and accuracy.

2.2.2 Speckle pattern interferometry

Speckle pattern interferometry (SPI) can be used for non-contact measurement and it is capable of full-field measurements of static or dynamic deformations of components. SPI systems use an object beam to illuminate the component with a laser, a detector then captures the interference between this object beam and a reference beam through an interferometer. When the image of the object is compared with a reference image, this produces a fringe pattern, where the fringes correspond to a deformation of the object.

There are three main techniques to perform SPI: time averaged methods, pulsed and stroboscopic methods and high-speed SPI. Applications of each of these these applied to vibration measurement and modal testing are described in this Section.

Time-averaged speckle pattern interferometry

The most common use of SPI for vibration measurement is time-averaged SPI, where many period of vibrations are averaged over the detector's exposure time. The phase of the fringes produced are proportional to the wavelength of light used and the more fringes that are visible, the more the test object has been displaced. Powel and Stetson [75] reported the theory and application of full-field holography to measure an object using sinusoidal excitation and was extended by the researchers [76] to develop real-time full-field holography. Produced by introducing a holographic reference image produced from initial conditions into the holography system. This reference image then interfered with the Michaelson interferometry system to produce fringes that would relate to the object's shape of vibration. The real-time fringes were of lower quality to that of non-real-time vibration measurement methods of the time. Developments from Bulabois, [77] and Tiziani [78] for example, demonstrated with appropriate considerations real-time analysis could be improved. Bulabois, [77] exploited the statistical properties of the speckle pattern through different apertures to understand the modulation transfer functions that could produce a method for measuring tilt angles which used a surface mapping technique to produce real time time-averaged vibration images. Tiziani [78] improved the real-time applications by introducing crystals that have electrical and electro-optical properties, bismuth silicon oxide, $Bi_{12}SiO_{20}$(BSO). The crystal's properties made it possible to temporally store a reference image within the crystal, and therefore within the physical system, which then interfered with the laser path to produce vibration fringes.

The developments of digital image processing for SPI [79, 80] meant modifications to the physical system to store reference planes were not necessary. Digital systems enabled SPI to develop both hardware and image manipulation technology. The real-time fringe quality was improved by moving away from these examples of zero order Bessel fringes, where after the first few fringes the visibility dropped dramatically. Improvements by Creath [81] where the quality of the fringe contrast was improved through the use of a vibrating reference mirror in the reference beam which introduced a π-shift. Figure 2.12 shows experimental results completed for this thesis of a time-averaged system [81] with a phase-strained reference beam. This Figure shows a boundary clamped circular plate (14 cm diameter) vibrating at 520 Hz, the first resonant frequency of the plate. The fringes of vibration can be seen in the Figure, where no movement at the outside of the circle and the fringes increase towards the centre which is the point of maximum deflection.

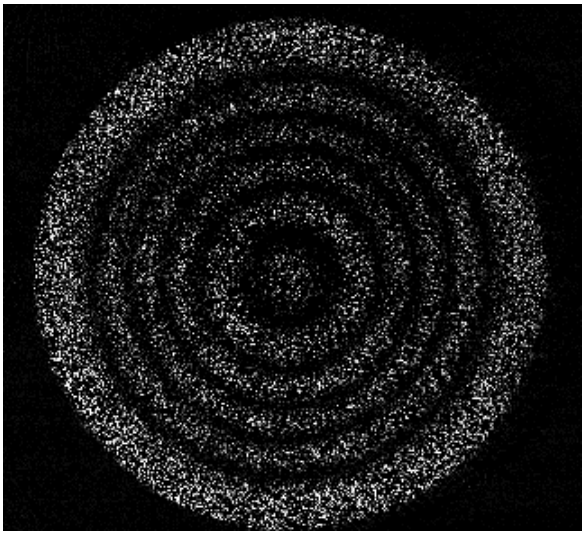

Figure 2.12: Experimental results of a boundary clamped circular plate vibrating at 520 Hz captured with a time-averaged SPI with phase-strained reference beam

Fibre based SPI systems by Valera [82] strained the optical fibre using piezoelectric material to give a similar phase change to improve the fringe quality without mechanical means. Lockberg [83] introduced phase modulation into the SPI system's reference beam specifically for low amplitudes of vibration.

The diagnostic abilities of time-average SPI technique was used by a range of researchers [84–94] and applied to engineering testing, including non-destructive testing and vibration analysis and demonstrated the benefits of full-field analysis can bring to these applications.

Understanding an object's resonant frequencies and indications of the shape of vibration can easily be captured by time-averaged SPI, but due to the time-averaging process the phase information is lost and limited to harmonic motion. For SPI to be used for modal testing this vibration phase must be retained accurately.

Pulsed and stroboscopic speckle pattern interferometry

Cookson at el [95] in 1978 introduced the concept of using double-pulsed lasers where these pulses were short in comparison to the object motion. Their introduction effectively freezes the object motion to capture the vibration event as the camera captures the vibration at each pulse through the vibration period. Pulsed generated fringes have a cosinusodial profile rather than Bessel fringes from time-average SPI, making it easier to analyse and give the understanding of the direction and magnitude of a vibrating object. Santoyo [96] was able to capture both out-of-plane and in-plane vibrations giving 3D measurements from a test object by the use of dual beams at 45 degrees from the measurement surface. Measurements include the vibration flow and vibrating shapes at the measured resonant frequencies. The same effect was also applied with multiple cameras with known viewing angles as demonstrated by San-

toyo and Pedrini [97]. Chambard et al [98] used the application of pulsed SPI for the vibration analysis of plates, washing machine panels and turbine blades. Figure 2.13 show the measurements from Chambard [98] where a rectangular plate clamped at two edges and the other edges are free. The left images are the undamped structure, the images on the right are the structure with passive damping added. The upper images are the vibration amplitude and the lower images are the vibration phase. The amplitude and phase were used to produce the vibration flow and acoustic intensity of the plates.

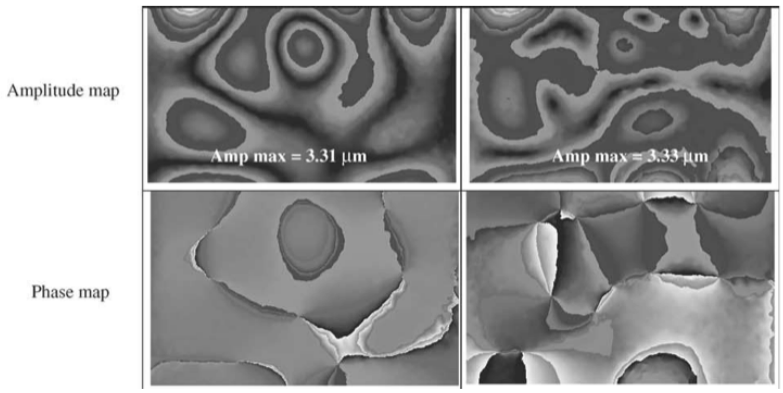

Figure 2.13: Amplitude and phase maps of a rectangle plate [98]

An extension of the pulsed SPI system that can then quantify both the amplitude and phase of vibration can be achieved by the introduction of a known phase-shift into the system [83, 99]. With the known phases measured by the system the objects vibration deformation can be calculated and as with time-average SPI, phase-stepped SPI has advanced with software developments that complement the hardware development [100, 101].

The ability of pulsed and stroboscopic SPI to capture both vibration magnitude and phase information has demonstrated its use in industrial applications. Its ability to capture transient events is also of interest, but for full-field applications the framrates are generally too low for the higher velocities of vibration. If transient events are to be captured high speed SPI must be used that offer much higher framerates to resolve the vibration data.

High-speed speckle pattern interferometry

Developing SPI to capture faster vibration events but keep the visibility needed for high quality SPI requires relatively short exposure in samples or relatively small phase changes per SPI measurement. Since these phase changes are directly proportional to surface velocity, the solution requires the use of shorter exposures that translates to higher frame-rates in detectors. This also requires development of high quality phase-stepping techniques to ensure the quality and accuracy of measurements are not lost.

Brown [102] presented a method to use a 16 x 64 sensor array that continually recorded with tape to perform HSSPI. The sensor could capture at 240,000 frames/s but hardware limited the ability to perform accurate phase-stepping. Developments in digital HSSPI by Moore [103] demonstrated the first use of high-speed cameras for HSSPI, where transient vibrations could be captured. This was achieved using a 45,000 frames per second camera (Kodak Ektapro 4540). These speeds were possible by reducing the pixel array to 64 x 64 from 256 x 256 (where 4500 fps was the maximum frame rate), increasing the temporal resolution by reducing the spatial resolution without sacrificing the system's parallel measurement ability. Figure 2.14 shows Moore's [103] system operating at 4500 frames/s and 256 x 256 pixels to continuously capture a centre clamped disc vibrating at 198 Hz. The series 2.14(a) to 2.14(f) show the fringes at increasing time incidents through the vibration period, (a) shows the plate at maximum deflection then decreasing in amplitude through to (d) that shows the disc at its neutral position, then increase to the opposite phased maximum at (f). This research was extended by synchronising the camera to the object vibration and a pulse-train over this vibration period would trigger the system to capture a sequence of 4 images, 1 for each pulse. Figure 2.15a shows the fringe pattern captured from the first pulse, a four bucket algorithm [104] was used on the 4 fringe patterns of the series to calculate the interference phase wrapped within π and $-\pi$ seen in Figure 2.15b. This phase is then unwrapped to give the amplitude seen in Figure 2.15c that measures 1.3 μm at the white edges of the plate and zero at the black centre, where it was clamped. The research was applied by Buckberry [105] to measure the operating conditions of vibrating door panels.

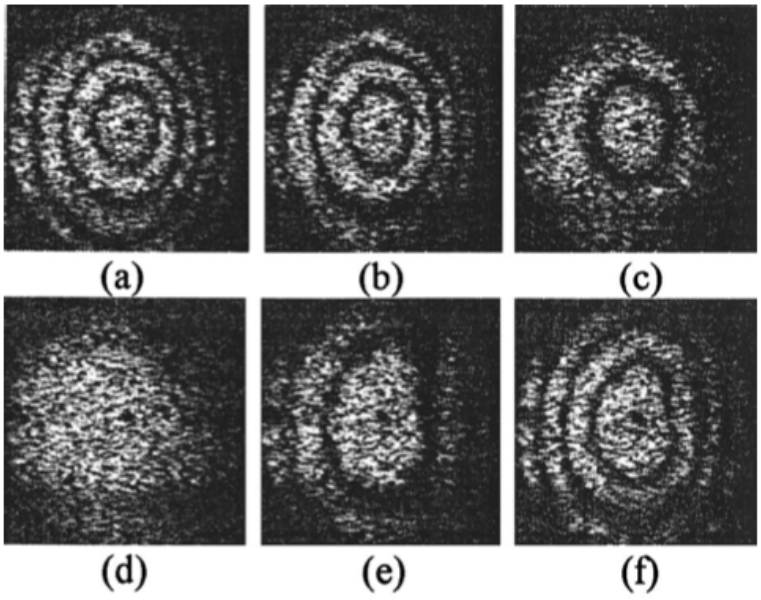

Figure 2.14: Vibration fringes for circular test plate from 198 Hz vibration captured at 4500 frames/s. Camera exposure not synchronized with object vibration [103].

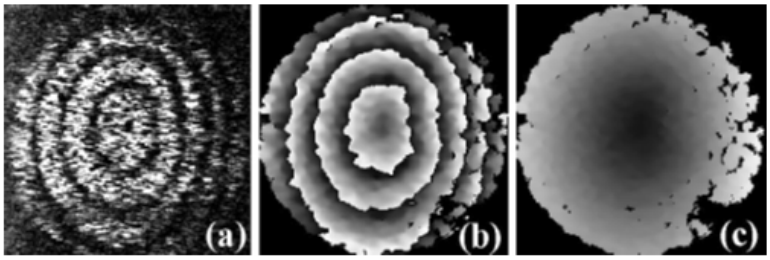

Figure 2.15: Results [103] that show: (a) Vibration fringes; (b) Wrapped phase and (c) Deformation from camera exposure at 4500 frames/s synchronised with object vibration (image from [105])

Huntley [106] demonstrated a system that kept the spatial resolution associated with SPI but dramatically increased the temporal resolution by synchronising the camera with a Pockels cell to introduce a interframe phase-step. The system had the ability to measure a theoretical maximum surface velocity of 67μm/s operating at 1000 frames/s with a detector with 239 x 192 pixels. The system needed a staircase of four $\pi/2$ phase-steps between each frame series, the accuracy of temporal phase-step functions were complemented with more accurate phase unwrapping techniques. Huntley demonstrated the stability of the proposed methods but was limited to low amplitude applications, below 25 μm.

Developments with inter-frame phase-stepping techniques enabled Kilpatrick [107] to extend HSSPI dynamic range with a faster high-speed CCD camera, with 1 x 256 pixel array and a frame rate of 100kHz. The phase-stepping was completed using the Carré algorithm which extended the system's measurable surface velocity to 3.2 mm/s, but had a theoretical limit of 10 mm/s. MacPherson [108] applied this SPI system to brake squeal analysis and transient analysis of plates, demonstrating the high dynamic range of the system. The system's high spatial resolution captured vibration deflection shapes that correspond to the resonant frequencies, as seen in the waterfall plot in Figure 2.16. This Figure shows the FFT response from the temporal data captured by Macpherson's HSSPI array [108] against frequency, where the deflection shapes can be seen at 117 Hz, 246 Hz, 566 Hz and 987 Hz.

Developments in complementary metal-oxide semiconductor (CMOS) cameras have shown applications to vibration analysis [109]. CMOS cameras have the ability to allow the user to select the region of interest they require on the the viewing plane, meaning the user can decide which pixels are used on the detector array for SPI measurements. This gives SPI the ability to rapidly switch between full-field analysis and then reduced sized arrays for higher frame-rate analysis. This was used by Wu et al [1] to demonstrate high-speed SPI with a CMOS detector and is the technique used in Chapter 3 for experimental modal testing. Wu demonstrated the use of a CMOS HSSPI to firstly show the system perform full-field (1024 x 1024) time-averaged mea-

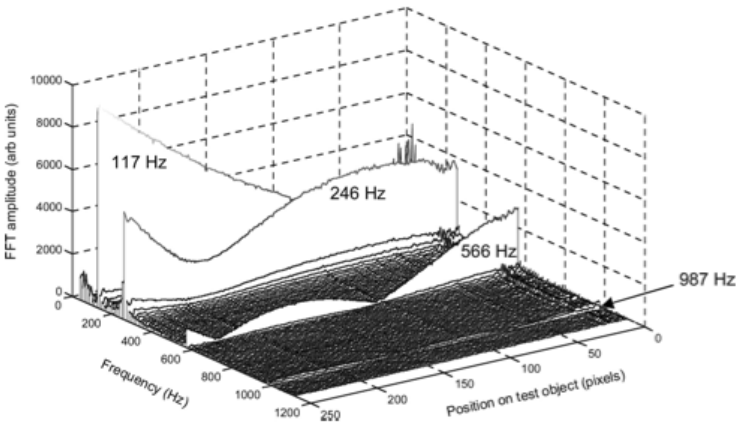

Figure 2.16: A waterfall plot of the response of a circualr disk to transient excitation, showing the FFT response across the linear array against frequency [108]

surements of a plate vibrating at 250 Hz at a framerate of 70 frames/s. The full-field pixels of the CMOS camera were reduced to a linear array of 125 x 1 pixels to extend the dynamic range to 33 kHz, that could measure a maximum surface velocity of 1.1 mm/s. The flexibility of the CMOS camera was further demonstrated by the use of a second region of interest, where a 16 x 64 region with a corresponding framerate of 10 kHz. Wu explored the velocity limits of the interframe phase-stepping and showed that a normalised velocity, the maximum surface velocity as a ratio of the maximum Nyquist velocity V_{Nyq}, needed for minimum sampling, would be $\pm 0.3\ V_{Nyq}$.

An alternative to interframe phase-stepping is spatial phase-stepping. This technique ensures at least two phase-stepped images are captured simultaneously by the measurement system, either with the use of multiple cameras [97] or with a phase grating [110–112] to create the required phase-stepped channels on a single detector. The accuracy of the spatial phase-step is critical to the performance of the technique, normally this step being $\pi/2$. Barrientos [113] successfully used spatial phase-stepping that was introduced by a holographic optical element (HOE) to capture transient response of a 100 μs impact on a cantilever beam (280 x 120 mm, thickness 4.7 mm). The HOE produced four $\pi/2$ increasing orders on a single detector plane starting from 0 order to π. Wu [2] used two binary phase gratings in both the object and reference beams to create a two channel system on a single CMOS detector, this approach increased the measurable surface velocity limit of Wu's earlier work [1] from 0.3 V_{Nyq} to equal the V_{Nyq}. This was demonstrated on a circular plate excited at 250 Hz at a framerate of 20,000 frames/s over a ROI of 656 x 1 pixels that translates to an effective pixel length of 256 x 1 once both channels are combined to calculate surface velocity. Wu also demonstrated the application of additional unwrapping to extend the velocity range further, where in conditions of continuous acceleration multiples of $2V_{Nyq}$ can be added to measurements that have exceeded the system limit. Wu demonstrated

experimentally that the unwrapping surface velocities of $4V_{Nyq}$ and could be extended by reducing the camera exposure. The experimental set-up demonstrated by Wu [2] is used in Chapter 4 to perform transient modal testing and in Chapter 5 to measure traveling waves. It is essential for the gratings in spatial phase-stepping to be well aligned as any miscalibrations causes the system to have a significant reduction in performance [2].

Any technique that uses speckle is subject to system errors [114] and SPI is no exception. Davilla [115, 116] reports three sources of errors that cause phase problems in HSSPI: intensity errors on, velocity errors, and speckle decorrelation, where careful selection of phase algorithms can reduce these errors. The Carré algorithm was shown to produce the lowest errors on average, but algorithms with a higher number phase-stepped algorithms provide higher reliability for low stability of speckle and intensity. The velocity errors can be significantly reduced by the system staying within 40% of the Nyquist velocity limit [117]. Environmental vibration induced errors are discussed by Ruiz [118, 119] where conditions of high amplitude and low frequency in testing requires an adaptive approach to phase-stepping. Any aliasing effects can be significantly reduced by increasing the framerate of the detector but a significant contribution of these errors can be attributed to spectrum contributions from outside of the phase-shifting algorithms, again the Carré algorithm was shown to be reliable in the unwrapping process with a consistent low average error ratio.

Modal testing using speckle pattern interferometry

In this Section, applications of SPI to modal analysis are discussed. SPI itself is a powerful tool for vibration measurement, resonant frequencies can be identified quickly and the use of stroboscopic and phase-stepped SPI enables the relative phase to be captured and resolved. The previous Section highlighted many applications of SPI for vibration measurement to either identify resonant frequencies or to capture full-field measurements of the operating deflection shape; this however is not always taken further for complete modal testing to extract other modal parameters other than the natural frequency.

Graham et al [120–122] used a pulsed SPI system and compared the results to LDV and accelerometer measurements. The experimental data was correlated against an FE model. The test object was a square plate and an ultrasonic block horn. The SPI system showed the highest correlation with the FE results at 79%. The lowest correlation was between the accelerometer and the FE results at 53%. However, this lower result is most likely due to the surface ratio between the contact accelerometer's surface area 20 mm^2 and the relatively small size of the block horn would likely produce a coupling effect that would give unrepresentative measured data. If these tests were to be repeated with a modern (and much smaller) accelerometer, the comparisons

of performance would likely improve. In each of the research papers the frequency comparison was limited to two frequencies, so comparative results are limited.

Auweraer [123, 124] demonstrated the use of pulsed SPI for modal testing in the automotive industry. The researchers used stepped-sine testing to capture a step by step frequency full-field response of the test objects. The response was used with the input force to create FRFs that were used by modal analysis to extract modal parameters. The results were compared to accelerometer results and the natural frequencies extracted each fell within 10% of each other, but the research did not compare other modal properties. The paper highlights the use of SPI for capturing accurate full-field data from single frequency excitation and indicates the need for a system that can capture transient events to reduce measurement time. Romero [125], Giraudeau [126], Morrison [127], Ozturk [128] and Martinez [129] used SPI to perform modal testing on vibrating plates. In each case the researchers applied modal analysis to extract the natural frequencies and to compare the operating deflection shapes, but no further modal analysis is applied.

Most applications of SPI do not extract full modal parameters. It is usually used with operating conditions to exploit SPI's full-field ability to understand vibration effects on objects. The advancement of LDV techniques (and its compatibility with existing post-processing hardware) made it the current industry standard for non-contact modal testing; while similarly performing techniques such as HSSPI were still developing. HSSPI applications have the benefits of parallel measurement, in a relatively simple set-up, while reducing testing time and the ability to have full-field analysis to quickly estimate resonant frequencies. However most applications of modal testing with SPI have been for single frequency analysis, this is overcome in this thesis with the application of the work by Wu [1, 2] and applying the systems to transient modal testing [130, 131] to provide a high spatial and high temporal resolution for faster modal testing.

2.2.3 Laser transducers to measure traveling waves

The complex behaviour of traveling waves can help understand problems with a system's operation or help detect damage [64]. New materials that are developed, such as materials for active vibration control [132], have an increased chance of complex vibration scenarios with the potential to excite traveling waves that need to be accurately measured. However, traveling waves are difficult to quantify experimentally [133]. This is in part because traditional approaches are based on contact transducers, which add a coupling effect to the system and can then change the conditions needed to excite a traveling wave. Also when the measurements are from a single point system the relative phase between multiple measurement points is lost and this

is required to fully understand the wave's behaviour. Both LDV and SPI provide a non-contact solution to observe traveling waves without any coupling effects, and with system considerations the ability to measure multiple points simultaneously.

Natural traveling waves occur from the resonant frequency's two degenerate mode-shapes, which possess a cosine part and a sine part [134]. In ideal conditions these two degenerate modes occur at exactly the same frequency and which ever is more dominant at that instant prevails. In real structures, due to minor non-linearities, these two degenerate mode shapes occur at slightly different frequencies from each other. When these two frequencies occur within 1Hz [135] there is a high chance these frequencies couple together and their phase differences can produce a traveling wave. This is more likely to happen in lightly damped structures.

Work by Bucher [132, 133, 136] showed the adoption of both LDV and SLDV systems to measure the response of traveling waves. Their motivation was to use traveling waves as a method for propulsion and were trying to find methods to excite pure traveling waves. These waves exist where only the complex part of the wave equation exist and there is no standing waves where there is no real part of the wave equation. The measurements were used as a feedback loop to optimise the excitation profile to ensure only pure traveling waves were present in the test objects. These measurements were used to update and optimise an analytical model for future predictions. An LDV system was used to measure traveling waves in both beams [133, 136] and annular rings [132]. These methods were based on measurements at a single point, which means that tests must be repeated multiple times at different scan rates to separate the traveling waves from the scanning rate. The different responses were coupled together to understand the system's vibration response at the different locations along the test objects, further analysis was required to understand if a traveling wave was present. To identify traveling waves with a single point system requires the use of post-testing signal analysis and coupling, the most common way is to use the modal complexity function (MCF) [3, 137] where multiple tests and analysis of the data can provide the complexity of a response function and the level of this complexity indicates the presence of traveling waves or not. MCF does not give any quantitative details of the traveling wave, just an indication of their presence. A technique called direction FRF(dFRF) can be adopted [138] to overcome this, which normalises the FRF to provide the shape of a traveling wave. An extension of dFRF called the directional spectral analysis [139] can be used to indicate the direction of the traveling wave.

Standbridge showed that with appropriate scans with an SLDV system over multiple tests [49] that the direction of traveling modes could be identified. Stanbridge [140] also demonstrated the use of a CSLDV to identify close modes likely to pro-

duce traveling waves, with the use of repeat testing to extract polynomial series from each scan achieved through stepped-sine excitation. All single point techniques require multiple testing and some form of post-processing to understand the presence of traveling waves. The extra testing and post-processing can be overcome by use of multipoint parallel measurements.

Kilpatrick [64] used MLV, effectively a 16 x 16 array of LDV systems, to measure the vibrations of a 90 mm diameter centre clamped disc of 6 mm. The plate was excited with a sinusoidal frequency chirp with frequency range 1.0 kHz to 50 kHz where Figure 2.17 shows the results of this. Column 3 shows the temporal measurement of a traveling waves with increasing time down the column and is rotating anti-clockwise. The frequency domain analysis in columns 4-7, give an insight into the identification of some of the divergent modes that contribute to the creation of traveling waves.

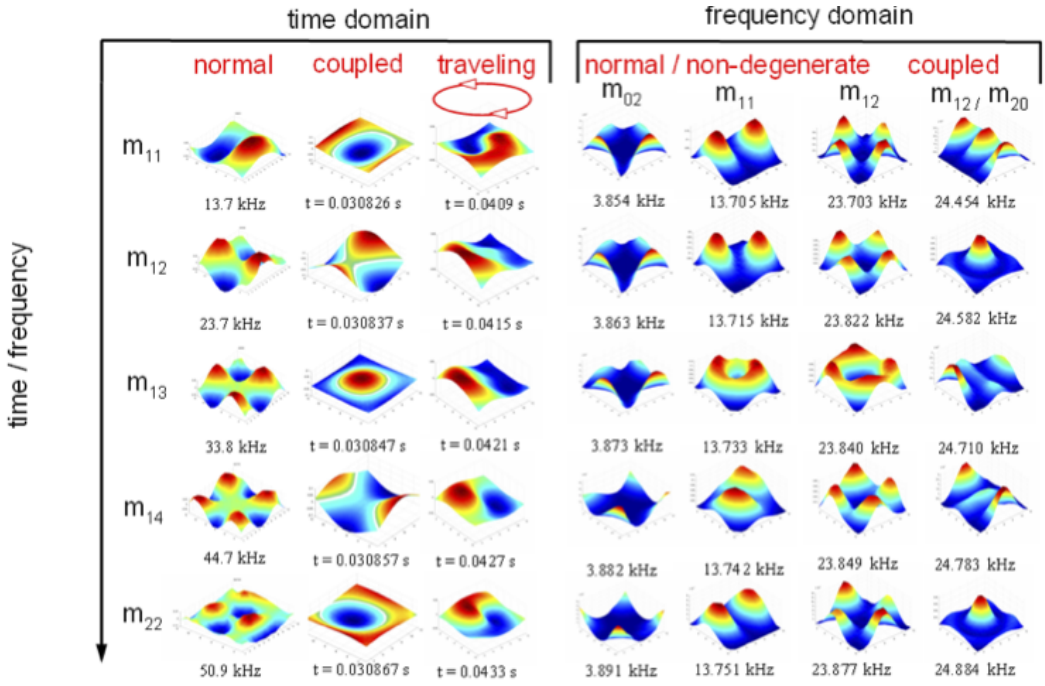

Figure 2.17: Outputs of MLV testing, the velocity-time profile for the 2D velocity maximums in column 1, coupled axisymmetric modes, column 2, and traveling waves (column 3). Frequency domain analysis (columns 3-6) of the plate at incremental frequencies [64]

Smigielski [141] used a full-field SPI approach to measure the power flow of traveling waves induced by two shakers at different points on a square plate. The shakers were set to the first resonance of the plate at 127 Hz but were $\pi/2$ out of phase form each other to excite a traveling wave, the presence of the wave was determined by the phase of vibration having a constant ramp in a clockwise direction.

Reeves et al [142] applied the research by Moore [103] to use HSSPI to the study of brake squeal. The HSSPI system captured test data at 18,000 frames/s with

64 x 256 pixels and 27,000 frames/s with 64 x 128 pixels, this high spatial resolution captured the fundamental traveling waves frequency of 3 kHz by exploiting the system's parallel measurement capability. The high temporal resolution of the HSSPI system enabled the traveling wave fringes to be visually tracked over the captured frames. This fundamental frequency contributed to acoustic problems associated with brake squeal, the data was used to compare against an analytical models for future design considerations. MacPherson [108] used an inter-frame phase-stepped HSSPI system to perform similar analysis on brake systems. The system had a 100 KHz framerate over a 1 x 256 pixel high-speed camera array, this can be seen in Figure 2.18 where the white line on the left image shows the measurement location. The right image shows the measured displacement from the system, where the x-axis corresponds to the systems array and the y-axis is the frames captured, the maximum displacement measured was 1 μm. The traveling wave was confirmed by observing the vibration's spatial phase across the pixel array in the frequency domain, showing a constant slope and the analysis confirmed the 3 kHz fundamental resonant frequency. Chapter 5 of this thesis extends the analysis of HSSPI to measure traveling waves and demonstrate the ratios of standing and traveling waves.

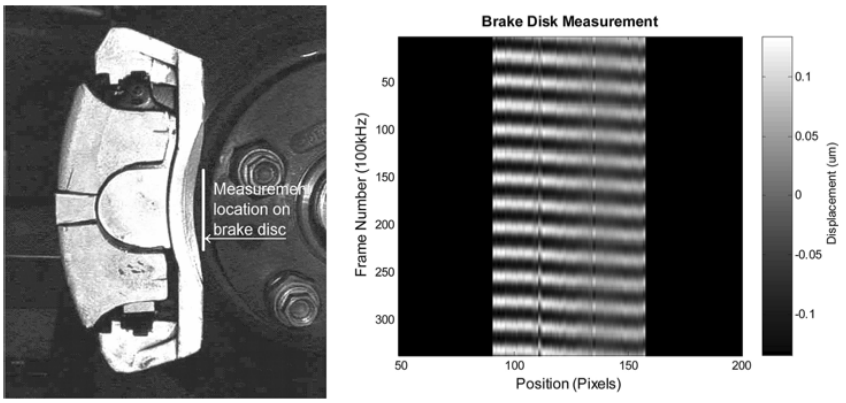

Figure 2.18: Brake disc measurement using temporal phase-stepped HSSPI at 100 kHz from Macpherson et al [108]

2.3 Chapter summary

This Chapter has given an overview of modal testing using laser transducers. The fundamentals of modal testing and analysis was presented to give an understanding of the techniques and technology needed to perform modal testing. A review of laser transducers used to measure vibration response was presented. This included LDV and SPI techniques, where the developments and limitations of the systems were presented as well as their application to vibration analysis and modal testing.

This work is extended in this thesis with the use of temporal phase-stepped HSSPI, in Chapter 3, and spatial phase-stepped HSSPI, in Chapter 4, to perform impact

modal testing to extract beyond the natural frequencies and compare other modal parameters to an FE model.

The applications of LDV and SPI techniques to measure traveling waves was presented and included applications for the successful identification of traveling waves was discussed. Chapter 5 of this thesis extends this research to understand the ratios of standing and traveling waves and the benefits parallel vibration measurement brings to traveling wave analysis.

Chapter 3

Modal testing using HSSPI with temporal phase-stepping

An inter-frame phase-stepped SPI system using a high-speed CMOS camera was used as a multipoint vibrometer to perform modal testing on two test objects; a circular plate and two overlapping square plates. The extracted modal parameters were correlated against an FE model and compared to the same tests performed with an accelerometer. The CMOS system used was developed by Wu et al [1] and described briefly in the next Section.

This application demonstrates the flexibility of the CMOS detector to select regions of interest (ROIs) to enable full-field time-averaged measurements, and then reduce the ROI to a selected region to capture time-resolved measurements sampled at up to 33 kHz. The vibration data from the vibrometer was used to collect velocity profiles of the test objects subjected to transient excitation and is presented in this Chapter. These results will be compared to the industry standard methodology of an accelerometer and discussed in the closing sections of this Chapter.

3.1 Experimental system

The system used was developed at Heriot-Watt University (HWU) by Wu et al [1] and was introduced in Section 2.2.2. The schematic diagram of the experimental system is shown in Figure 3.1 where the output from a diode-pumped, frequency doubled Nd:YVO4 laser (single-frequency continuous-wave output at 532 nm with power levels up to 5 W) was divided by a polarizing beamsplitter (PBS) into orthogonally linearly polarised object and reference beams. Each beam was launched into the fast axis of a highly-birefringent (Hi-Bi) optical fibre. The output power of the laser was maintained below 500 mW in order to prevent damage to the fibre ends.

The principle of the system is based on HSSPI and makes use of a Photonfocus MV-D1024, 8 bit, CMOS camera. This type of camera enables user-selected ROIs to be

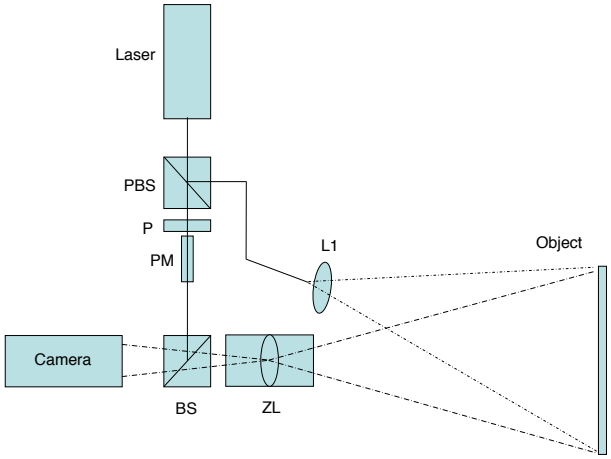

Figure 3.1: Schematic of experimental set-up. PBS polarising beamsplitter; P polariser; PM phase modulator, L1 optional cylindrical lens; BS beamsplitter and ZL zoom lens.

defined and allows the user to switch easily from full-field time-averaged measurements to smaller time-resolved measurements at sample rates of up to 70 kHz, when the pixel rate is reduced to 1 x 4 pixels. Reducing the pixel line length compromises the spatial resolution for higher temporal resolution.

The speckle pattern detected by the systems is known as an objective speckle pattern. The average size of an objective speckle, generated from a region with the diameter of D , is given by:

$$\Delta x = \frac{L\lambda}{D} \tag{3.1}$$

where L is the distance between the viewing screen and object and λ is the wavelength of the light. The speckle is termed objective, because for a given illumination, the scale of the speckle depends only on the position of the plane where it is viewed. The object illumination is approximately collinear with the optic axis of the imaging lens and camera, which is defined as the z-axis. The component of object deformation or displacement resolved in the z-direction produces a change in the optical path length of the object beam, producing a change in the interferogram phase $\phi(x, y, t)$ and therefore the interferogram intensity. If such a speckle pattern is imaged onto the screen by a lens, a subjective speckle pattern is formed. The spatial distribution of this speckle is determined by the diffraction limit of the imaging system. Subjective speckle size is taken as the separation between the first two minima of the diffraction Bessel function and thus is dependent on the focal length f and lens aperture D_a.

The average size of an individual subjective speckle observed at the imaging plane may be expressed as:

$$\sigma = \frac{\lambda f}{D_a} \tag{3.2}$$

The system detects any change in motion, of the test surface, as a change in the interference phase and therefore a change in intensity, between laser light scattered from the surface and the reference beam. For continuous wave illumination, the interference intensity recorded by the CMOS detector at pixel (x, y) and at time t_n, integrated over the frame exposure t_e, is given by [1]:

$$I_n(x, y, t_n) = I_O(x, y) \left\{ 1 + \gamma_O sinc\left(\frac{\Delta}{2}\right) cos(\Phi_O(x, y, t_n) - \Phi_R(x, y, t_n)) \right\} \tag{3.3}$$

where I_O is the bias intensity and γ_O is the visibility of the speckle modulation (and depends on the relative intensities of the two beams, their coherence, and states of polarisation).

The object phase, Φ_O, is the combination of a random speckle phase ψ_O plus a term proportional to the out-of-plane target deformation, $(2\pi/\lambda)\ \eta\ w_n$, where λ is the wavelength of the laser and η is the interferometer's sensitivity factor equal to 2 throughout this thesis. Temporal phase modulation requires a phase carrier to be introduced to the interferometer in order to calculate Φ_O from the interference signal. Therefore, the reference phase, Φ_R, includes a phase-step increment $2\pi n/N$,

$$\Phi_O(x, y, t_n) - \Phi_R(x, y, t_n) = \tan^{-1}\left(\frac{\sqrt{[3(I_n - I_{n+1}) - (I_{n-1} - I_{n+2})][(I_n - I_{n+1}) + (I_{n-1} - I_{n+2})]}}{(I_n + I_{n+1}) - (I_{n-1} - I_{n+2})} \right) \tag{3.4}$$

where N is the number of steps per 2π-period of Equation 3.4. For $N = 4$, the interference phase is calculated from these phase-stepped intensity measurements of the digitised speckle patterns using the well-known Carré algorithm [143], which is insensitive to errors in the phase steps caused by linear surface motion. It is assumed that the camera sampling rate is sufficiently high that the surface velocity is approximately linear during any four consecutive frames so that the phase at a given pixel can be calculated from I_{n-1} to I_{n+2}.

Images were transferred to a computer (PC) at up to 20,000 frames per second via a camera link interface. A camera frame synchronisation signal was passed from the PC to a staircase waveform generator (SWG) that generated a staircase voltage

with N equal steps, each step synchronised to the camera frame rate. The SWG gain was adjusted to produce phase steps of $\pi/2$ radians in the reference beam during the blanking period between frames in Figure 3.2. Figure 3.2(a) shows the variation in mean phase-step size (calculated over all pixels modulating at greater than 5% of the maximum theoretical modulation) for a sequence of phase-stepped frames recorded with the test object stationary. The error bars show plus and minus one standard deviation about the mean. Over all frames in the sequence, a mean phase step of 90.20° with a standard deviation of 9.85° was obtained and seen in Figure 3.2(b).

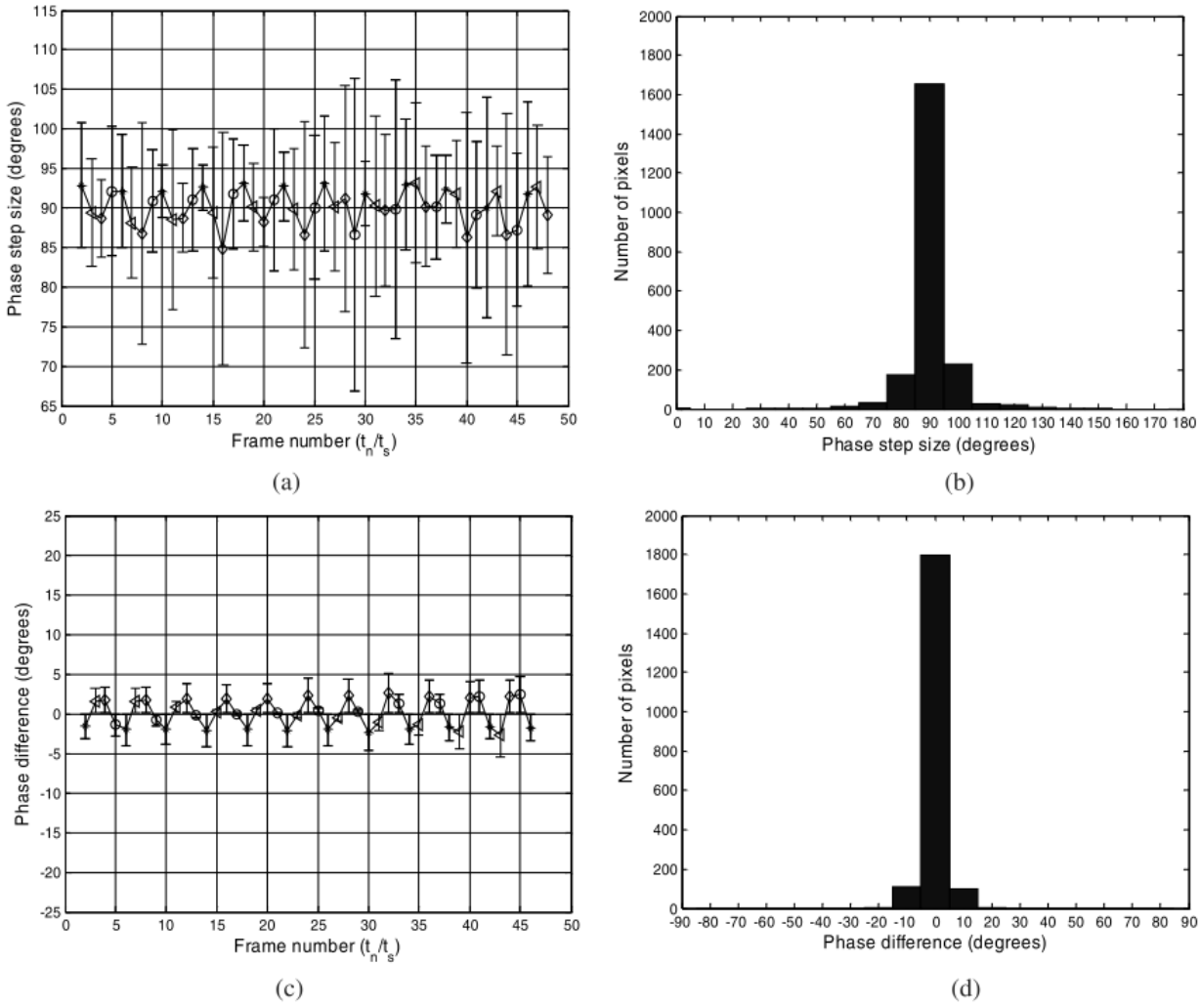

Figure 3.2: a) Interframe phase-step size plotted against the frame number and (b) phase-step size distribution for all frames recorded for a stationary object with a frame rate of 33 kHz. (c) Interframe phase difference plotted against the frame number and (d) phase difference distribution, for the same image sequences as (a) and (b). Image from [1]

The phase difference between each successive frame is given by:

$$\Phi_O(x,y,t_n) - \Phi_R(x,y,t_n) - \{\Phi_O(x,y,t_{n-1}) - \Phi_R(x,y,t_{n-1})\} = \Delta\Phi_O(x,y,t_n) + \frac{\pi}{2} \quad (3.5)$$

where $\Delta\Phi_O(t_n) = \Phi_O(t_n) - \Phi_O(t_n - 1)$ is the change in phase due to the surface deformation between frames and $\pi/2$ is the applied phase step. Figure 3.2(c) shows the mean phase difference between successive frames (calculated over all pixels modulating at greater than 5% of the maximum theoretical modulation) for the same sequence of phase-stepped frames recorded with the test object stationary. Over the whole sequence, a mean phase difference of -0.002° with a standard deviation of 3.06° was obtained seen in Figure 3.2(d).

Using the conditions imposed by the Nyquist limit, that there must be at least 2 samples per fringe period and a maximum phase change of $\pm\pi$ in Φ_O between any two frames, this corresponds to a velocity limit of:

$$\mathcal{V}_{Nyq} = \pm\frac{\lambda}{2\eta t_s}\left[1 \mp \frac{2}{N}\right] \tag{3.6}$$

The upper and lower velocity limits correspond to the sense of the surface displacement relative to the phase step imposed on the reference beam. Unless the surface displacement is unidirectional and of a known sense, the lower magnitude value of V_{Nyq} sets the practical velocity limit [1]. This phase difference between the frames given from Equation 3.5, without the phase step, is wrapped into the range -π to π radians and then related to the surface velocity of the plate by:

$$w'(x, y, t_n) = \frac{\mathcal{V}_{Nyq}}{\pi}\Delta\Phi_O(x, y, t_n) \tag{3.7}$$

This approach to find the velocity eliminates the need for temporal unwrapping associated with displacement measurements, which can cause discontinuities within the data. Rearranging Equation 3.7 gives:

$$\frac{w'(x, y, t_n)}{|\mathcal{V}_{Nyq}|} = \frac{\Delta\Phi_O(x, y, t_n)}{\pi} \tag{3.8}$$

The introduction of the temporal phase step gives a normalised surface velocity limit that can be used to ensure that the data collected is within the system limits and therefore reliable. This is the result of the Nyquist condition that the cosine term from Equation 3.3 must be sampled at least twice per fringe. The maximum surface velocity that can be reliably measured due to the four-step algorithm used with the inter-frame phase step corresponds to a theoretical limit of ± 0.5 but in practice ± 0.3 is the typical practical maximum measurable surface velocity [1].

The phase information can be numerically differentiated to give the surface acceleration:

$$w''(x, y, t_n) = \frac{\lambda}{2\pi\eta t_s^2}\Delta^2\Phi_O(x, y, t_n) \tag{3.9}$$

where $\Delta\Phi_O(t_n) = \Delta^2\Phi_O(t_n + 1) - \Delta^2\Phi_O(t_n)$ represents the rate of change in phase difference between frames. Rearranging Equation 3.9 yields the normalised acceleration:

$$\frac{w''(x, y, t_n)}{2\pi f|\mathcal{V}_{Nyq}|} = \frac{\Delta^2\Phi_O(x, y, t_n)}{2\pi^2 f t_s} \tag{3.10}$$

Similarly, for the deformation, numerical integration can be applied down each column to give:

$$w(x, y, t_n) = \frac{\lambda}{2\pi\eta t_s}\sum\Delta\Phi_O(x, y, t_n) \tag{3.11}$$

and again to normalise this to the Nyquist limit,

$$\frac{2\pi f w(x, y, t_n)}{|\mathcal{V}_{Nyq}|} = 2ft_s\sum\Delta\Phi_O(x, y, t_n) \tag{3.12}$$

If the system stays within its limits, it can be used to perform non-contact multipoint modal testing and has the ability to measure transient events.

3.2 Simulation work

To model the effects on system performance of multi-frequency excitations, a Matlab simulation was developed. The model used the characteristics of the experimental system in Section 3.1 to simulate a 250 x 1 pixel line fringe pattern generated using Equation 3.3. The multi-frequency vibration introduced the following equation:

$$w'(x, t_n) = \frac{2\pi\eta}{\lambda}w_0\sum_{m=1}^{M} 2\pi f_m sin(2\pi f_m t_n)sin(2\pi x K_m) \tag{3.13}$$

Where f_m is the frequency of the object's multiple resonant frequencies: 98 Hz, 211 Hz, 248 Hz, 458Hz and 552 Hz. K_m is the spatial shape of the resonant frequency f_m captured on the camera array, x, corresponding to the frame time t_n. The vibration amplitude w_0 was defined in terms of the maximum normalized surface velocity for a given interferometer arrangement (λ = 532 nm, η = 2 and t_s, proportional to the

Nyquist limit V_{Nyq} seen in Equation 3.7). The normalised velocity was set to $0.2V_{Nyq}$. The model produced the simulated intensity fringe pattern from this excitation seen in Figure 3.3. The fringe pattern can then be used to calculate the inter-frame phase distribution using the Carré algorithm (Equation 3.5) seen in Figure 3.4. Unwrapping the phase and using Equation 3.8 the normalised velocity response can be calculated to produce Figure 3.5, which shows the different velocities across the array varying with time. The multi-frequencies can be seen from the constructive and destructive wave pattern produced in Figure 3.5.

To have the results in the frequency domain an FFT transform was applied to the velocity to produce the spatial-frequency profile that can be seen in Figure 3.6 which shows the spatial shapes of the excitation and their location in the frequency domain. The models are to represent and validate the Matlab code for multi-frequency analysis and its reliability for post-processing of the fringe patterns that is used for the subsequent experimental tests and was not for quantative analysis.

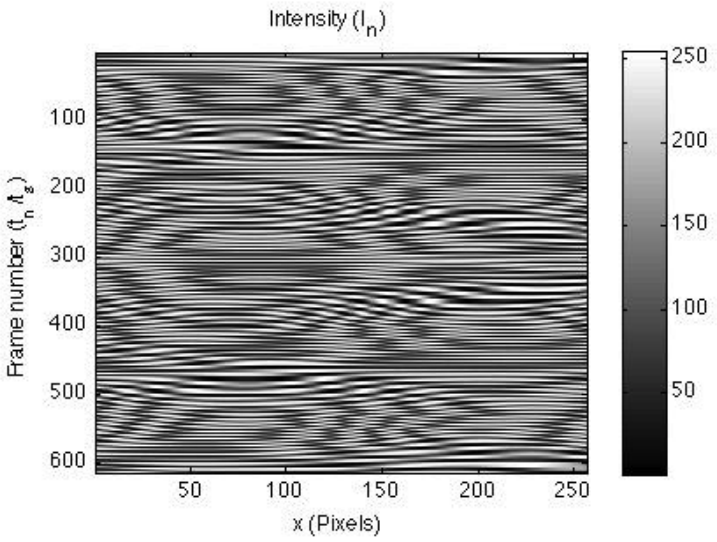

Figure 3.3: Multi-frequency simulation of intensity array for each frame, amplitude of $0.2V_{Nyq}$

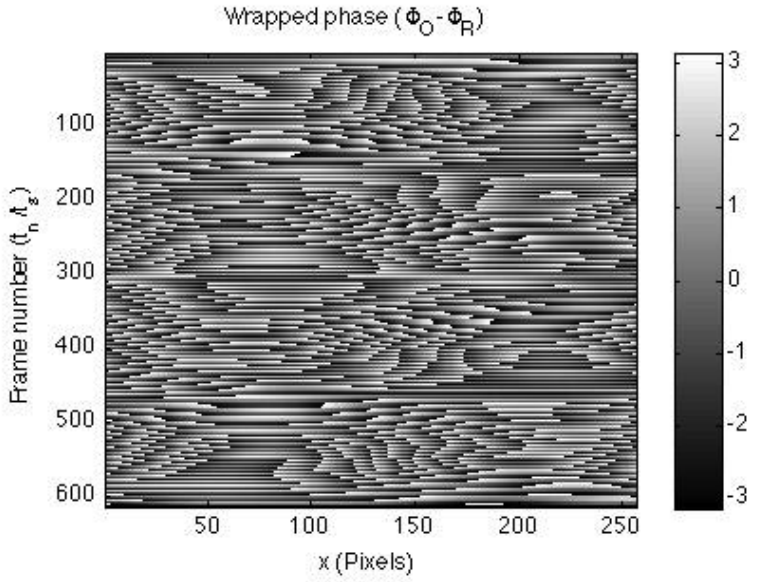

Figure 3.4: Multi-frequency simulation of wrapped phase array for each frame, amplitude of $0.2V_{Nyq}$

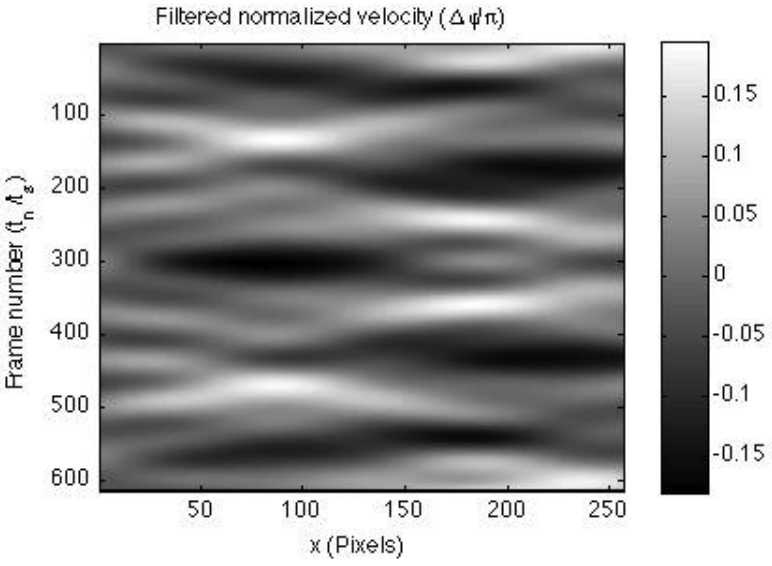

Figure 3.5: Multi-frequency simulation of velocity array against each frame, amplitude of $0.2V_{Nyq}$

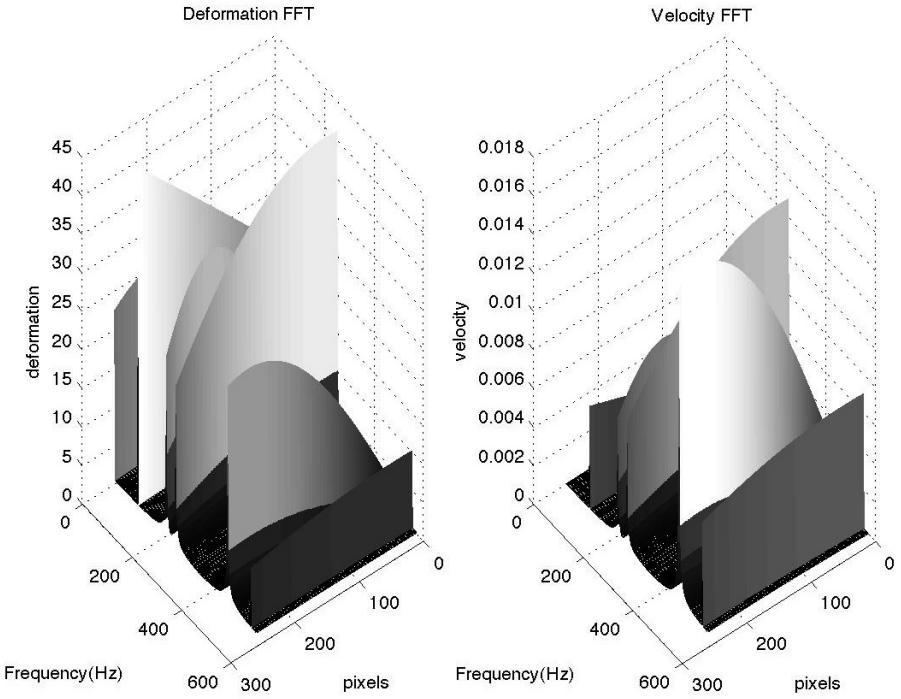

Figure 3.6: Multi-frequency waterfall plots showing velocity & displacement pixel arrays against frequency, amplitude of $0.2V_{Nyq}$

3.3 Sound pulse excitation

To demonstrate the system's performance and understand its ability to perform modal testing, introductory tests were conducted. These tests were to show the system capturing single frequency excitation and multi-frequency excitation. These initial tests were conducted using a circular plate clamped at its centre and excited by a small loudspeaker attached to a function generator. Non-contact excitation was chosen to ensure the system would provide a response that is representative of a modal ring down test from a modal hammer and to give results closer to the pure natural frequencies of the test object as introduced in Section 2.1.3. This type of excitation does limit the dynamic range that can be excited as acoustic excitation limits the force that can be transmitted into the object. The test object, excitation method and results are described in the following sections.

3.3.1 Test setup for acoustic excitation

The test object used was a centre-clamped, 14 cm diameter, circular aluminium plate of 1 mm thickness. A retro-reflective coating was applied to the front of the plate to enhance the surface's optical reflection. The plate was excited by a small loudspeaker (impedance rating of 8Ω), the signal for the speaker was produced from a function generator and the loudspeaker was placed behind the plate. The SPI system used to measure the velocity response as Section 3.1, and was positioned and focused with full

field ROI (1024 x 1024), then reduced to 1 x 250 for testing to increase the maximum surface velocity.

The plate was subjected to 5 different excitation signals from the loudspeaker. The first 4 were single frequencies at the same magnitude (5 V), the fifth excitation was a pulse (500 μs pulse at 3.2 V). The single frequencies used to excite the plate were 101 Hz, 201 Hz, 242 Hz and 545 Hz. These frequencies were chosen by using full-field SPI to observe the response of the plate to a range of individual frequencies from 80Hz to 600Hz, the frequencies with the highest fringe density showed the location of a natural frequency, and occurred at the mentioned frequencies.

The pulse excitation from the loudspeaker was set to the shortest pulse possible on the frequency generator 500 μs, which theoretically excites a frequency range of up to 2 kHz if all the energy is ideally transferred. The voltage used to excite the loudspeaker was 3.2 V, lower than the single frequency excitation as the coupling effect of the individual velocities from each frequency would go through the dynamic range of the SPI system. An iterative approach was used to find the maximum excitation of 3.2 V for the loudspeaker.

The CMOS camera ROI was set to 1 x 250 to increase the sample rate of the detector and the array's location relative to the plate can be seen in Figure 3.7a, which shows a line overlaid upon a full-field (1024 x 1024) time averaged SPI image of the plate vibrating at 242 Hz. The 1 x 250 array from the camera was acquired via a PC that captured a maximum of 5000 samples (the physical limitation of the DAQ buffer size) and then processed using Matlab code. This code calculated the velocity using the theory from Section 3.1 and the deflections shapes to understand the vibration response of the system.

Paramater	Value
Camera frame rate	33 kHz
Line length	1 x 250
Max Velicity	2.16 mm/s

Table 3.1: Summary of HSSPI parameters for testing in Section 3.3.1

3.3.2 Single frequency excitation

The Matlab code resolved the phase measurements captured from the SPI system and calculated the corresponding velocity, this time-resolved data can be seen in Figure 3.7 where the y-axis is the time-data captured (i.e. the data from each frame of the camera) and the x-axis is the 1 x 250 array from the CMOS detector, positioned at the the white line in Figure 3.7a. Figure 3.7 shows the calculated velocity from the array data with the plate excited at 242 Hz. The image shows how the centre of the image is a nodal line (a point of no movement) and the edges are moving sinusoidally

out of phase from each other. This nodal region would correspond to the full-field SPI system image (Figure 3.7a) where the fringes correlate measurements from the HSSPI system.

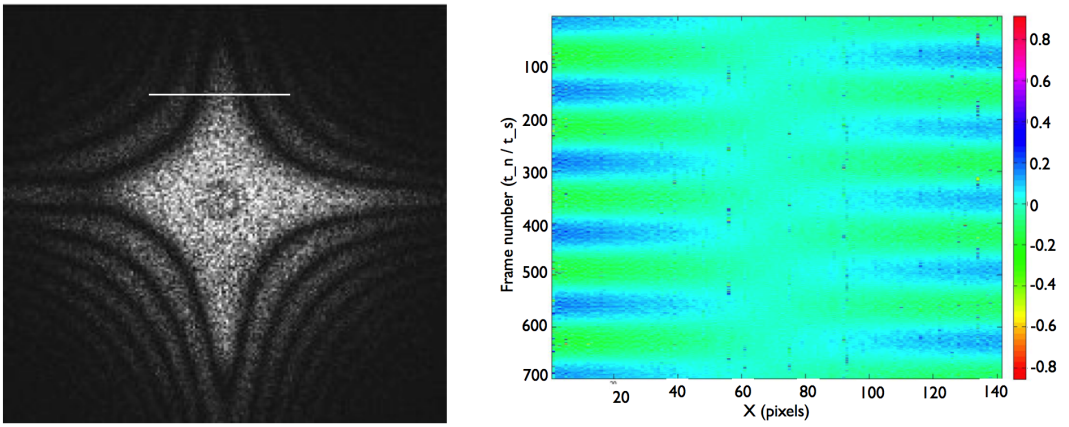

(a) Full field SPI *(b) Multipoint vibrometer velocity measurement*

Figure 3.7: Full field SPI image of the circular plate vibrating at 242Hz; the white line highlights the position of the 1 x 250 array for data capture and the corresponding time domain results of 1x140 pixels from an excitation with the single frequency 242 Hz single frequency (normalised to HSSPI limit)

Applying the fast Fourier transform (FFT) to the time domain data in Figure 3.7 gives the vibration data in the frequency domain. This is a spatial distribution of the frequency component of the vibration data. This is represented in the waterfall plots in Figure 3.8 showing the absolute values of the deflection shapes at their corresponding frequencies. The deflections shapes correspond in both shape and frequency with the simulated analysis and the full-field SPI system observations.

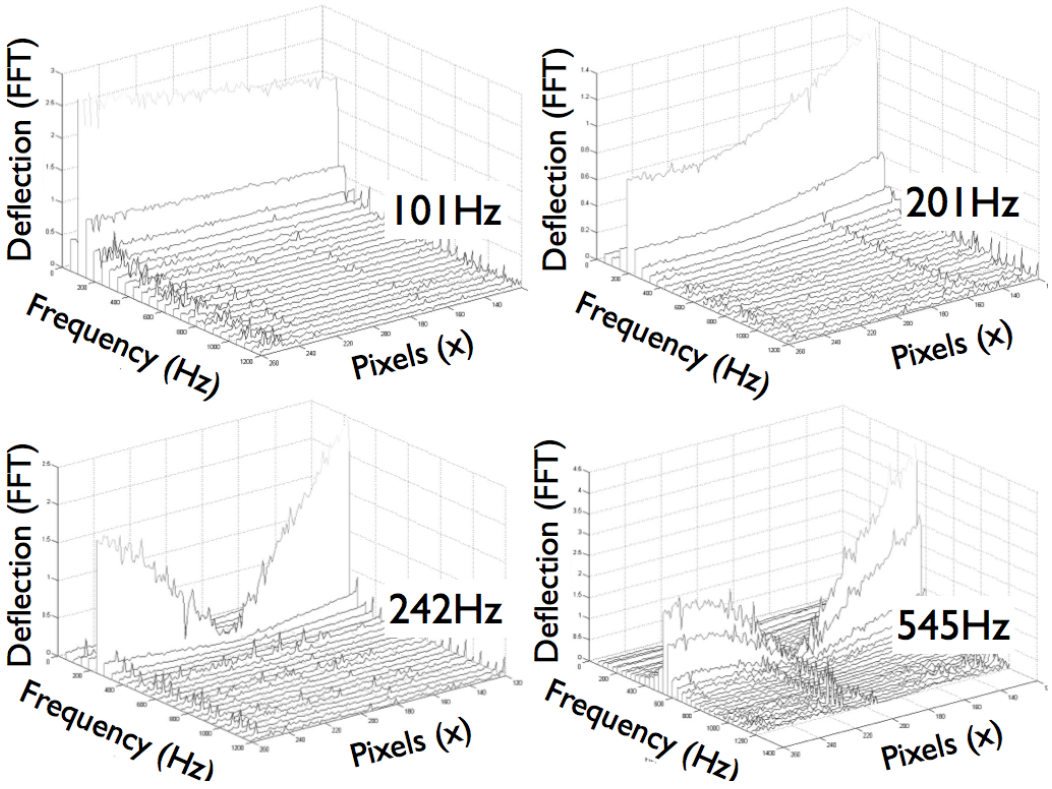

Figure 3.8: Deflection shapes from single frequency excitation

3.3.3 Pulse excitation

The preliminary results from Figures 3.7 and 3.8 give a baseline for comparing the system's performance at capturing transient vibrational excitations of an object. An 500 μs top hat square pulse was sent to the loudspeaker to excite the plate and the CMOS SPI system captured the response data. Figure 3.9 shows the captured intensity (a) and the calculated normalised velocity (b). Again the y-axis is the time corresponding to the frame captured by the system and the x-axis shows the corresponding pixels of the detector array. Evident in each of the calculated data sets (b) is the presence of the ring down effect that a pulse excitation would have, the larger deflections appearing at the top of the images (the instance of the pulse being applied) and the deflections tending towards zero near the bottom of the images (the end of the sample time).

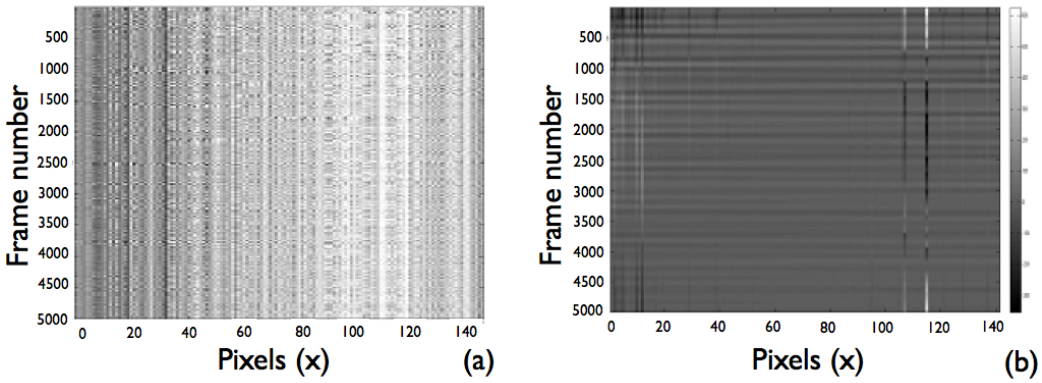

Figure 3.9: Time resolved data from 500μs pulse (a) intensity, (b) normalised velocity

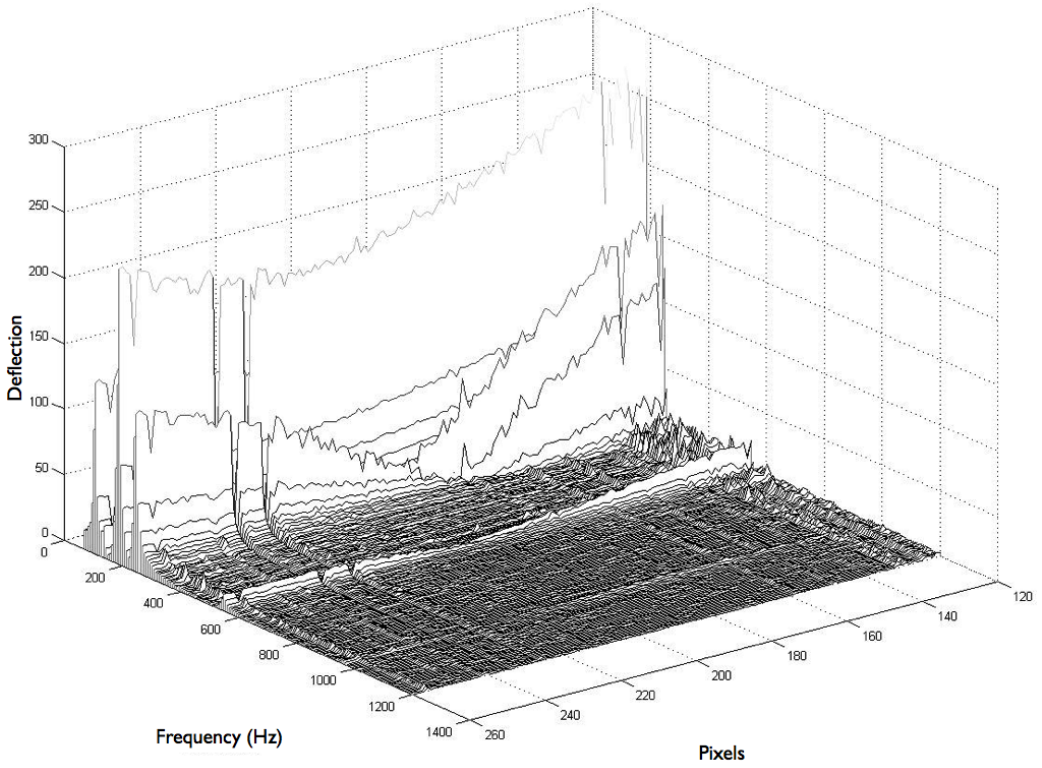

Figure 3.10: Waterfall plot of deflection shapes over the ROI vs Frequency from 500μs sound pulse

The application of the FFT to the time domain data gives the spatial-frequency data that is plotted in Figure 3.10. Comparing this directly with Figure 3.8 both the frequencies and the deflection shapes correlate to what was captured in the single frequency trials.
Figure 3.10 shows that the higher frequency responses appear much weaker than the lower frequencies. The waterfall response at higher frequencies is a limiting factor of using sound as an excitation method: the transmissibility of the air pressure to excite the test object is low, reducing the range of resonant frequencies that can be excited. These tests have extended the simulation work and demonstrated that the system's ability to measure transient events and the use of the Matlab code to process the data, but the excitation needs to have a higher force throughout the frequency range to be useful for modal testing applications.

3.4 Test object for modal testing

The system used in Section 3.3.1 was used to perform modal testing on a new test object: these tests were developed as part of a collaboration with the Atomic Weapons Establishment (AWE). The test object comprised of two plates bolted together at one edge with an overlap of 25 mm, as shown in Figure 3.11. The objects was chosen to produce initial results that could be used as a basis to extend the analysis to more complex structures with overlapping joints. Each plate was 100 mm by 100 mm by 3 mm and made from an aluminium alloy and suspended from the outer corners using rubber ties to simulate free-free boundary conditions. The HSSPI vibrometer results were compared to the results collected at the AWE's test facilities with an accelerometer. The tests were conducted using the two plates and the excitation was achieved using a modal hammer, then the data sets were compared and correlated against an FE model: both the HSSPI and accelerometer results were compared to the same finite element model.

The first 10 natural frequencies were calculated in ANSYS using a CAE model of the test object. These frequencies can be seen in Table 3.2. The AWE's modal test planning software, Optiset [12] used the FE model to calculate the points least likely to cause modal spatial aliasing, points that give a true representation of the vibrations without introducing errors through such things as nodal points. The best 29 ranked points were used for the test locations: these can be seen marked in Figure 3.11, with the circled point of 5181 calculated as the best excitation position, most likely to excite pure modes with little contribution from modal spatial aliasiing. Due to the theory of reciprocity, if the excitation is measured at say point 5181 and the force at point 869, it would produce the same measurement data as measuring the force at 5181 and the response at 869. Meaning the tests can either be completed

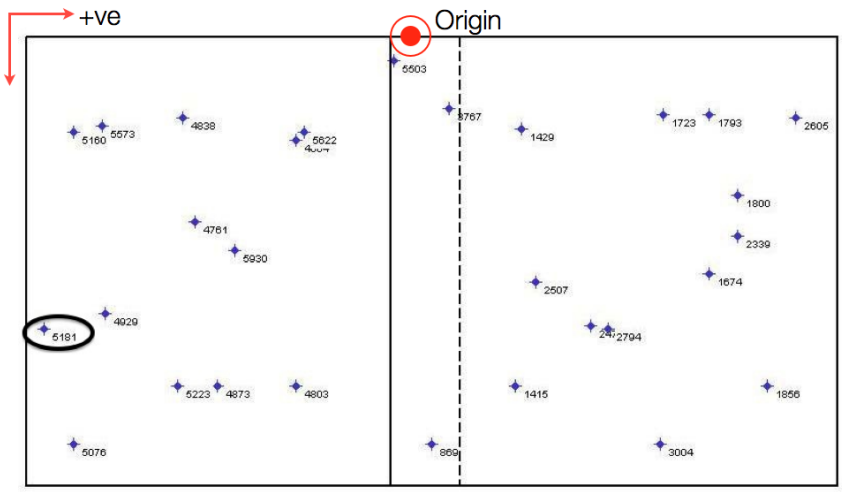

Figure 3.11: Test object consisting of two square plates (100mm x 100mm x 3 mm) with an overlap of 25 mm with the back plate edge indicated by the dashed line. The plates were held together with 3 5mm bolts. The 29 measurement points are marked. The origin point is marked in red and the positive directions for measurement points are shown

The exact measurement positions are in Appendix B.

using the response only measured at 5181 and excite all the other points individually as the accelerator testing in this chapter testing or excite point 5181 individually and measure the response from the different measurement points for each excitation, as with the HSSPI in this chapter. The exact geometric positions of the points used on the plate can be seen in Appendix B.

Mode	Frequency (Hz)
1	182
2	238
3	476
4	553
5	777
6	875
7	911
8	1008
9	1264
10	1327

Table 3.2: First 10 natural frequencies of the two overlapping clamped plates

3.4.1 Accelerometer tests and results

The accelerometer tests were performed at the AWE's test facilities. The accelerometer (Endevco 2250AM1-0) was fixed using wax to point 5181 and the modal hammer (BK8203) excited each of the test points individually and the the FRF data from each of these points was recorded, each point was repeated three times to achieve a moving average response. The modal analysis files, FRF data sets, were saved and processed

in Modal analysis software, ICATS Modent, was used to extract the modal data from the FRF data sets, using the modal extraction techniques from Section 2.1.3. The modal data was then used with ICATS Modesh to correlate against the FE data.

A typical FRF from the accelerometer data can be seen in Figure 3.12 this is the drive point FRF when the response and excitation measurement point are both at 5181, where the resonant frequencies can be seen from the peaks in the data and the phase change of 180 degrees in the phase. Figure 3.13 shows the output of this correlation. The correlated mode pairs for the natural frequencies correlation is shown on the left and on the right is the resulting modal assurance criterion (MAC). As expected from a developed and standard measurement process, the accelerometer FRF results provided accurate measurements with high sensitivity over a wide frequency range, demonstrated by the high correlation against the FE results in Figure 3.13.

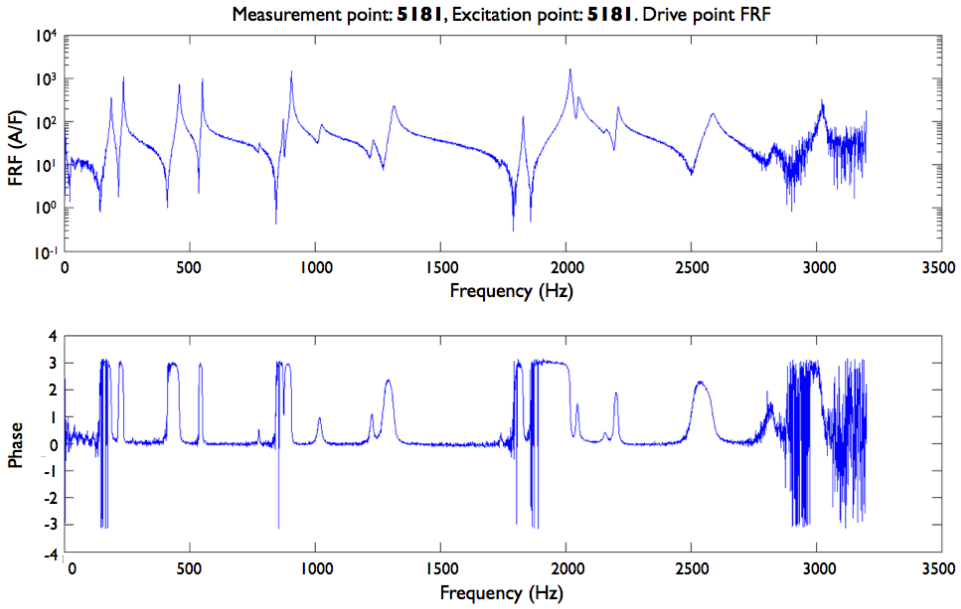

Figure 3.12: Drive point FRF from accelerometer position 5181 and excitation position 5181 showing the FRF response (upper image) and the corresponding phase (lower image)

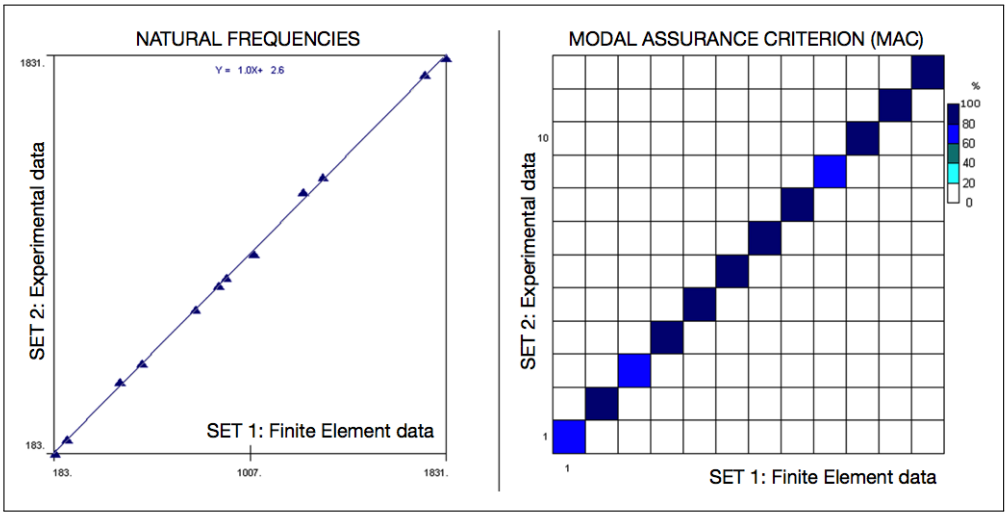

Figure 3.13: FE and accelerometer modal data correlation, (Left) Natural frequency comparison. (Right) MAC

3.4.2 Multipoint vibrometer tests and results

As opposed to a fixed response point and moving the excitation position, the multi-point vibrometer tests were conducted by keeping the excitation point fixed in a single location and changing the pixels of the camera to capture the different response points. Point 5181 was used as the fixed excitation position and six ROI were identified to capture the test data. Each of the test points related to a pixel on the CMOS detector and employing the ability of the detector to examine user-defined ROI, the relevant pixels were selected and the vibration response captured at these coordinates, each of the test lines were 1 x 256 pixels long. Both the excitation point (5181) and the six ROI for the test used are highlighted in Figure 3.14. The test object was suspended just as in the accelerometer tests and the response was measured using the HSSPI system described in Section 3.3.1.

Paramater	Value
Camera frame rate	20 kHz
Line length	1 x 256
Max. Velocity	1.31 mm/s

Table 3.3: Summary of HSSPI parameters for modal testing in Section 3.4.2

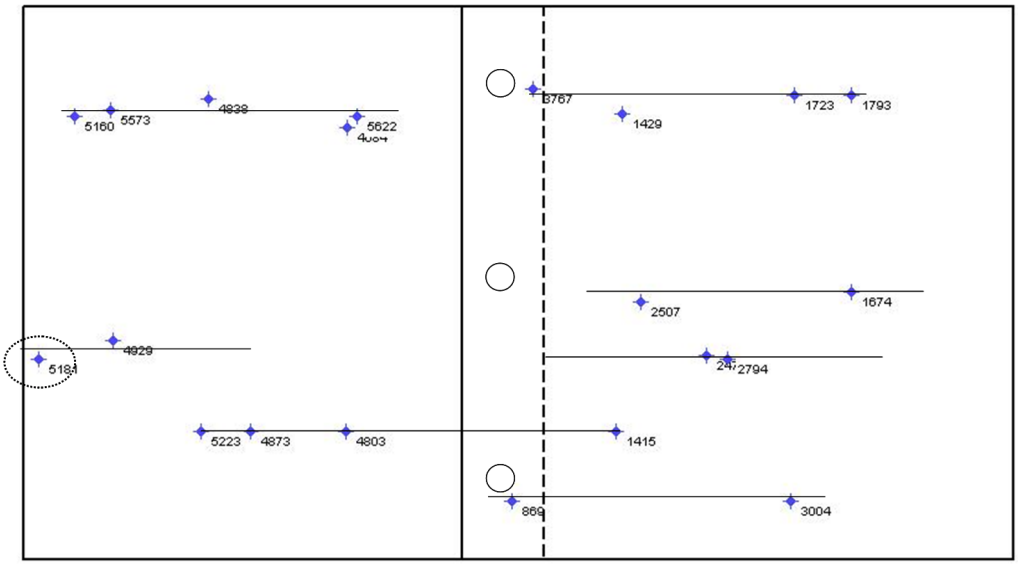

Figure 3.14: Test object with 7 ROI and the excitation point marked

For each excitation the ROI of interest was selected for each line shown in Figure 3.14 and the measurement system was triggered from the modal hammer's impact signal. The ROI was then moved to the next line to repeat the test process. The force data was recorded on a digital oscilloscope and the CMOS detector's signal was captured in a Labview acquisition environment. Both data sets were imported to Matlab to create the FRF files, and Matlab scripts were created to convert this response data into the correct ICATS format for modal analysis.

The output from the multipoint vibrometer was processed in Matlab to extract the quantified response measurements. The output data from the HSSPI is an array (1 x 256 pixels) of intensities varying with time as can be seen in Figure 3.15aa, where each horizontal row represents a frame capturing an ROI from the camera and is a measure of the intensity. However, the line length was reduced to 1 x 160 as the intensity strength at the edges of the full line had low intensity values leaving data with high noise. The intensity is processed within Matlab using the same process used in 3.3.1 to calculate the surface velocity of the plate, Figure 3.15b, where the ring down effect from the impact can be seen down each of the parallel columns.

A fast Fourier transform (FFT) is applied to give the two data sets in the frequency domain which are used to produce the Mobility FRF function. Figure 3.16 shows the waterfall FRF of the data from Figure 3.15. Showing the FRF in this way enables the operational deflection shapes (ODS) to be quickly seen and the resonant frequencies quickly identified. In this case they are 96 Hz, 211 Hz, 248 Hz, 458 Hz, 552 Hz, 724 Hz, 860 Hz and 906 Hz. Each pixel that is related to a test point is then converted into ICATS format (CRD & FRF files), using the Matlab scripts developed so they can

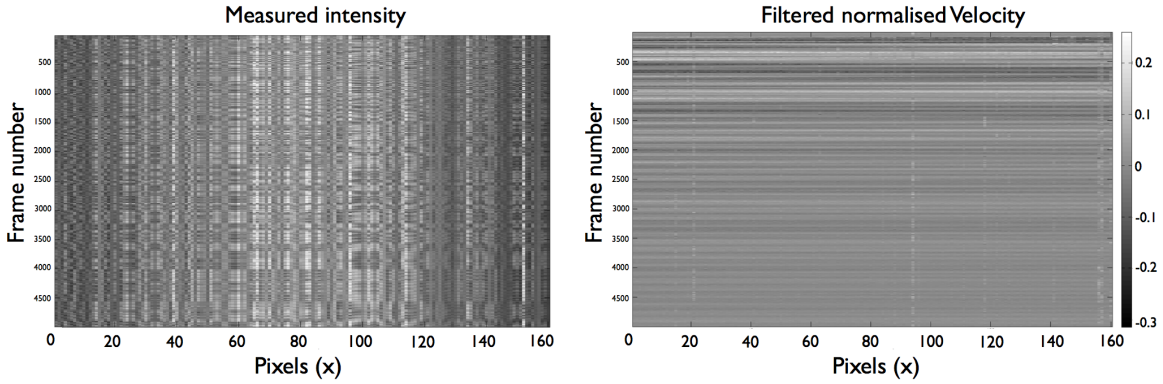

(a) Intensity against frame number *(b) Normalised velocity against frame number*

Figure 3.15: Vibrometer output Signal

be read and processed. As with the accelerometer data, ICATS Modent was used to extract the modal data and ICATS Modesh was used to correlate the results against the FE data. The results can be seen in Figure 3.17 and 3.18 which correspond to 16 and 21 coordinates respectively, which are the same points as the accelerometer data for direct comparison. Again, the natural frequency comparison is on the left and the MAC on the right. The results show that the HSSPI is capable of producing high natural frequency correlation against the FE results, but although the MAC has some degree of correlation, there are sources of errors not seen in the accelerometer results.

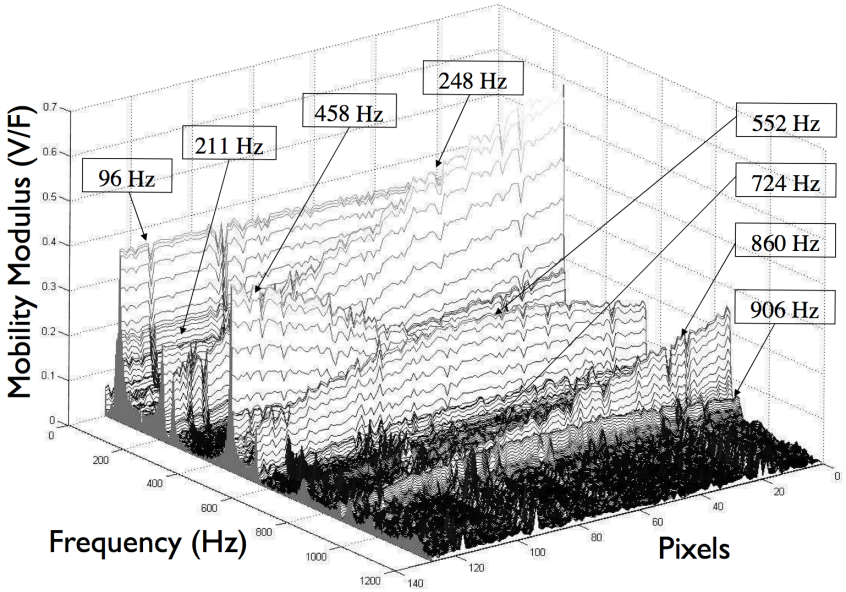

Figure 3.16: 3D FRF of vibrometer results from an ROI with resonances shown

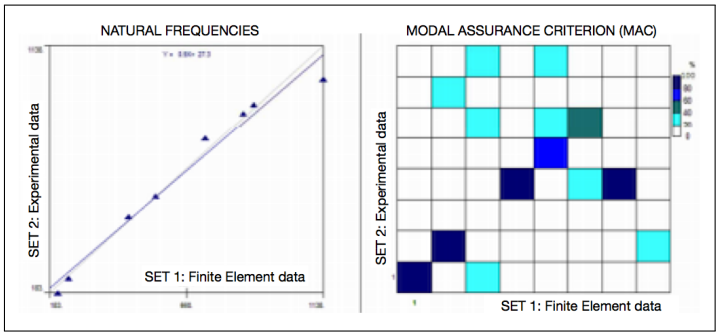

Figure 3.17: FE and 16 point multipoint vibrometer modal data correlation, (Left) natural frequency comparison. (Right) MAC

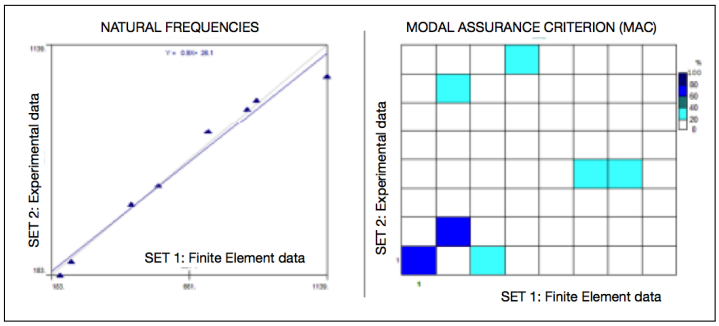

Figure 3.18: FE and 21 point multipoint vibrometer modal data correlation, (Left) natural frequency comparison. (Right) MAC

3.5 Discussion

The experimental results for the multipoint vibrometer (Figures 3.17 and 3.18) demonstrated that the system can produce a good natural frequency correlation, the range was lower than similar accelerometer results but has the same degree of correlation over its shorter range. The multipoint vibrometer system had a smaller data acquisition buffer length (a current hardware limit of 5000). This buffer length restricted the frequency range and frequency resolution of the measurements, i.e. 8 natural frequencies and 6.6 Hz resolution that the vibrometer could measure in its usable range compared to the 12+ from the accelerometer at 0.5 Hz resolution. However, this is a technical restriction that can be resolved with the introduction of new hardware with a larger buffer capacity of 20000 to reach a 1 Hz resolution. The MACs in Figures 3.17 and 3.18 show that the system produced correlated modal results although currently of inferior quality to the accelerometer results, Figure 3.13.

Unexpectedly, the 16 point correlation produced a higher quality of MAC than the 21 point correlation: usually decreasing the number of test points increases the chance of spatial aliasing errors.

To understand this the raw velocity data was investigated. Figure 3.19b shows the velocity calculated from a single column of the multipoint vibrometer and the

corresponding data from a Polytec single point vibrometer recorded in a subsequent test with a comparable force level. Both signals ring down after impact as expected, but the single point vibrometer measurement shows a measured velocity of 3 mm/s, well in excess of the 1.4 mm/s velocity limit of the multipoint system. (The velocity limit for the multipoint system is set by the Nyquist limit for sampling the interference signal, [1, 107]).

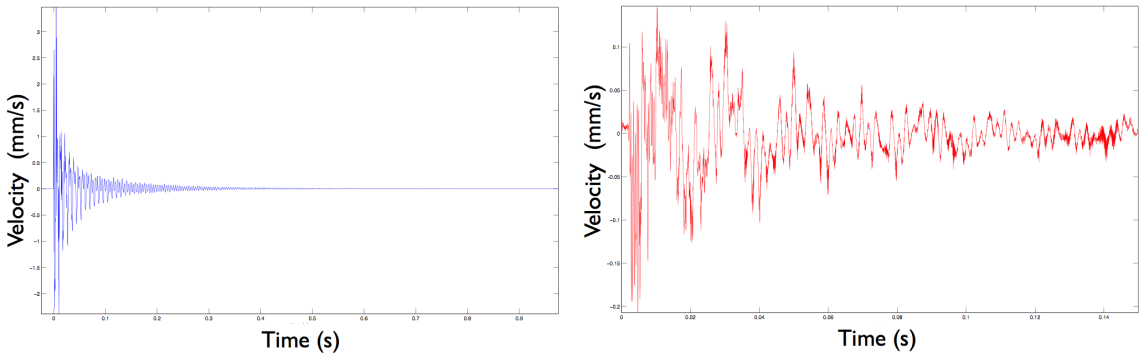

(a) Polytec vibrometer velcity signal *(b) Multipoint vibrometer velocity signal*

Figure 3.19: Comparison of captured velocities

It is evident from Figure 3.17 that the natural frequencies can be accurately extracted from the discontinuous data, but the recovered modeshapes have errors introduced, as well as possible distorted phase data, leading to a poorer MAC. It was determined that the experiments reported were already at the lowest force input achievable in practice, and that reducing the force input for these trials would simply reduce the signal to noise ratio of the recovered velocity signal. This reduction in force wouldn't address the significant issue of the multipoint vibrometer's maximum velocity limit, and to continue with modal testing the dynamic range must be increased.

3.6 Chapter summary

This Chapter has shown the application of a temporal phase-stepped high-speed SPI multipoint vibrometer system for modal analysis for the first time. The multipoint vibrometer results showed promising results especially with the production of the operational deflection shapes and resonant frequencies quickly over user-defined ROIs. However, the calculated MACs were shown to contain larger errors than for the accelerometer tests due to the much lower surface velocity measurement range of the multipoint system.

The next Chapter will focus on using spatial phase-stepping techniques to increase the measurable surface velocity by a factor of three in an attempt to improve the MAC quality and demonstrate the vibrometer's suitability for general modal analysis.

Chapter 4

Modal testing using HSSPI with spatial phase-stepping

With the knowledge gained from the temporal experiments in the previous Chapter the HSSPI's dyanmic range must be increased to improve the quality of the modal analysis. This increase was achieved through a spatial phase-stepped system that has three times the dynamic range of the temporal system. The spatial phase-stepped SPI system used a high-speed CMOS camera as a multipoint vibrometer which increased the velocity from $\pm 0.3\ \nu_{Nyq}$ to $\pm 1.0\ \nu_{Nyq}$, a velocity of 2.7 mm/s. To ensure the system stayed within its measurable velocity limits the maximum velocity of the excitation was restricted. The hammer tip and its force gauge was fixed to an electromagnetic shaker that provided finer control to limit the input pulse for impact excitation. A single point LDV measured the velocity at the excitation point, and any measured excitation from the shaker pulse that gave a velocity response higher than 2.5mm/s was rejected and repeated until a measurement was taken within this range. These conditions and the faster measurement capabilities of the spatial system was used to repeat the modal testing seen in Chapter 3 on the two overlapping square plates with impact excitation.

This Chapter describes the set-up of the spatial system used to perform the modal testing and includes simulations of the spatial system for vibration analysis. The results of the modal testing are compared to an FE model and the temporal experimental results and then discussed in the close of this Chapter.

4.1 Experimental system for experiments

The spatial HSSPI system used for modal testing was developed at Heriot-Watt University (HWU) by Wu et al [2] and was a development of the temporal system in Section 2.2.2.

Paramater	Value
Camera frame rate	25 kHz
Line length	1 x 656
Max. velocity	2.77 mm/s

Table 4.1: Summary of HSSPI parameters for modal testing in Section 4.1

The schematic diagram of the experimental system is shown in Figure 4.1, where: the output from a diode-pumped, frequency doubled Nd:YVO4 laser (single-frequency continuous-wave output at 532 nm at power levels up to 5 W) was divided by a polarizing beamsplitter (PBS) into orthogonally linearly polarised object and reference beams. Each beam was launched into the fast axis of a highly-birefringent (Hi-Bi) optical fibre. The output power of the laser was below 500 mW in order to prevent damage to the fibre ends. Two gratings are placed before each of the beams enter the beam splitter (BS) as seen in Figure 4.1. This has the effect of splitting the beams into a two channelled system. The two gratings were calibrated to have a phase difference of 90 ° from each other: meaning each channel that was separated by the gratings captures complementary intensity data during the vibration period. The two identical binary gratings had a nominal pitch of 38 μm. The phase modulation depth of the gratings was originally designed to suppress the 0, $\pm$2, $\pm$4, etc. diffracted orders at 532 nm for a shape measurement illumination system that projected interference fringes between the +1 and -1 diffracted orders.

The physical set-up of the optics is similar to that used in temporal phase-stepped HSSPI and used the same CMOS camera, with the user-defined ROI ability described earlier. The difference between the two systems was how the system introduces phase-stepping. The previous Section used temporal phase-stepping to resolve vibration data by capturing a minimum of four images per vibration cycle and used the Carré algorithm to calculate the phase to then extract the velocity. The Nyquist sampling frequency limits the maximum velocity the temporal HSSPI system can measure. This velocity limit can be increased with the use of spatial phase-stepping, which enables SPI to act as a dual channel system with a fixed phase step between the two channels. The spatial phase-step removes the sampling per cycle limitation the temporal system had, allowing faster velocity to be captured. The PM in the system is only included for calibration of the system, but this is not used for operation of the HSSPI system.

The system similarities of the spatial and temporal system can be seen in Figure 4.2, which show the spatial system's dual channels capturing vibration data with the use of temporal phase-stepping. The two channels can be clearly seen in 4.2a which shows the intensity across the array of the detector and the frame number running down the image. Figure 4.2b shows the calculated phase from the Carré algorithm

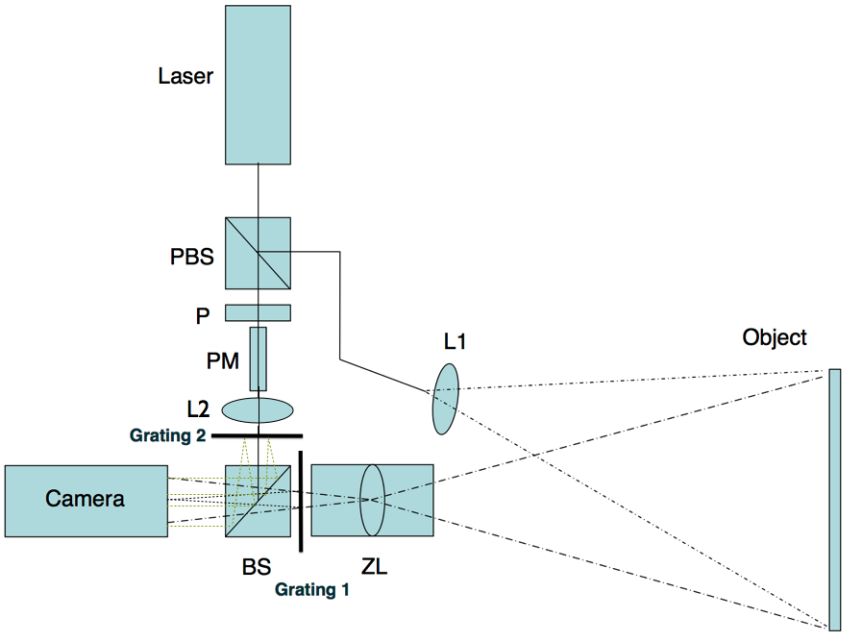

Figure 4.1: Schematic of Spatial phase stepped HSPI experimental set-up. PBS polarising beamsplitter; P polariser; PM phase modulator (used for calibration only), L1 optional cylindrical lens; BS beamsplitter and ZL zoom lens. showing Grating 1 and Grating 2 locations

(from Equation 3.4 in Section 3.1) used to resolve the velocity in Figure 4.3. These figures show the similarities of the physical set up of the two systems but there is no spatial phase-stepping in these figures only temporal phase-stepping.

The detector of a spatial phase-stepped interferometer measures an intensity at the corresponding pixels $(x, y)_N$ where N is the number of separate regions on the detector at a particular instance t_n, and that intensity can be represented by:

$$I_{n,N}(x, y, t_n) = I\left\{1 + \gamma_O sinc\left(\frac{\Delta}{2}\right) cos(\Phi_O - \Phi_R)\right\} \tag{4.1}$$

this is identical to 3.3 but in this case each of the separate regions introduce a constant phase-step of $\Phi_R = (N-2)\pi/2$ between each region. When there is two detectors, $N = 2$, as in our case, the relative phase difference, Δ between the object and reference beam has a constant phase change and can be calculated at each pixel can be calculated [146]:

$$\Delta\Phi_O(t_n) - \frac{\pi}{2} = 2tan^{-1}\left(\frac{I_{n-1,N} - I_{n,N-1}}{I_{n-1,N-1} - I_{n,N}}\right) \tag{4.2}$$

The system is capable of unwrapping adjacent frames, even if the phase change exceeds

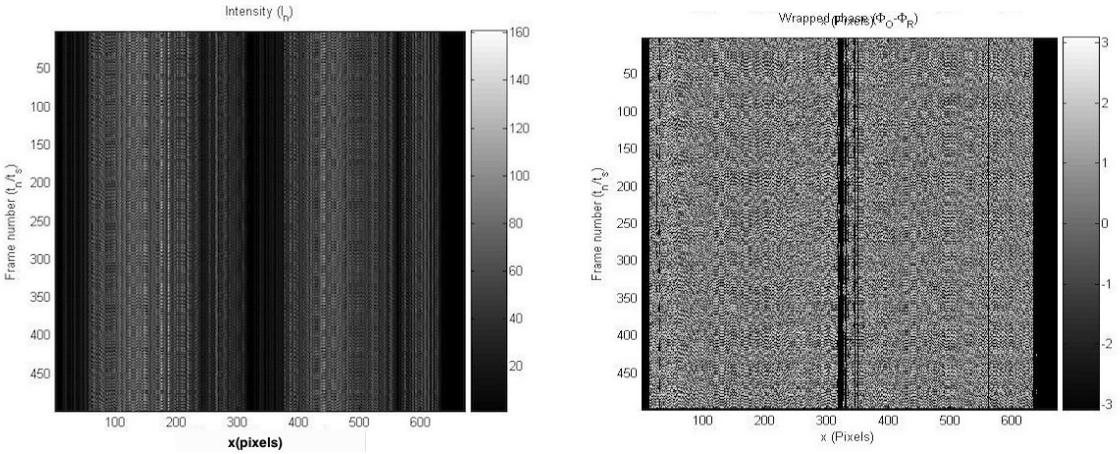

(a) intensity measurements for each frame *(b) Phase calculated from the Carré algorithm*

Figure 4.2: Spatial system operating as a temporal system

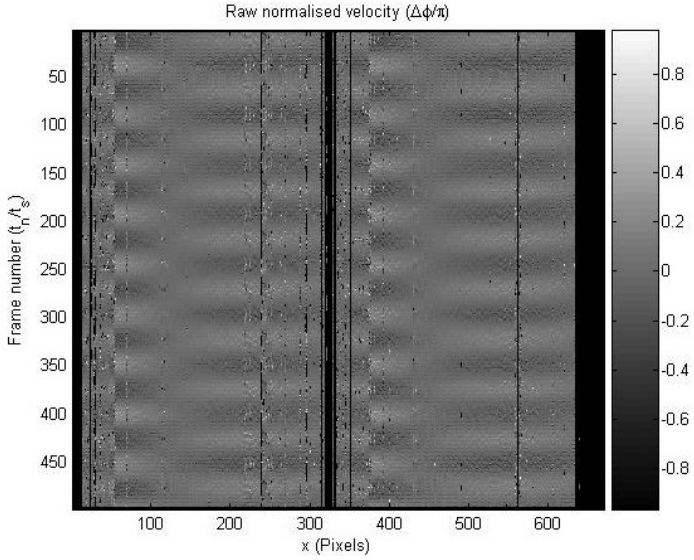

Figure 4.3: Calculated velocity of the spatial system operating as a temporal phase-stepped system

π radians, by assuming the velocity is continuous [2, 147]. The measured velocity is wrapped in the range $\pm V_{Nyq}$ that translates to a modulo of $2V_{Nyq}$, meaning that the unwrapping algorithm can add multiples of $2V_{Nyq}$ to correct the normalised velocity at each pixel:

$$\frac{\overline{\Delta\Phi_O(t_n)}}{\pi} = \frac{\Delta\Phi_O(t_n)}{\pi} \pm k2\mathcal{V}_{Nyq} \tag{4.3}$$

where $\overline{\Delta\Phi_O(t_n)}/\pi$ is the unwrapped normalised velocity, $\Delta\Phi_O(t_n)/\pi$ is the measured normalised velocity modulo $2V_{Nyq}$ and k is an integer.

As factors of $2V_{Nyq}$ are automatically added or subtracted during the unwrapping process, to calculate the absolute velocity (when $k = 0$) a reference point is needed to be measured. Limits to the system are not determined from the velocity limit,

as in the temporal phase-stepped system, but from the acceleration limit. This is determined from the difference between a normalised velocity that produces a V_{Nyq} between a frame change and can be used to form the expression for the acceleration:

$$w_n''(x, y, t_n) = \frac{\lambda \Delta^2 \Phi_O(x, y, t_n)}{2\pi\eta t_s^2} \tag{4.4}$$

or rewritten to include V_{Nyq} the acceleration becomes:

$$\frac{w_n''(x, y, t_n)}{\frac{\mathcal{V}_{Nyq}}{t_s}} = \frac{\Delta^2 \Phi_O(x, y, t_n)}{\pi} \tag{4.5}$$

Where $\Delta^2\Phi_O(t_n) = \Delta^2\Phi_O(t_n+1) - \Delta^2\Phi_O(t_n)$ represents the rate of change of phase difference between frames. Setting $\Delta^2\Phi_O = \pi$ into Equation 4.5 gives the acceleration limits for sub-Nyquist interferometry:

$$a = \frac{\mathcal{V}_{Nyq}}{t_s} \tag{4.6}$$

this limit is a theoretical limit but in practical systems this would be limited by the camera's exposure, that was demonstrated by Wu et al [2].

4.1.1 Binary grating alignment

To achieve the required spatial phase-shift a pair of binary gratings were introduced into the system. The use of binary gratings for spatial phase stepping was first implemented by Wu et al [2]. One grating was placed into the reference beam path and the second in the object beam path. Each binary grating was designed to eliminate the even diffraction orders for the YAG laser's wavelength, 532 nm, and have a nominal pitch of 53μm. The removal of these orders mean that the +1 and -1 diffracted orders were more dominant and suitable for this type of analysis. This introduces a double-wave front into the system that was captured by the CMOS detector. For the wave front to be used for spatial phase-stepping a $\pi/2$ phase shift was needed to be finely calibrated between the grating pairs. Accurate alignment of the gratings was critical to the phase-stepping performance and assuming the speckle size was approximately the size of a pixel on the detector a calibrated system needs sub-pixel alignment. The two axes that are critical for dual channel alignment are: the translational alignment (x, y on the viewing plane) and the rotational alignment (around the viewing plane). The sub-pixel alignment of the object beam was applied on the x and y axis and then the rotation position. The reference beam was then matched to the object beam and the same sub-pixel alignment was applied with the object beam blocked. The final stage was to ensure the relative orientation of the object and reference gratings

was correct for location and step-size for π /2. A microbench translation stage, built into the system, was used to aid in the alignment and used for both the translation alignment (x, y) and to refine the phase-shift between the gratings in the viewing path.

To quantify the accuracy of sub-pixel alignment an image correlation technique was used in Labview. The image correlation uses Equation 4.7 below [2]:

$$r = \frac{\sum_x \sum_y (A_{xy} - \bar{A})(B_{xy} - \bar{B})}{\sqrt{\left(\sum_x \sum_y (A_{xy} - \bar{A})^2\right)\left(\sum_x \sum_y (B_{xy} - \bar{B})^2\right)}} \tag{4.7}$$

where A and B are the separate images created from the dual-channel gratings and $\bar{A}$ and $\bar{B}$ are the mean intensities of the pixels across each image. An r value of 1 represents perfect correlation and 0 means no correlation. This correlation was used independently for the object beam and the reference beam, then again for when they are combined. The alignment of the object beam was most difficult due to intensities being less uniform across the image, a minimum correlation coefficient of 0.93 was used for the object beam. The reference beam was more straightforward and a correlation coefficient no less than 0.98 was used for the system. The final stage of correlation was to achieve an accurate phase-step between the pairs of gratings. This was adjusted by small movements of the grating along the viewing path and was measured by introducing a temporal phase-step between image acquisitions of a stationary object. The images were processed in Matlab using a 4-step algorithm and adjustments were made until the pixels show a phase shift of $\pi/2$.

4.2 Simulation work

To understand the performance of the spatial phase-stepped HSSPI system, simulations were created in Matlab. These simulations used the same principle as the temporal phase-stepped simulations in Section 3.1: to understand the response of the system's characteristics (introduced in Section 4.1) to single frequency excitation and multi-frequency excitation.

Figure 4.4 shows the simulation of spatial phase stepping for a vibration amplitude of $0.5v_{Nyq}$ with a single vibration frequency of 211Hz. The figure shows the simulated intensity over 500 frames (increasing down the columns), that were equally sampled on x_N (the 2 separate regions on the single detector) and calculated at time t_n from Equation 4.1. The system parameters were the same as the temporal phase-stepped system, λ= 532 nm and $\eta = 2$ and the framerate set to 25kHz. The random speckle phase in $\Phi_O(x, t_n)$ was set to zero in order to visualize the process more clearly.

The intensity was used to calculate the wrapped phase from Equation 4.2 which can be seen in Figure 4.5, from which the normalised velocity was calculated as seen in Figure 4.6, using the unwrapping algorithm, Equation 4.3. The velocity can be represented as a 3D waterfall plot (Figure 4.7) in the frequency domain from FFT transform, this shows the deflection shape of the excitation frequency.

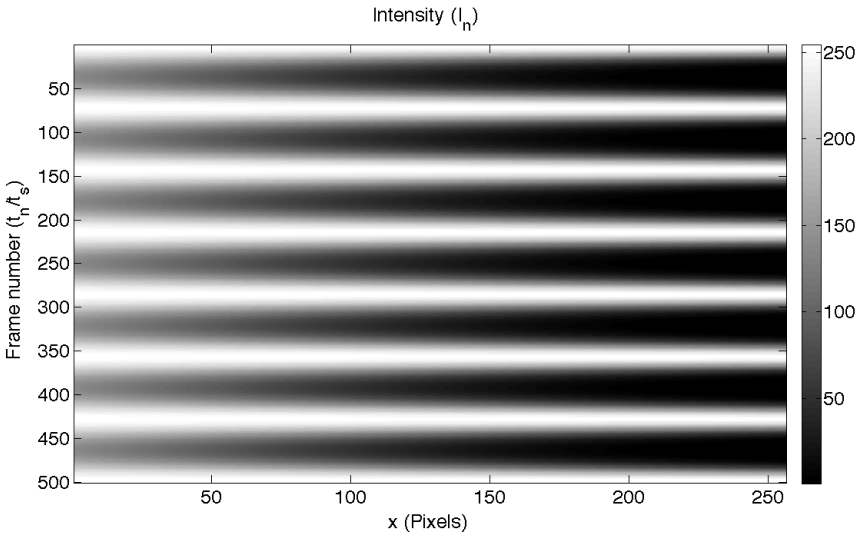

Figure 4.4: Calculated intensity vs frame number

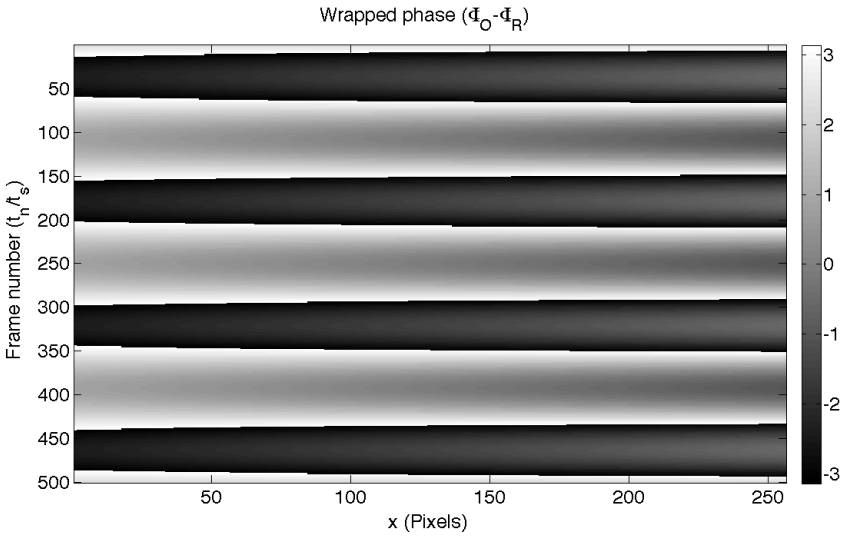

Figure 4.5: Calculated wrapped phase vs frame number

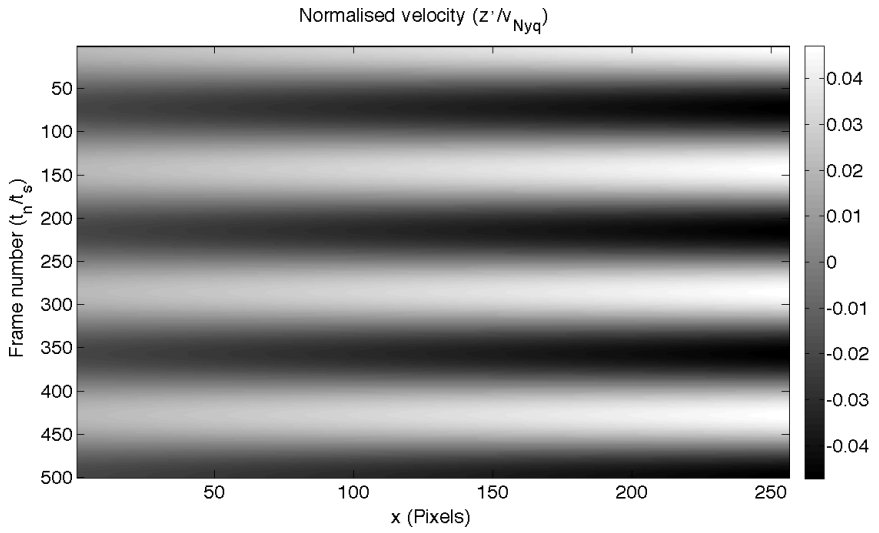

Figure 4.6: Single frequency simulation velocity against frame number

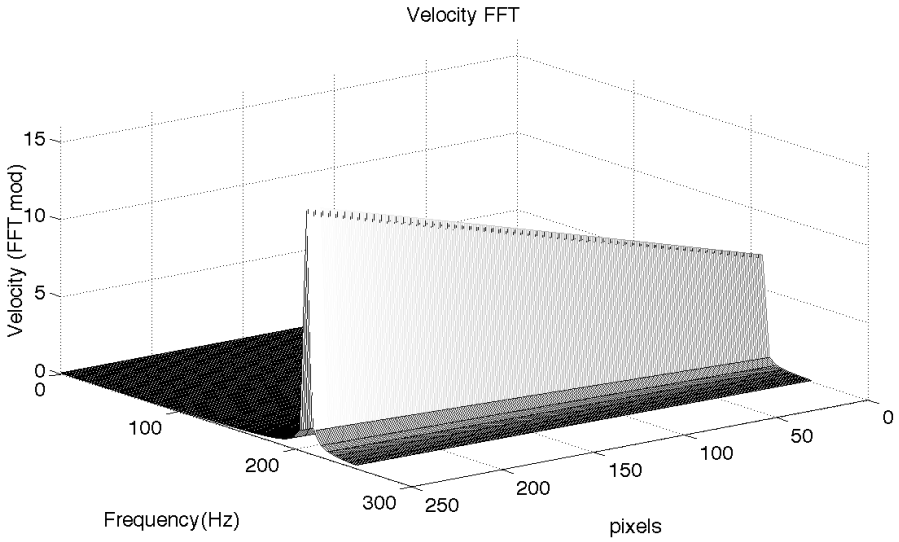

Figure 4.7: Single frequency waterfall plots velocity array against frequency

These initial simulations demonstrated the system's response to calculate a single frequency excitation but there is a need to understand the system's response to multi-frequency excitation to know the expected performance of the system for modal testing with a modal hammer. To represent this transient excitation a sum of multiple frequencies were used as inputs into the simulation. These were based on the same frequencies seen in Section 3.2 based on the expected resonant frequencies of the the test object of: 98 Hz, 211 Hz, 248 Hz, 458 Hz and 552 Hz.

The multi-frequency simulation takes the same form as the single frequency, where the intensity measured by the simulated system, taken from Equation 4.1, can be seen in Figure 4.8. The wrapped phase is calculated from this using Equation 4.2 and can be seen in 4.9.

The phase is unwrapped and gives the calculated velocity shown in Figure 4.10 and can be represented in the frequency domain with a 3D waterfall plot as shown in Figure 4.11 where the deflection shape of each of the individual excitation frequencies can be seen. These results demonstrate and validate the theoretical process for extracting multiple frequencies from a simulated spatial phase-stepped system was possible and can used as the basis for extracting experimental data.

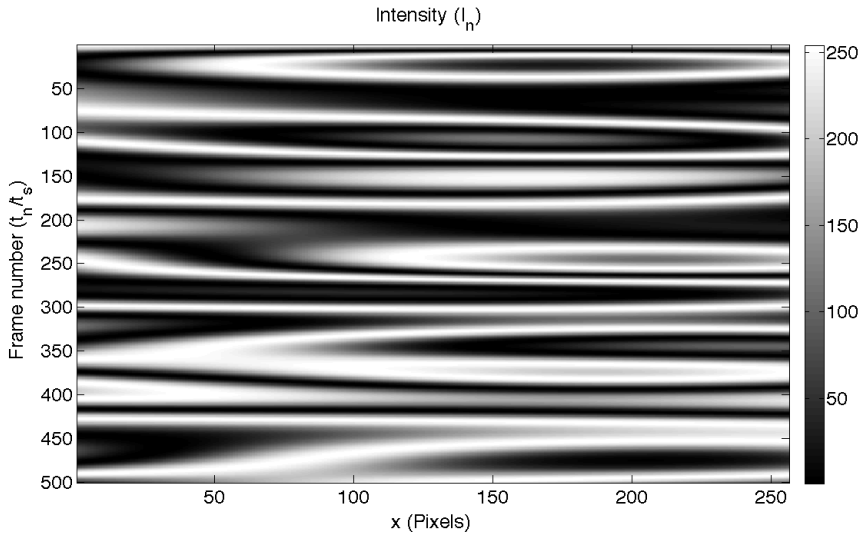

Figure 4.8: Calculated intensity vs frame number from spatial system simulation with multi-frequency excitation

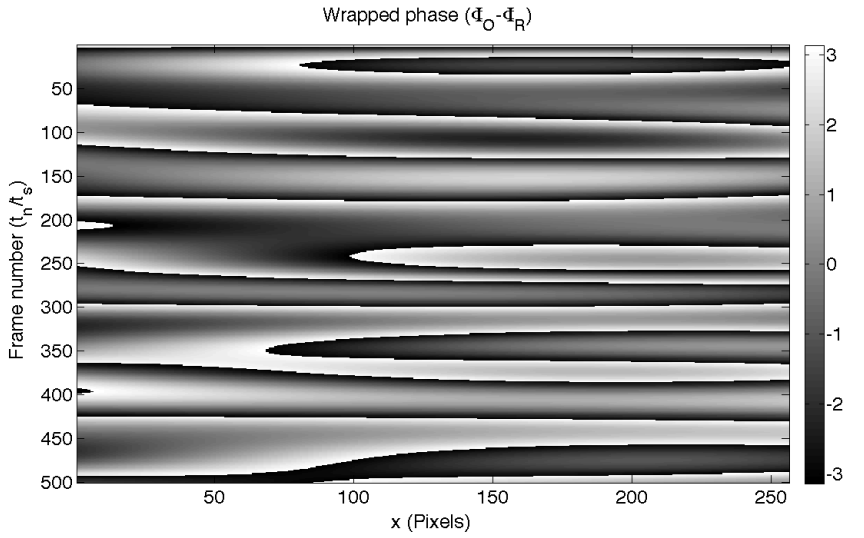

Figure 4.9: Calculated wrapped phase vs frame number spatial system simulation with multi-frequency excitation

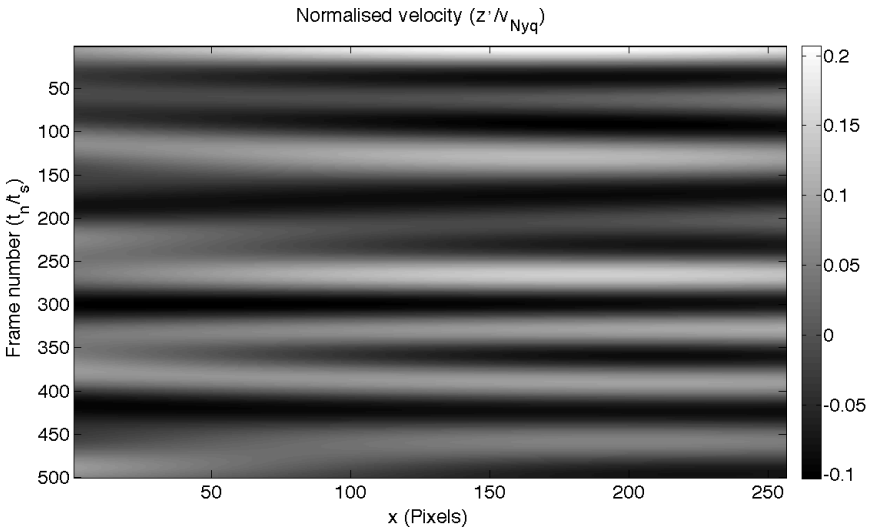

Figure 4.10: Multi-frequency simulation velocity

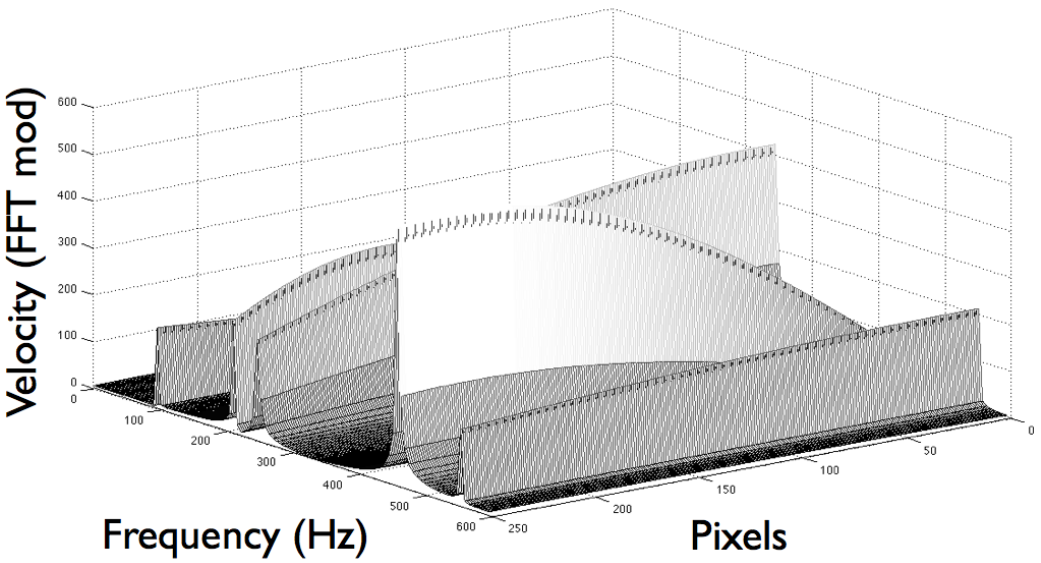

Figure 4.11: Multi-frequency waterfall plots of simulated velocity array against frequency

4.3 Test object for modal testing

The two overlapping square plates used in Section 3.4 were used as the test object to perform modal testing with the spatial phase-stepping system. The test object of two plates clamped together at one edge with an overlap of 25 mm, shown in Figure 4.12. The test object was suspended from the outer corners using rubber ties to create close to free-free boundary conditions and the two plates were fixed together with bolts at the overlapped edge. The modal hammer's head and force gauge (B&K Type 8203) was attached to a shaker (B&K Type 4810) to give finer control of the maximum force and velocity of excitation pulse. A function generator sent a 500 μs pulse to the shaker that provided the impact hammer pulse to measurement point 5181. A single point LDV (Polytec OFV-534) was set up to measure the velocity response to the impact pulse and if the measured velocity was over 2.5 mm/s (below the system's maximum: 2.7 mm/s) the HSSPI was rejected and the force level reduced on the shaker. The measurement points were measured with the spatial system using the same lines as the temporal system and can be seen in Figure 4.12. The different lines were captured by changing the pixels in the CMOS detector. The force data from the modal hammer's force transducer was recorded on a digital oscilloscope and the CMOS detector signals were captured with the same LabView acquisition system. Measurement acquisition was triggered to start from the modal hammer's impact signal and both signals were imported to Matlab for signal processing then converted to ICATS file format for modal analysis. The data sets were then compared and correlated against the FE model, the correlations were then compared to the accelerometer and the temporal results to compare the quality of the results.

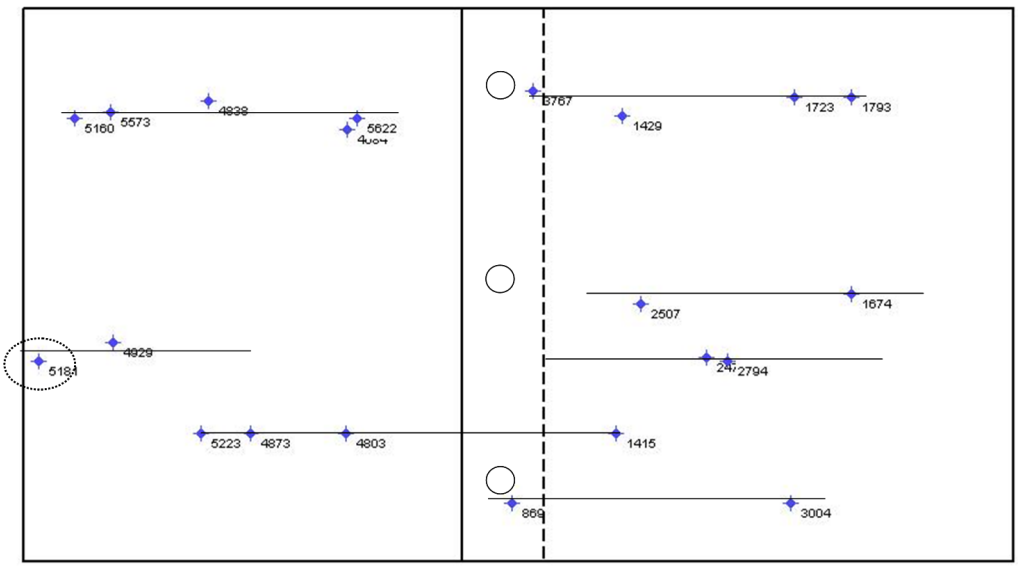

Figure 4.12: Test object with 7 ROI and the excitation point marked

4.4 Results

The spatial phase-stepped results were processed in Matlab to create the FRF functions needed for modal parameter extraction in ICATS. Figure 4.13 shows the captured intensity from the spatial phase-stepped system, this is intensity measured across the 656 x 1 array at the drive point line seen in Figure 4.12. As the simulation in Section 4.2, the wrapped phase was calculated from the intensity with the use of Equation 4.2 and can be seen in Figure 4.14. The unwrapping algorithm was then used to unwrap the phase to give the velocity profile seen in 4.15. The dual channels of the spatial system can be seen in the intensity Figure 4.13 before the the phase was calculated in Figure 4.14 that joins the separate data from the two channels into a single measurement. Applying an FFT to both the velocity data and the force data then dividing the velocity by the force produces the mobility FRF function. Figure 4.16 shows the FRF across the array of the data, Figure 4.17 shows the same data from an aerial view of the frequencies.

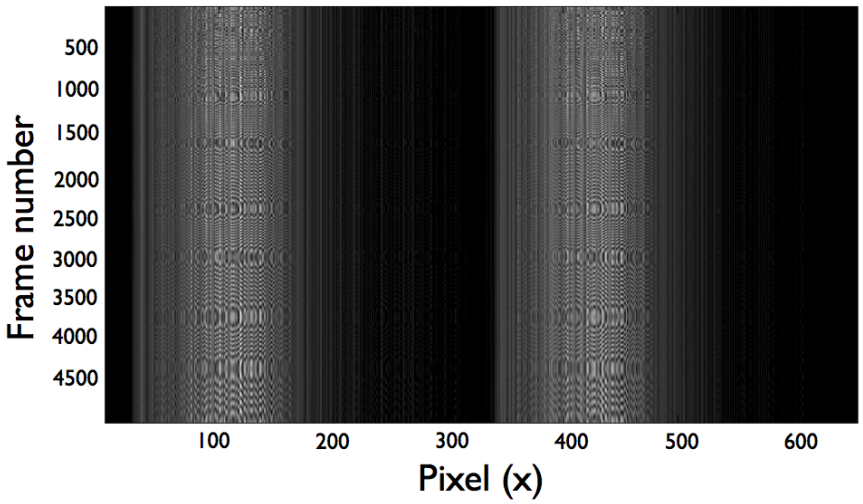

Figure 4.13: Measured intensity vs frame number from spatial phase-stepped system

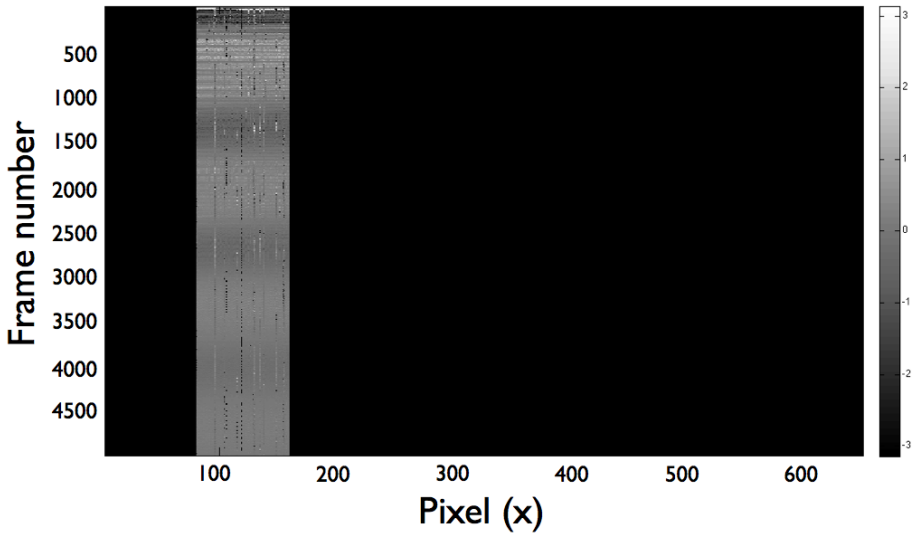

Figure 4.14: Calculated wrapped phase from spatial phase-stepped system from spatial phase-stepped system

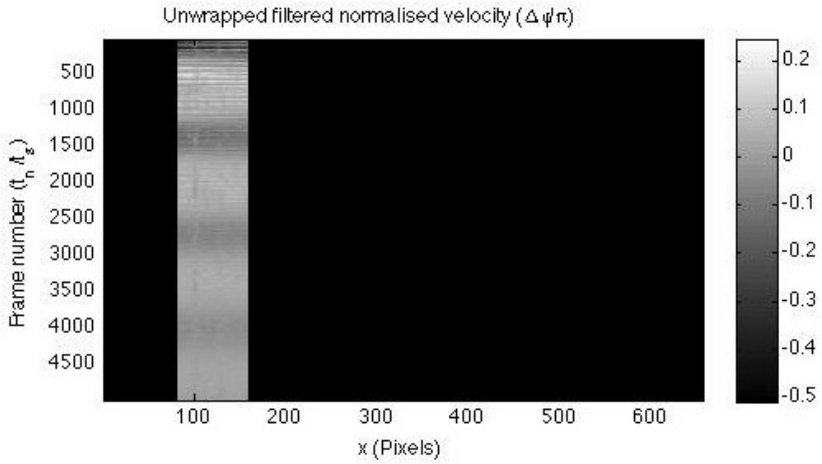

Figure 4.15: Spatial phase stepping velocity data from line 4 of modal testing, for each frame. The dark area is the unused data after the two grating areas have been used to calculate the velocity

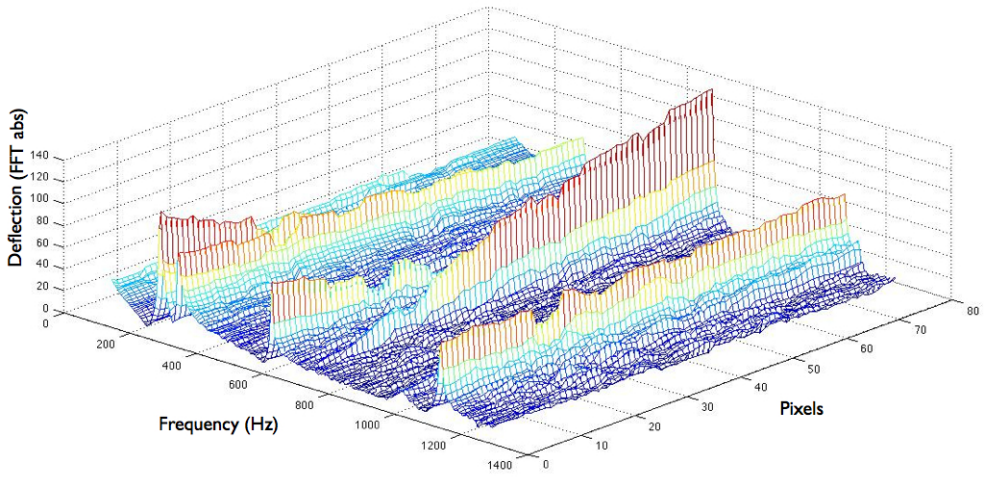

Figure 4.16: Spatial phase stepping waterfall plot of FRF from line 4 of modal testing

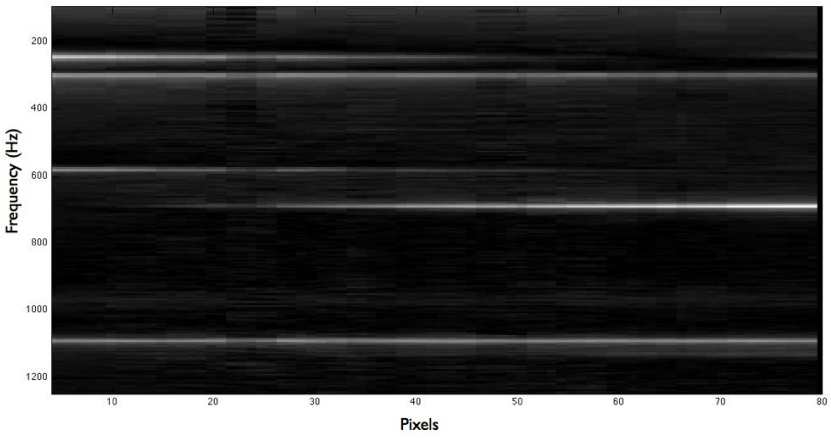

Figure 4.17: Spatial phase stepping aerial view of FRF from line 4 of modal testing

Each measurement point's FRF was processed in ICATS Modent using the circle fit method (Section 2.1.3) to extract the FRF modal parameters and were saved in ICATS Modesh format. ICATS Modesh was then used to correlate the difference between the spatial measurements and the FE model to provide a measure of the natural frequency correlation and the MAC. Figure 4.18 includes the spatial correlation against the FE model (4.18a) and the high correlation results of accelerometer vs FE results seen in Figure 4.18b give confidence to the validity of the FE model. Similarly in Figure 4.19 shows the same diagrams but the comparison of the spatial system vs FE in 4.19a and the temporal vs FE in 4.19b. The natural frequency correlation show comparable results to the accelerometer tests and against the FE results. The results also show slightly better correlation in the MAC when compared to the temporal results (Figure 4.19) where the third mode has been captured more accurately and thus correlates against the FE model.

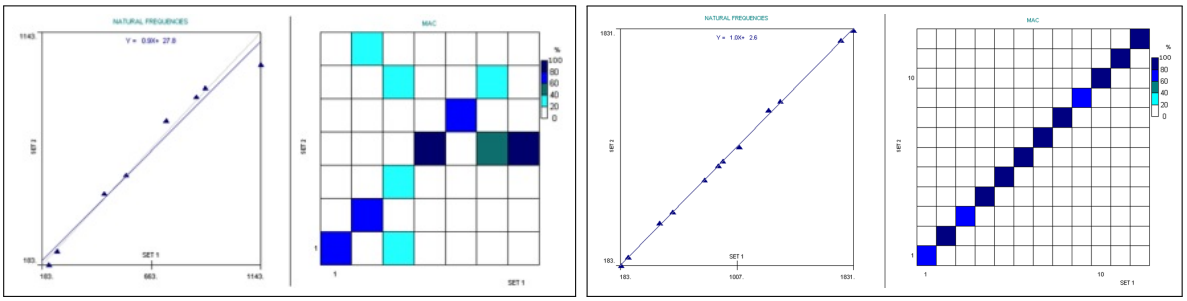

(a) MAC for spatial system *(b) MAC for accelerometer*

Figure 4.18: Comparison of MAC results from Spatial and accelerometer

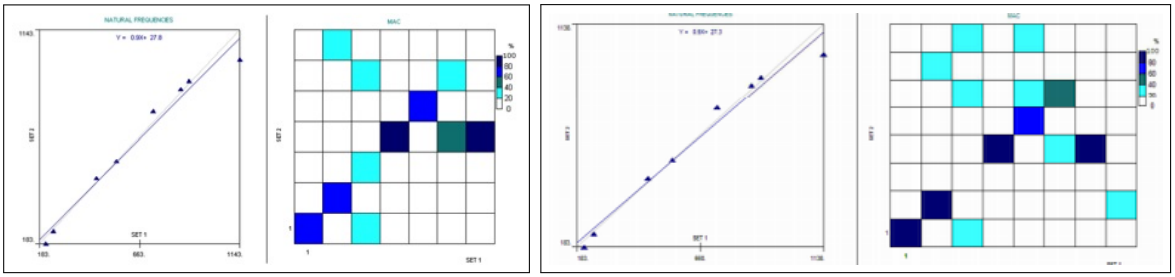

(a) MAC for spatial system *(b) MAC for temporal*

Figure 4.19: Comparison of MAC results from Spatial and temporal

4.5 Discussion

A high speed spatial phase-stepped SPI system was used for the first time to perform quantified modal analysis. The Chapter showed the use of spatial phase-stepping to increase the measurable velocity of an HSSPI system and used a simulation model to understand the system response to multifrequency excitation in preparation for transient testing. The system was then used to perform modal testing on 2 overlapping

plates bolted together and compared it to FE results, accelerometer results and the temporal results from the previous Chapter.

The results showed that the system was capable to perform modal testing. The spatial phase-stepped multipoint system showed its ability to rapidly capture deflection shapes (Figure 4.16) across a range of frequencies from a single impact test.

The frequency correlation results of the spatial data on the left of Figure 4.18a show well correlated results against the FE results and give a similar performance to the accelerometer results in Figure 4.18b and the temporal results in Figure 4.19b. The MAC results for the spatial system in Figure 4.18a show good correlation of the first 6 mode pairs and some improvement over the temporal results from Chapter 3 seen in Figure 4.19b. Where the third mode pair correlating in the spatial results and not at all in the temporal results, however, modes one and two in the spatial result's MAC are less correlated than the temporal result's MAC. When compared to the accelerometer MAC results in 4.18b it was clear that the range and sensitivity of the contact transducer outperforms the spatial system. Firstly from the range that it can capture modal data, demonstrated over 12 resonant frequencies here and secondly from the high correlation values over this range. The FE model can be trusted as the accelerometer data provides high correlation, meaning that the occurrences of correlation off the diagonal from the HSSPI data sets is likely to come from vibration spatial aliasing from the mode shape data. This could be improved if there was hardware modifications of the detector through low-pass and high-pass filters.

Both the temporal system and the spatial systems have demonstrated similar performance and is most likely due to the dynamic ranges of the two systems. The temporal system captured data at a frame rate of 20kHz on an array of 1 x 192 pixels which gave a maximum velocity limit of 1.4 mm/s. This limit was extended with the spatial system at a frame rate of 25kHz with an array of 1 x 656 pixels to 2.77 mm/s. The measurable velocity limit for the temporal system limited the actual range the system could capture. The spatial system tests on the other hand, limited the excitation velocity to a maximum of 2.5 mm/s. This limitation of the velocity was achieved by lowering the force into the system which therefore limited the frequency response range that could be excited. This range was sufficient to capture the first six modes but the signal to noise ratio was too low to extract modal properties of modes higher than this.

With this physical restriction for the measurement of velocity the only way to improve HSSPI performance for modal testing is to increase the dynamic range of the system. The maximum velocity for the spatial system could not be increased as the line length of the array was at a minimum due to the test object being larger than

the field of view. The longer the line length the slower the framerate of the CMOS camera.

4.6 Chapter summary

The system demonstrated the principle of a spatial phase-stepped SPI system for use in modal testing, within the 6 modes of correlation and had a small improvement over the temporal system. The limits of the system were discussed and compared to accelerometer and FE results.

The next Chapter applies the spatial phase stepped SPI system's parallel measurement ability to the measurement of traveling waves on a centre clamped circular disc.

Chapter 5

HSSPI application to measuring traveling waves

A unique application of the HSSPI system is to measure and identify traveling waves. This application is unique to SPI in general as the ability to capture simultaneous parallel measurement points of interest at an instance is essential to measure traveling waves. Simultaneous parallel measurements capture the relative phase between measurement points, so they can be measured and compared directly. It is impossible to do similar tests with single point devices as there is no way to compare the measurement points without performing multiple tests, additional processing and data synchronisation. These tests require intensive post-processing analysis to identify modal complexity factors in the measurement data [3, 138]. Different user experience delivers different determinations of the presence of traveling waves and without this analysis and experience it is impossible to identify traveling waves with single point measurements.

Using the HSSPI system can overcome these issues as it offers the high temporal resolution to capture multi-frequency and transient events but also offer adequate spatial resolution to capture the relative phase difference between the pixels to understand the vibration response of a system. This approach has been successfully demonstrated by researchers studying break squeal [105, 107, 108, 142] to identify the complex modes affecting brake systems and plates [64].

This Chapter demonstrates the unique application of the spatial phase-stepping HSSPI system to identify the presence of traveling waves that can be used to extend other HSSPI research in this area. A theoretical model of traveling waves is presented that shows how to identify traveling waves and to know if the response from HSSPI is a pure traveling wave, a standing wave or a combination of both. The same system used in Chapter 4 was used to capture traveling wave vibrations on a circular plate clamped at its centre. The plate was initially excited with single frequency excitations

to know the typical modeshapes and resonances that would be expected and secondly excited with a frequency modulated (FM) signal. FM was used to excite the divergent complex modes that occur very close to the resonant frequencies of the plate. Exciting these frequencies causes natural traveling waves to occur in structures [135]. The HSSPI system was used to observe, measure and quantify the ratio of traveling waves and standing waves in the test object. A LDV single point system was used to ensure the HSSPI's measurements were within the system's velocity limits.

The results are presented and discussed at the end of the Chapter showing the advantages to this approach as well as particular applications of the measurement technique.

5.1 Background to traveling waves

A theoretical model of propagating waves is presented in this Section to understand the contributions of traveling waves and standing waves and how they can be measured. A traveling wave can be excited from either a force response using multiple excitation points [133] or by exciting the two degenerate modes that coexist near a structures natural resonance [135]. The latter produces a combination of multiple standing waves that have slightly different wavelengths and frequencies, and interfere with each other to produce a traveling wave. These combined modes produce a response profile that has a mixture of standing and traveling wave components present. An approach with multiple excitation points would mean the force can be tuned and optimised to produce a pure traveling wave with no standing wave - this iterative approach to exciting traveling waves is beyond the scope of this thesis.

The multiple waves that combine to form a propagating wave can be assumed to have an angular position (θ for a circular object) for a single frequency, ω. The wave would produce a wavelength λ_K through λ_K=2π/K, where K is the spatial wave number and would produce a response at a particular point in the form [132]:

$$w(\theta, t) = A(K\,\theta)\,cos(\omega\,t) + B(K\,\theta)\,sin(\omega\,t) \tag{5.1}$$

where $A(K\,\theta)$ and $B(K\,\theta)$ are functions that are both position dependent . $A(K\,\theta)$ and $B(K\,\theta)$ can be expanded further to:

$$A(K\,\theta) = A_1\,cos(K\,\theta) + A_2\,sin(K\,\theta) \tag{5.2}$$

and:

$$B(K\,\theta) = B_1\,cos(K\,\theta) + B_2\,sin(K\,\theta) \tag{5.3}$$

where A_1, A_2, B_1 and B_2 are the peak values of the functions. Equations 5.2 and 5.3 represent the spatial wave values. They can be introduced to Equation 5.1 with the application of trigonometric identities to produce:

$$\begin{aligned} w(\theta,t) = \frac{1}{2}\,(&(\,A_1 + B_2\,)\,cos(\omega\,t - K\,\theta)\;+(\,B_1 - A_2\,)\,sin(\omega\,t - K\,\theta) \\ &+(\,A_1 - B_2\,)\,cos(\omega\,t + K\,\theta)\;+(\,B_1 + A_2\,)\,sin(\omega\,t + K\,\theta)\,) \end{aligned} \tag{5.4}$$

This represents a wave propagating and includes both standing wave components and traveling wave components. The terms $(\omega\,t - K\,\theta)$ and $(\omega\,t + K\,\theta)$ determine the positive or negative direction of the traveling wave and can be separated as such:

$$\begin{aligned} w_+ &= \frac{1}{2}\,((\,A_1 + B_2\,)\,cos(\omega\,t - K\,\theta)\;+(\,B_1 - A_2\,)\,sin(\omega\,t - K\,\theta)) \\ w_- &= \frac{1}{2}\,((\,A_1 - B_2\,)\,cos(\omega\,t + K\,\theta)\;+(\,B_1 + A_2\,)\,sin(\omega\,t + K\,\theta)\,) \end{aligned} \tag{5.5}$$

These equations can be used to define the unique properties that a propagating wave has and with this understanding can be used to identify the presence of traveling waves and standing waves in response measurements. The real and imaginary parts of Equation 5.4 can be plotted on the complex plane and produces variations of an ellipse depending on the presence of either standing waves, traveling waves or the combination of both. If there is a pure traveling wave present, traveling in any direction, the ellipse on the complex plane has a constant radius making it a circle. If there is both traveling waves and standing waves present this produces an ellipse and if there is only standing waves present this produces a straight line with no ellipse present. The direction of the traveling wave can be determined from the slope of the spatial wave's phase across the measured array, a traveling wave in the positive direction, w_+, produces a positive gradient and a traveling wave in the negative direction, w_-, produces a negative gradient.

The ratio of the ellipse's major and minor axes give an indication of the amount of traveling wave to standing wave[132]:

$$Standing\,Wave\,Ratio = \frac{|w_+| - |w_-|}{|w_+| + |w_-|} \tag{5.6}$$

where the ratio -1 is a pure traveling wave in the negative direction, 1 is a pure traveling wave in the positive direction and pure standing waves (when positive and

negative equal each other) cause the ratio to tend towards infinity and seen as a standing wave. This ratio can be used as an indication of the presence of traveling waves. In order to quantify the presence of a traveling wave, curve fitting of an ellipse can be applied to the measured spatial response data. The data can be captured with the use of non-contact single point measurements or scanning LDV [132], but only through repeated measurements and synchronisation of the signals and data, which can be labour intensive. However, with the use of multipoint parallel sensors, such as HSSPI, the presence of traveling waves can be identified through their ability to capture the instantaneous relative phase across the detector array. This relative phase can be used to determine the wavelength of a traveling wave, the direction of the traveling wave and the spatial frequency of the wave.

5.2 Simulation work

With the theory presented in Section 5.1 a Matlab model was created to understand how the characteristics of traveling wave vibrations interacted and would be interpreted by the HSSPI spatial system. The simulations also demonstrate the curve fitting applied to a range of array lengths to identify the presence of traveling waves.

The model is treated as an array of ideal measurement device points, spaced exactly beside each other on a single parallel line. For the simulations in this Section the number of these arrays are 60, 100 and 200 pixels in length to demonstrate the accuracy of different ellipse fittings on different array lengths. The sampling frequency and sample length of the simulation data are 20kHz and 5000 blocks of data respectively, based on the test system characteristics that would be used.

The model firstly creates the spatial parameters of the wave as described by Equations 5.2 and 5.3 which combine to form the spatial wave shape that vary with time for the simulation. If these two specific waves combine and are of equal value: a standing wave is produced, if the magnitude of one of the directional waves is larger than the other, but both are non-zero: a combination of standing waves and traveling wave is produced in the direction of the wave with the largest magnitude. If one of the directional waves has a magnitude of zero: this produces a pure traveling wave in the direction of the non-zero wave. The waves are separately varied to produce different amplitudes of the spatial wave shapes and the contributions of a standing wave, traveling wave or a combination of both.

Varying the spatial shape with time at a harmonic frequency can be simulated by using the conditions in Equation 5.4. This response produced a time-resolved vibration data across the array of ideal sensors, creating a time-resolved vibration map. The map was transformed into the frequency domain using the FFT transform, that can then be used to identify the vibrating frequency applied, the phase and the

separate real and imaginary parts of vibration. The real and imaginary parts of the data can be plotted onto the complex plane and the use of ellipse least-means-squares (LMS) curve fitting to the data points on this plane gives the ratio of standing and traveling waves from measured data.

How these separate properties of traveling wave conditions affect each other and how they are observed in terms of an array measurement is presented in the rest of this Section. The different parameters that are changed in the model are the pixel length, spatial wave shape, the traveling wave speed and the frequency of the standing wave. The pixel length was changed to aid the understanding how the length effects the accuracy of the curve fitting on the complex plane and to identify if there was a minimum length for successful curve-fitting, these variables were set to 60, 100 and 200 pixels to demonstrate this. The spatial shape was varied to show that different wave shapes can be measured but have different effects on the complex plane and that basic analysis cannot demonstrate from the wave shape alone if a traveling wave is present. This spatial waveshape was set to $\pi/100$ and $\pi/400$ due to their similarities to the experimental waves at the resonant frequencies. The traveling wave speed is changed to show how the wave is perceived by the array of pixels against time. Finally the frequency of the standing wave is fixed to 242Hz to be representative of the experiments in the following Section.

The changes of the variables above are presented over this Section in different forms to show how the system was used to identify traveling waves. These forms are a temporal map of the pixels against time, an overlay of the first and last pixel in an array against time, a 3D waterfall plot of pixel against frequency and finally the spatial phase of the waveshape in the frequency domain. Each of the plots are described below to show the benefits of each of the plots and their limitations.

The temporal map shows multiple frames of measurements from an array of pixels. Represented in Figure 5.1a where the array of pixels is the x-axis and the frames run down the y-axis. The display of a temporal map provides a way to:

- Visually represent the vibration pattern that was seen by each pixel length against time.
- Visually see the direction of a traveling wave, if present.
- However, this does not give a complete solution to understand the ratio of standing and traveling waves, or provide an understanding of the waveshape when the traveling wave speed is high.

The first and last column plot of the temporal map are overlaid on a single plot, as shown in Figure 5.1d. This plot provides:

- An understanding if the peaks of the waves have a lag can be an indication of a traveling wave being present
- Can show leading and lagging of basic waves in simple waveforms
- However, for more complex waveforms it is difficult to understand if a traveling wave is present based on this.

The spatial wave plot shows the calculated waveshape in the frequency domain, calculated from the temporal map, a 3D waterfall plot can be seen in Figure 5.1c, showing magnitude and pixel length against frequency. This provides and understanding of:

- What the waveshape is regardless the speed of the traveling wave.
- However, it is only the waveshape that can be seen from this plot, no indication of the presence of traveling waves or the direction can be identified from this plot.

The spatial phase plot shows the phase across the pixels at the point of maximum response across the pixel array in the frequency domain. Figure 5.1b shows an example of this, where this figure provides:

- the ability to know the direction of the traveling from the gradient of the phase, if no gradient is present then it is a standing wave.
- However, no understanding of any other properties of the waveshape can be taken from this.

The Complex plane is a plot of the real and imaginary parts, from across the pixel array in the frequency domain, plotted against each other. Seen in Figure 5.8, where the variations of different combinations of waves are seen, and discussed further later in this Section. These plots provide:

- The ratio of standing and traveling waves with an ellipse, the presence of a pure traveling wave, with a circle or a pure standing wave, as a straight line.
- However, there is no understanding of the waveshape.

These plots together can provide a method of identifying traveling waves and standing waves from an array measurement, but none alone can give a complete solution.

The first vibration scenario presented is a standing wave of 241 Hz varying with time, this is shown in Figure 5.1. Where Figure 5.1a shows the temporal map, described above, with the array length on the x-axis and the frames varying with time

on the y-axis. The spatial wavenumber was π / 100 that can be seen to produce a nodal line in the vibration pattern at pixel 75. All the points on the vibration map can be seen to be either fully in phase with each other or fully out of phase either side of the nodal line. The standing wave properties is shown by comparing the first and last column as in Figure 5.1b where the first column of Figure 5.1a is overlaid upon the last column of Figure 5.1a, which shows the time domain waves to be completely out of phase with each other with no lag, as expected from a standing wave. The frequency domain results are shown as the spatial wave plot in Figure 5.1c where the shape of the spatial wave is at input frequency of 241Hz, the phase from this Figure is used to plot its corresponding spatial phase in Figure 5.1d. As expected the standing wave produces a constant phase change with no gradient and is out of phase after the nodal line at pixel 75.

The introduction of a traveling wave to the standing wave of 241 Hz can be seen in Figures 5.2, 5.3 and 5.4, which show the results of the different array lengths of 60, 100 and 200 pixels, respectively. Again each of the array's temporal maps can be seen in Figures 5.2a, 5.3a and 5.4a. The longer the length of the array the more of the waveshape can be seen on the temporal map. The first and last columns of each of the temporal maps were overlaid and can be seen in Figures 5.2b, 5.3b and 5.4b. These Figures shows the the slight variation in phase that the traveling wave introduced by the blue wave leading the red by a few frames. The spatial wave plot is shown in the Figures 5.2c, 5.3c and 5.4c where each of the different pixel lengths shows more of the the spatial waveshape, that demonstrates that the longer the array length the more information that can be captured about the spatial wave shape.

The direction of a traveling wave can be determined from the gradient of the slope in the phase plots, demonstrated in Figure 5.5. Where each column in Figure 5.5 represents a pure traveling wave, moving in opposite directions, the top row shows the traveling wave represented in the temporal maps. It can be seen that both have different directions from the diagonal lines through time, these lines are lines of constant phase. Figures 5.5c and 5.5d shows the overlay of the first and last column and by comparing both the images it can be seen that in Figure 5.5c the blue waveform lags the red waveform and in 5.5d the blue waveform leads the red waveform, this shows the different directions each column is traveling. In the frequency domain the spatial phase produces Figure 5.5e and 5.5f where the direction of the traveling wave can be taken from the gradient of the phase's slope. If the gradient is positive, as in Figure 5.5f, the traveling wave is moving to the left with respect to the array and if the gradient is negative, as in Figure 5.5e, the traveling wave is moving to the right with respect to the array.

When the velocity of the traveling wave is high, it becomes impossible to understand the waveshape from the temporal map alone, as the traveling wave present in the array measurements is too dominant. This is demonstrated in Figures 5.6 and 5.7, where two different traveling waves, with their corresponding temporal maps and their resulting waveshapes of different array lengths. The effects that the wave number, K, has on the vibration signal can be seen by comparing Figure 5.6 and 5.7 showing the difference between $K = \pi$ / 100 and π / 400. The column on the right of these figures shows the variation of spatial wave shape measured from different pixel lengths. Figures 5.6 and 5.7 show that different array lengths can capture more of the frequency domain waveshape from the temporal maps, this helps understand the quality of information that can be fitted on the complex plane.

Plotting the real and imaginary parts of the frequency domain array data on the complex plane provides a further understanding of the presence of traveling waves. An LMS ellipse fit was applied to the simulated measurement points and shows that different vibration conditions produce different variations of an ellipse, seen in Figure 5.8. The first column in Figure 5.8 represents the vibrations conditions of a standing wave only, the second column represents a mixture of traveling and standing, and the third column shows a pure traveling wave. Each of the rows represent different pixel lengths to show the effects of the fit for different pixel lengths. It can be seen from each of the images that each of the different vibration conditions give a unique shape: if the wave under analysis is a standing wave, there is no ellipse to be fitted and produces a straight line as seen in the first column. If the wave is a pure traveling wave then the ellipse has a constant radius and produces a circle. If there is a mixture of traveling and standing waves then this produces an ellipse, the thinner the ellipse the more dominant the standing wave, and the wider the ellipse the more dominant the traveling wave is.

The simulation work has illustrated the different types of analysis that can be used to identify traveling waves and provided confidence in the curve fitting techniques used in the next Section for the identification of traveling waves in the experimental data.

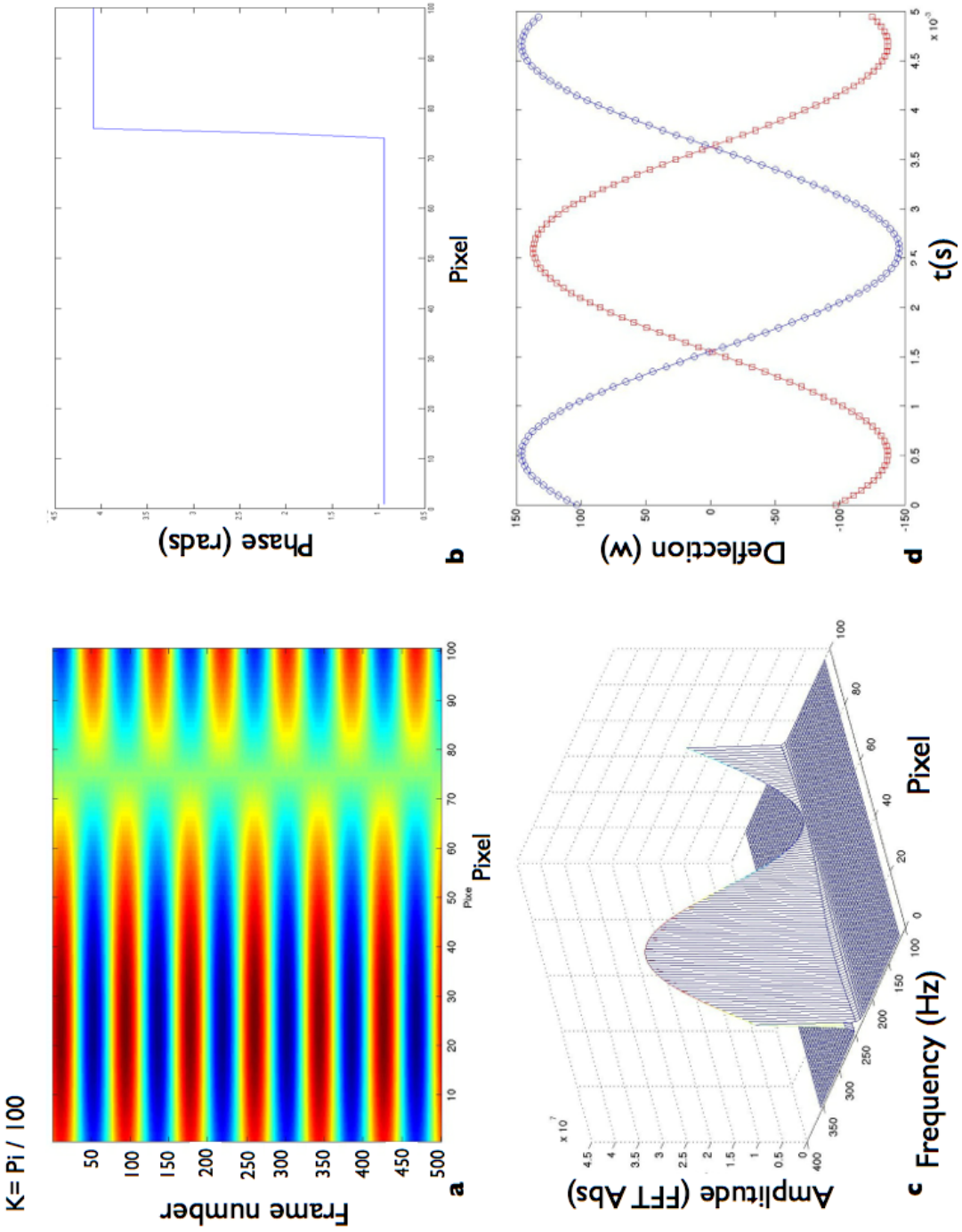

Figure 5.1: Outputs from simulated model for a 241Hz standing wave with wavenumber K = π / 100. With a) showing spatial response data across 100 pixels and 500 frames, b) calculated spatial phase from FFT at 241Hz, c) Spatial FFT amplitude vs frequency and d) the overlay of the first and last column of (a)

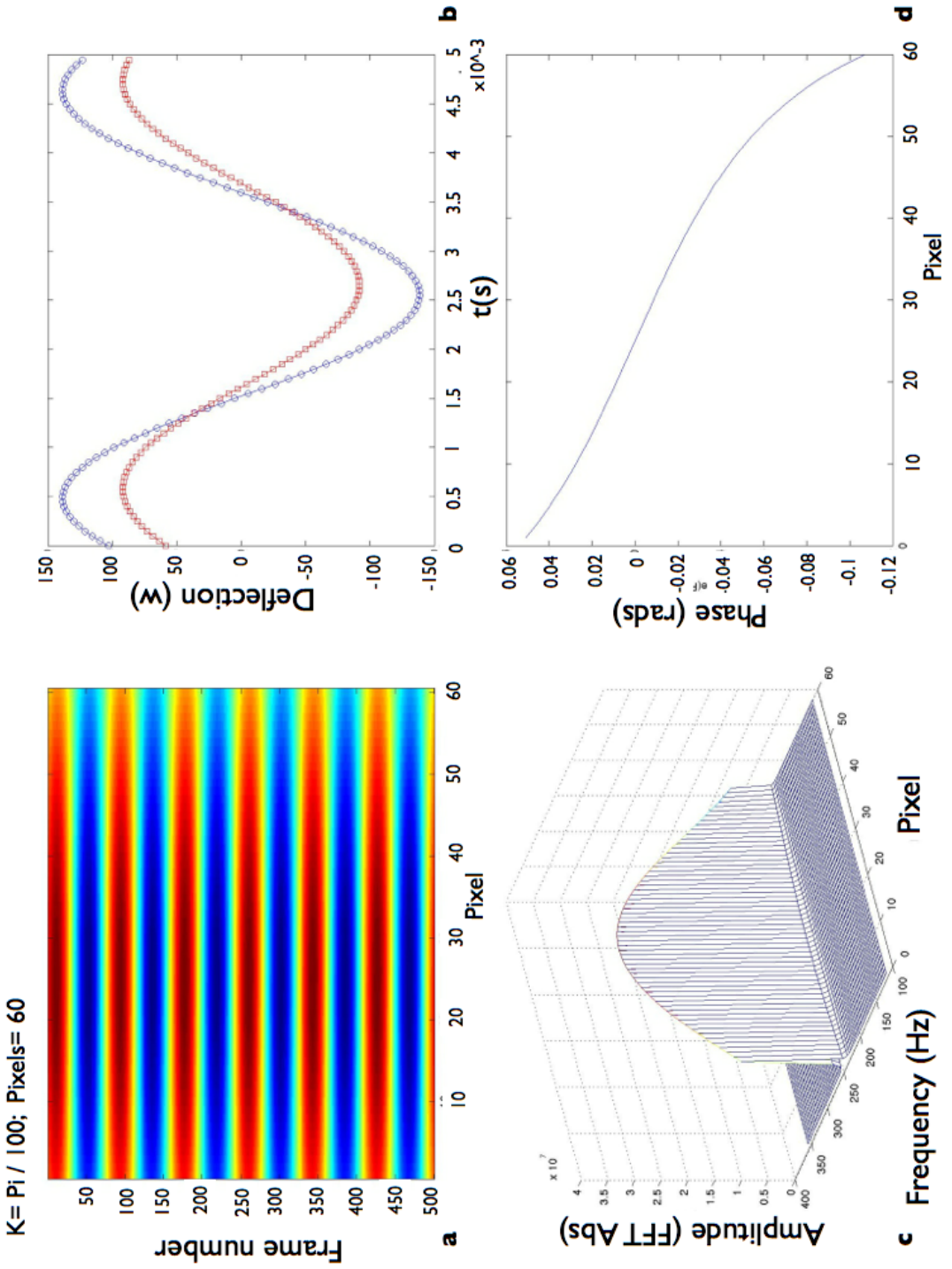

Figure 5.2: Outputs from simulated model for a 241Hz standing wave and a traveling wave with wavenumber K=π / 100. With a) showing spatial response data across 60 pixels and 500 frames, b) calculated spatial phase from FFT at 241Hz, c) Spatial FFT amplitude vs frequency and d) the overlay of the first and last column of (a)

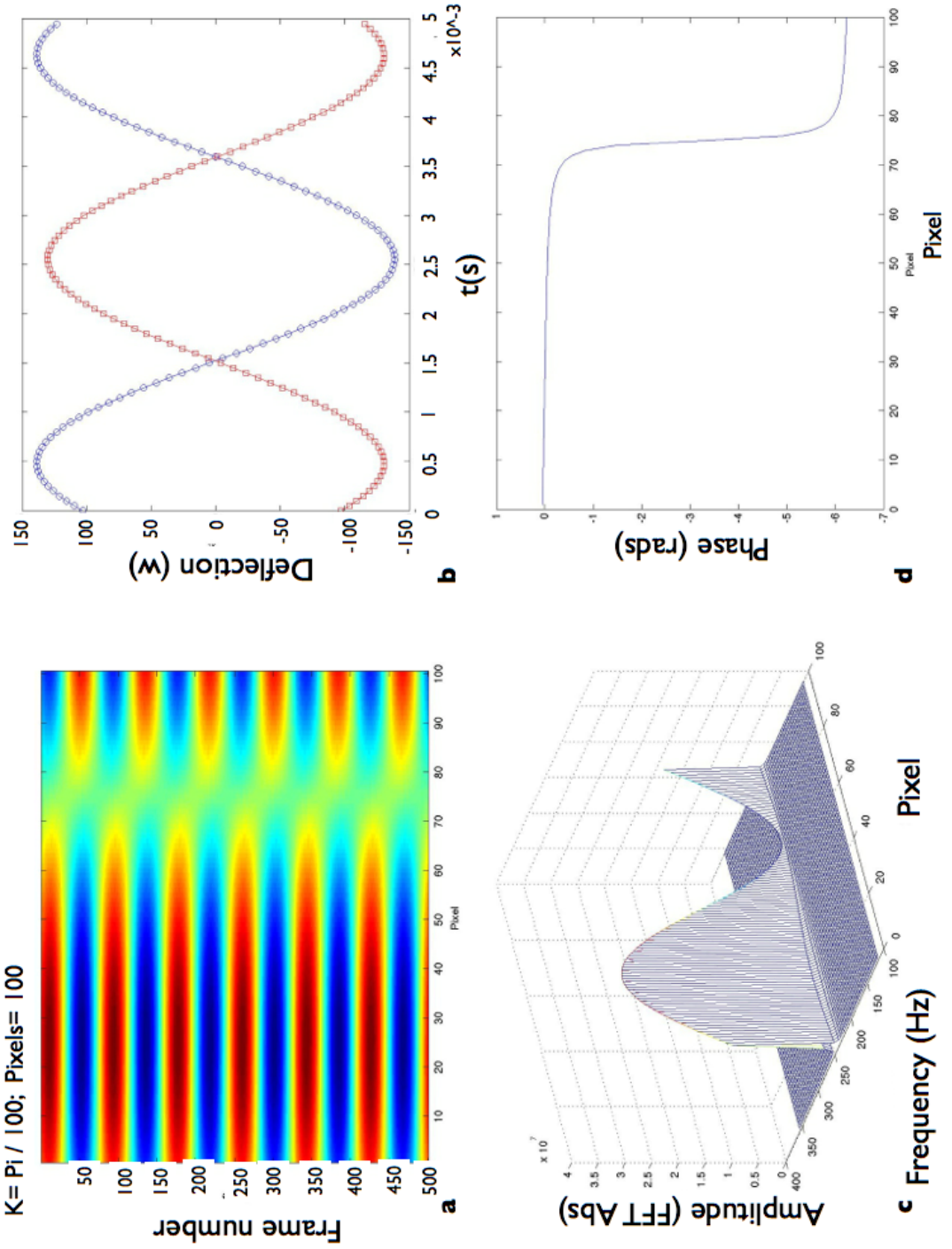

Figure 5.3: Outputs from simulated model for a 241Hz standing wave with a standing wave K=π / 100. With a) showing spatial response data across 100 pixels and 500 frames, b) calculated spatial phase from FFT at 241Hz, c) Spatial FFT amplitude vs frequency and d) the overlay of the first and last column of (a)

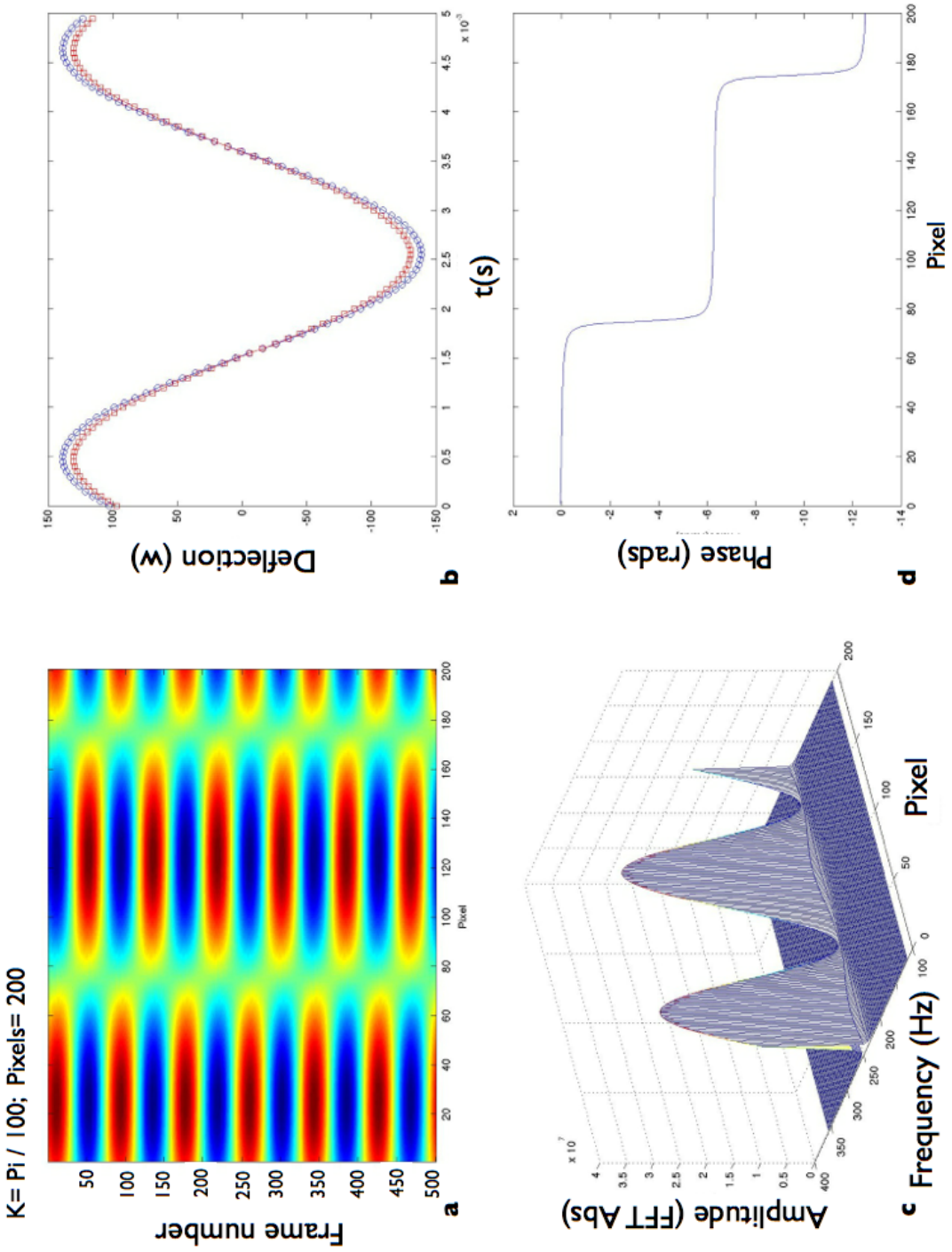

Figure 5.4: Outputs from simulated model for a 241Hz standing wave and a traveling wave with wavenumber K=π / 100. With a) showing spatial response data across 200 pixels and 500 frames, b) calculated spatial phase from FFT at 241Hz, c) Spatial FFT amplitude vs frequency and d) the overlay of the first and last column of (a)

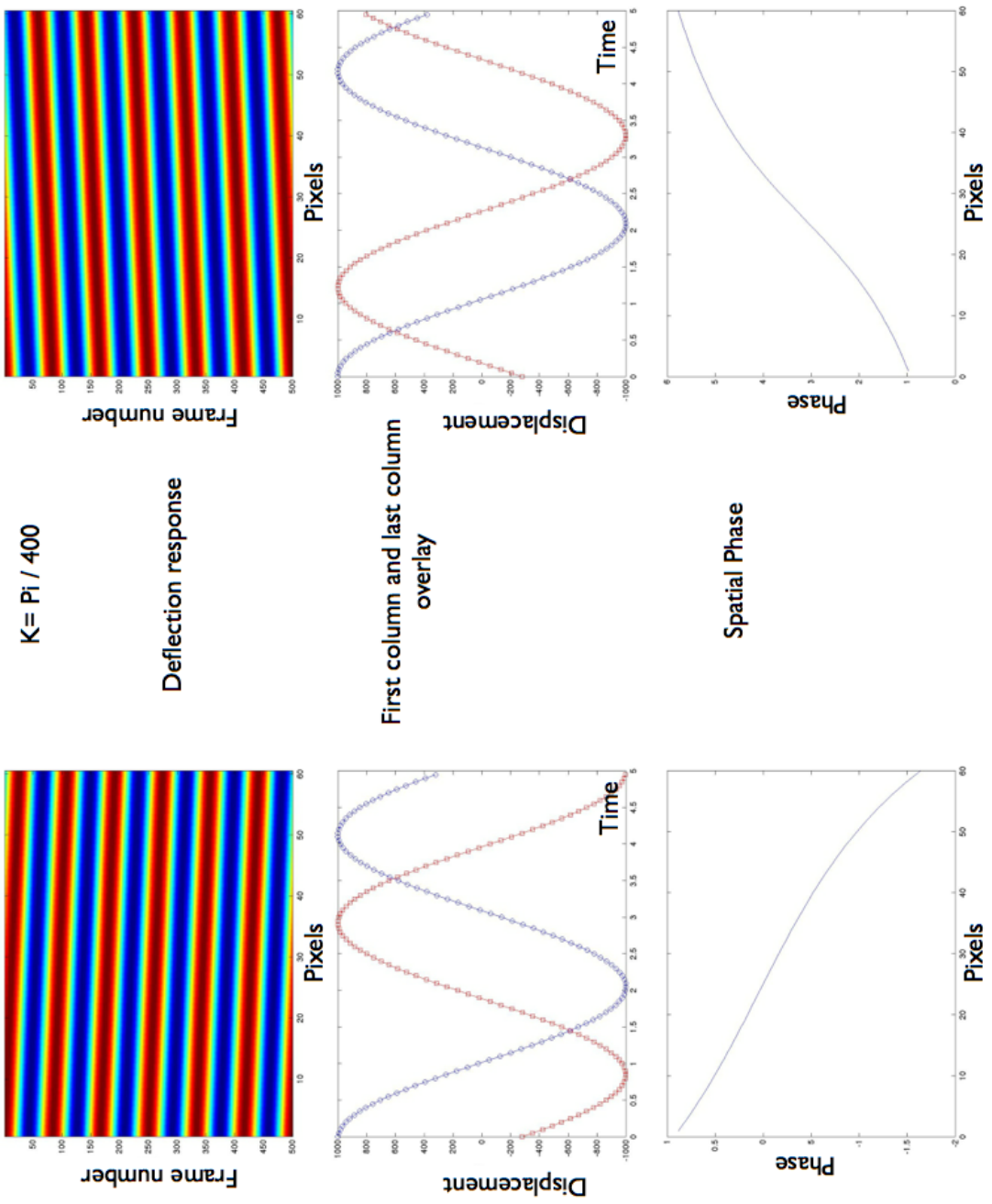

Figure 5.5: Outputs from simulated model to demonstrate the ability to measure the directional of a traveling wave. Top image's are the deflection response, middle images an overlay of the first and last column, and the bottom images are the corresponding spatial phase that demonstrate the direction of a traveling wave. Positive slope means moving to the left of the image. A negative slope means traveling to the right of the image

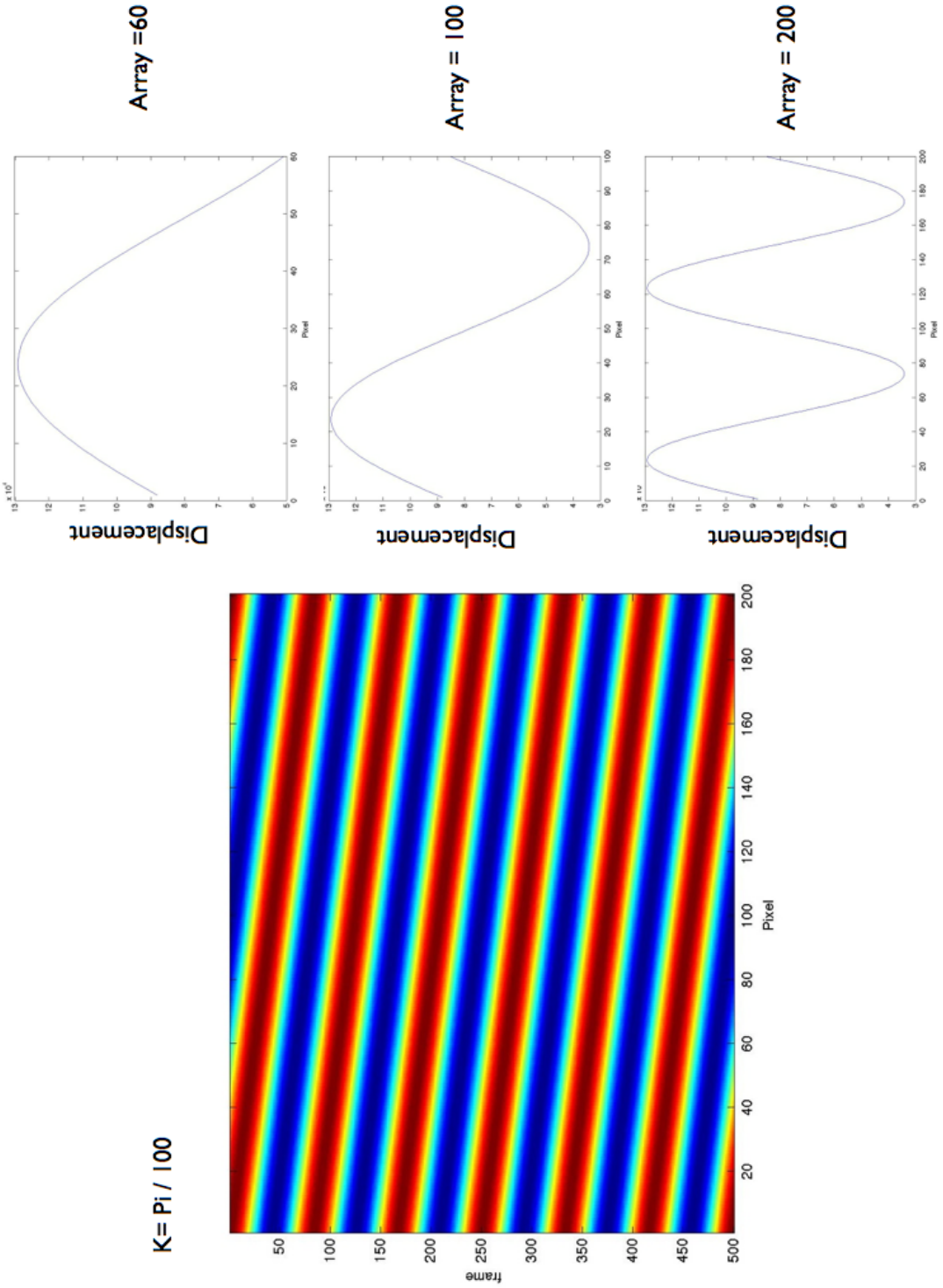

Figure 5.6: Outputs from simulated model for a 241Hz traveling wave with wavenumber K=π / 100. Demonstrating the Spatial wave shapes observed from the different pixels lengths: 60, 100 and 200 and the effects of the wave number K

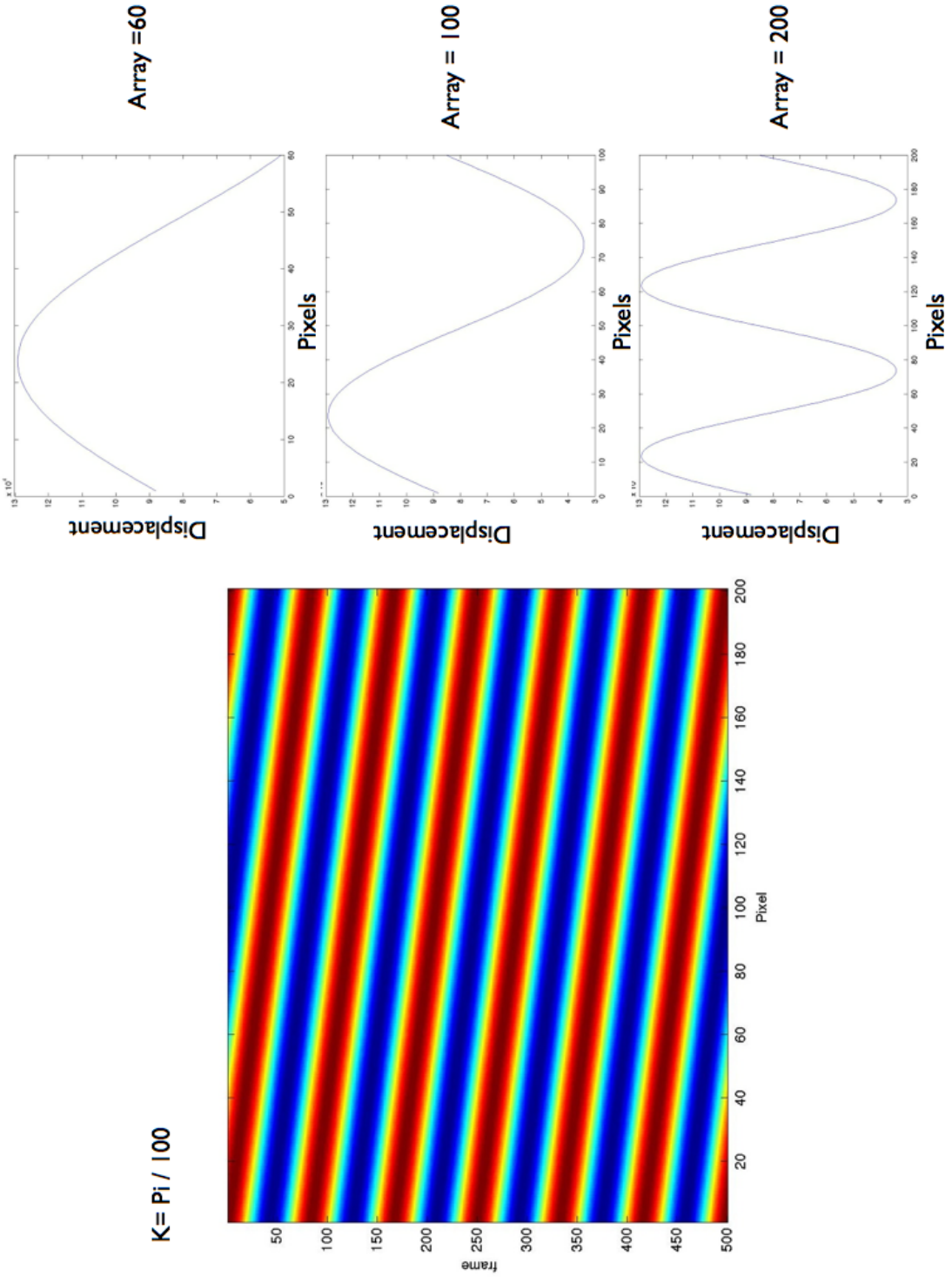

Figure 5.7: Outputs from simulated model for a 241Hz traveling wave with wavenumber K=π / 400. Demonstrating the Spatial wave shapes observed from the different pixels lengths: 60, 100 and 200 and the effects of the wave number K

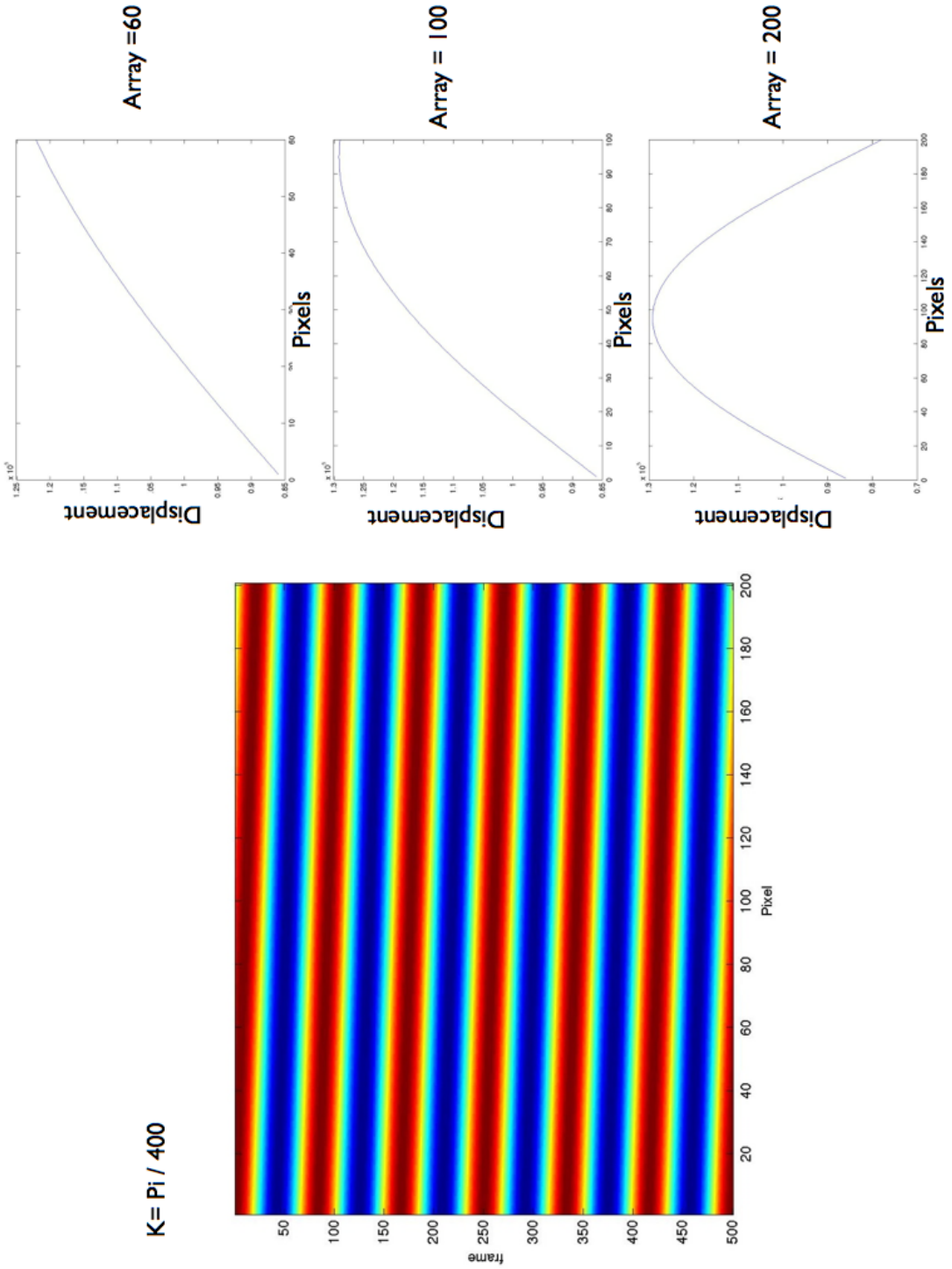

Figure 5.8: Outputs from LMS ellipse fitting to the complex plane of the real and imaginary parts of the vibration. The columns represent the different situations of: standing wave only, standing and traveling waves mixed and traveling waves only. The rows represent increasing pixel lengths

5.3 Experimental system for experiments

The HSSPI spatial phase-stepped measurement systems used for these experiments was the same as described in Section 4.1. The test object for the experiment was a 1 mm thick circular aluminium disc with a diameter of 14 cm and was clamped at its centre. A symmetrical disc was chosen as the diametrical modes make it easier to excite the degenerate modes that produce traveling waves [148]. A traveling wave can be produced by the excitation of the degenerate modes that are likely to exist when the cosine and sine parts of the degenerate modes are within 1Hz of the natural frequency and has relatively low damping [49, 135]. The test object was excited using a shaker (B&K Type 4810) attached to the disc using a stinger and bolts through a 2 mm hole in the plate. The force was measured using a force transducer (B&K Type 8203) attached to the stinger and the plate.

Two excitation methods were used to excite the plates. These were single frequency excitation and frequency modulation (FM) excitation. Single frequency was used to identify the plate frequencies and have standing wave vibration data to directly compare the traveling wave tests data to. The FM excitation was used to excite the degenerate modes in the plate, by the base frequency being used to excite the plate's natural frequency and the carrier frequency to a slightly different frequency to excite the degenerate mode and therefore induce a traveling wave. An Agilent 33210A signal generator was used to produce the signals. Both excitation methods used stepped frequencies to capture each measurement set, steps were set at an increment of 0.5Hz at ±10Hz of each resonant frequency. The carrier frequency for the FM signals was 241Hz (based on the resonant frequency likely to produce a traveling wave known from the initial single frequency tests). A single point LDV system was used to validate the results and to ensure the system was within the systems velocity limits. All the results were processed in Matlab.

Paramater	Value
Camera frame rate	20 kHz
Line length	1 x 656
Max Velocity	2.77 mm/s

Table 5.1: Summary of HSSPI parameters for modal testing in Section 5.3

5.4 Results

5.4.1 Single frequency excitation

Results from single frequency excitation are presented in the following Section. Figure 5.9 shows the raw intensity signal and corresponding phase which was used to calculate the velocity of the SPI spatial phase-stepped system shown in Figure 5.11. Applying

an FFT to the velocity data to transform the data into the complex form can be seen in Figure 5.12 to 5.13.

For validation of the frequencies in the test a comparison of the LDV and Spatial-phase stepped HSSPI can be seen in Figure 5.15, that show the abs FFT vs frequency results of both devices. These results are used to determine the location of the resonant frequencies of the plate, to identify the frequencies and spatial wave shapes.

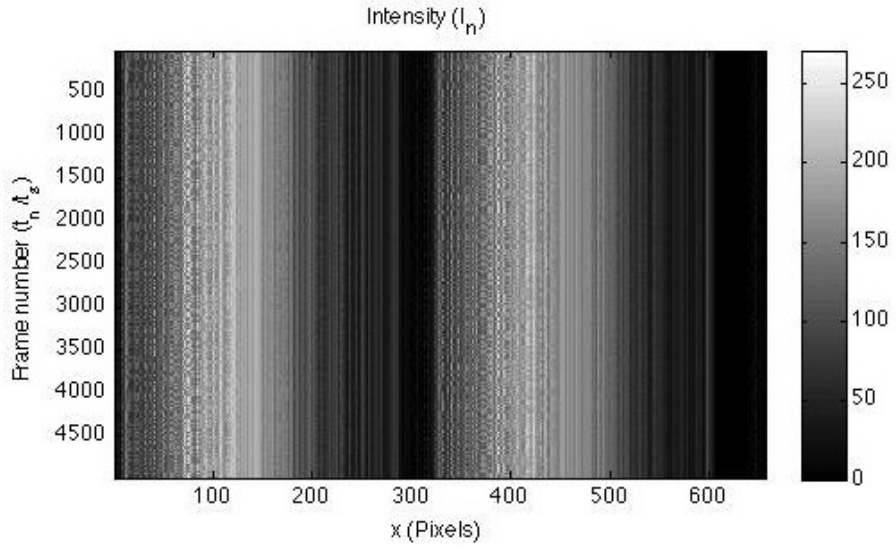

Figure 5.9: Intensity map from 242Hz from spatial HSSPI system

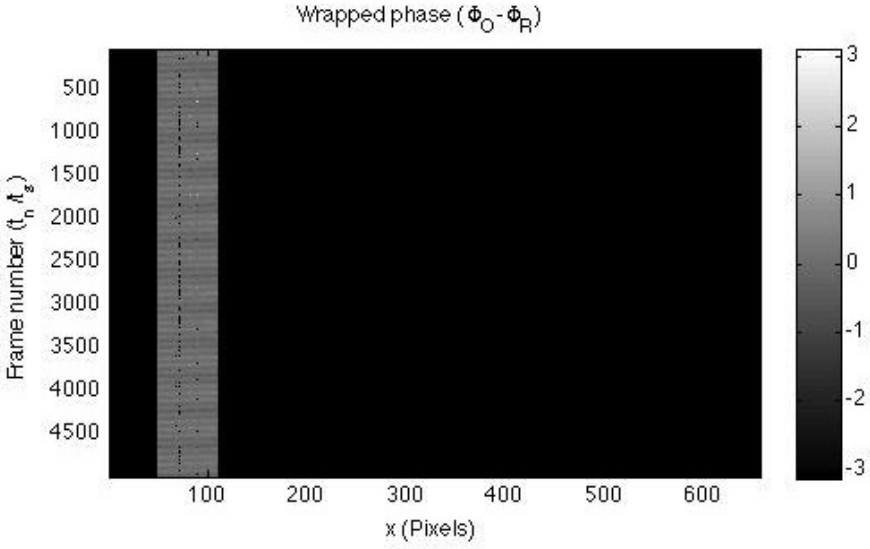

Figure 5.10: Phase map from 242Hz from spatial HSSPI system

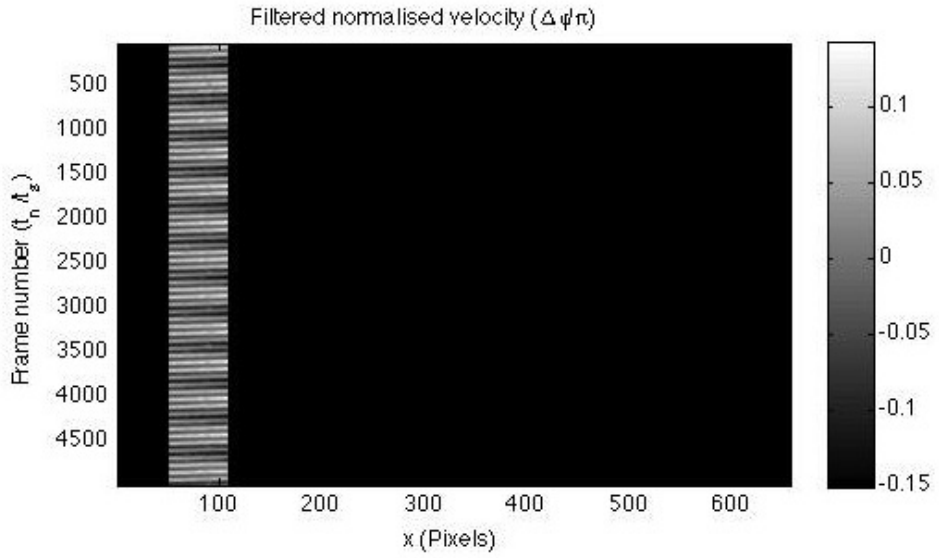

Figure 5.11: Normalised velocity for a 242 Hz single frequency excitation

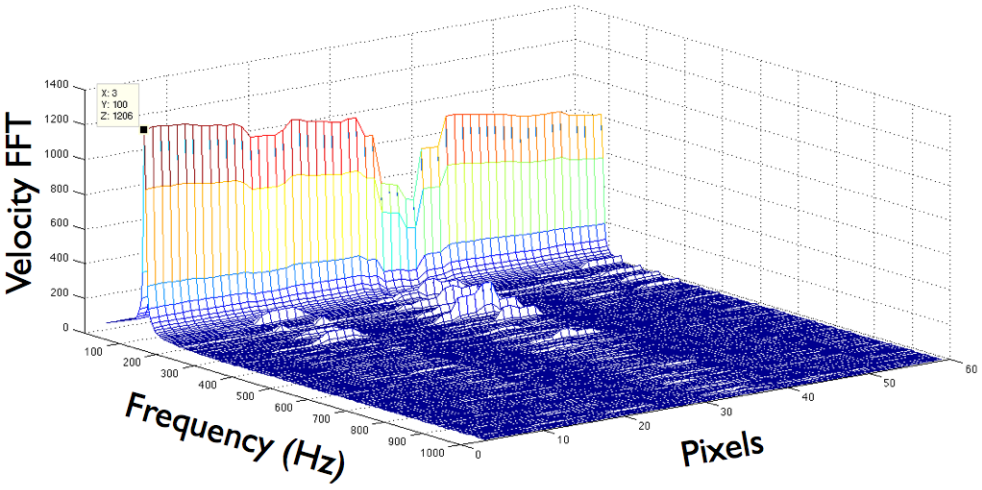

Figure 5.12: Single frequency waterfall plot from spatial HSSPI system of 100 Hz excitation

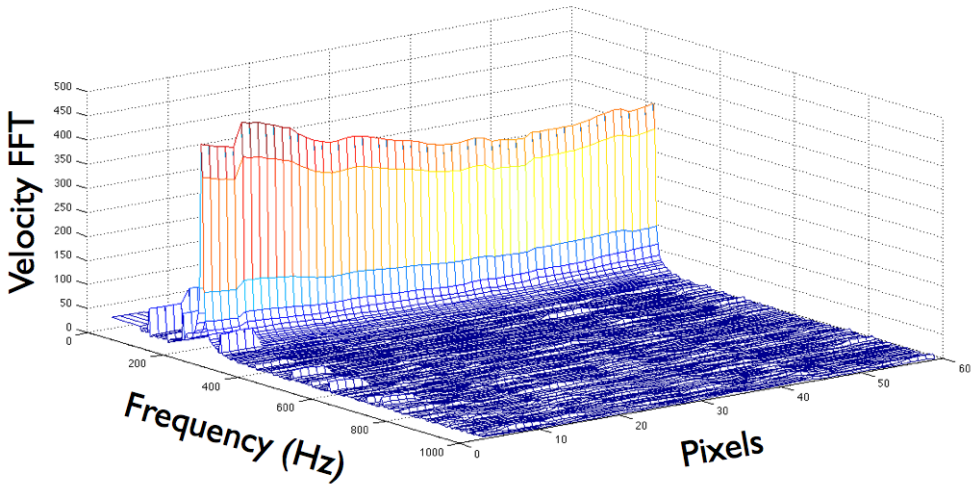

Figure 5.13: Single frequency waterfall plot from spatial HSSPI system of 242 Hz excitation

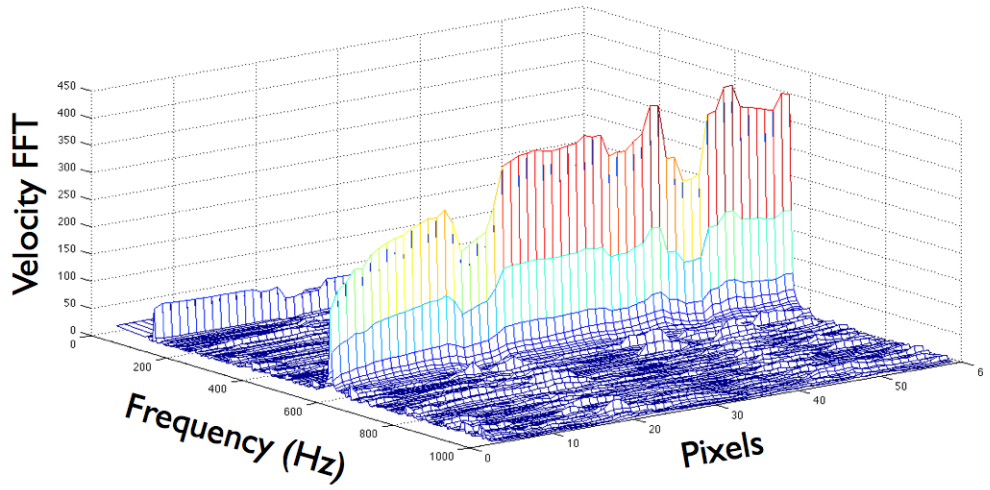

Figure 5.14: Single frequency waterfall plot from spatial HSSPI system of 565 Hz excitation

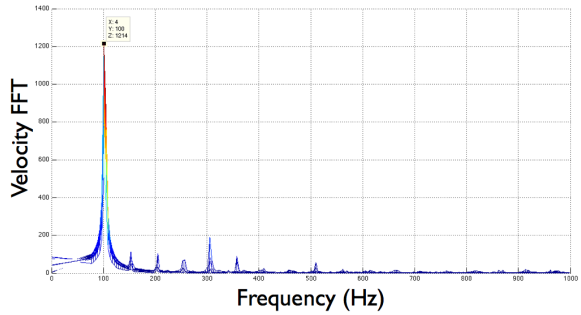

(a) 101Hz: Spatial SPI FFT sideview

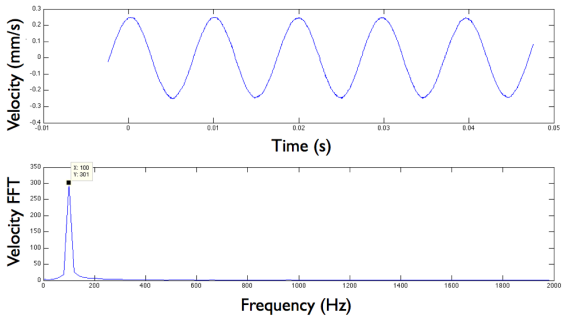

(b) 101Hz: LDV velocity and FFT

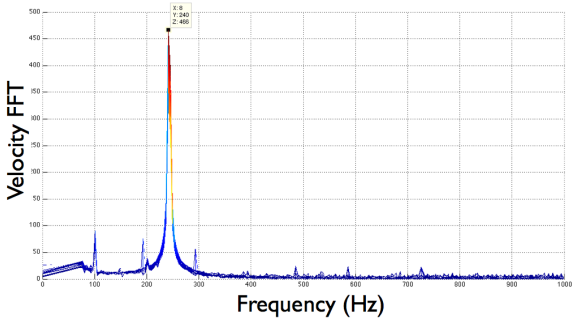

(c) 242Hz: Spatial SPI FFT sideview

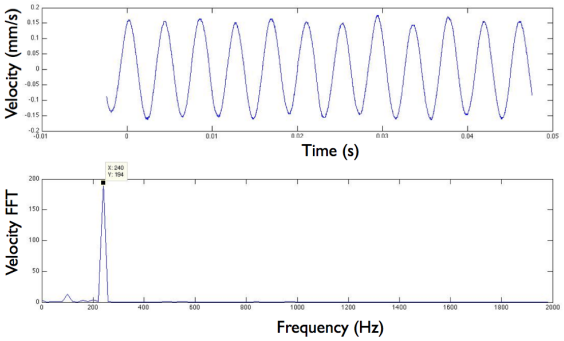

(d) 242Hz: LDV velocity and FFT

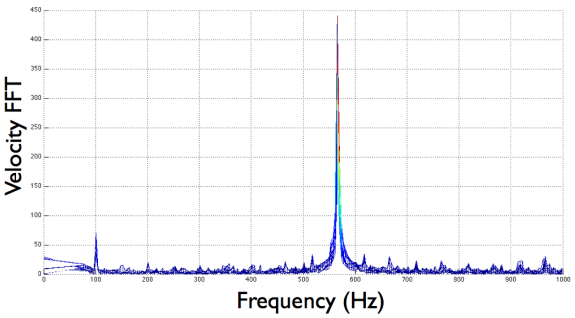

(e) 565Hz: Spatial SPI FFT sideview

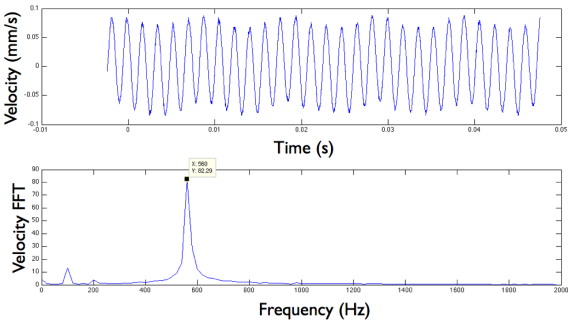

(f) 565Hz: LDV velocity and FFT

Figure 5.15: Comparison of the LDV and SPI spatial phase-stepped system responses from single frequency excitation

5.4.2 Frequency modulation excitation

The FM signal excitation of the plate was a 0.5 Hz stepped-frequency between ±10 Hz of each of the frequencies: 101 Hz and 241 Hz. Two carrier frequencies were used to excite a traveling wave at each frequency, these were 100 Hz and 241 Hz. The results presented in this Section show the results of ±10 Hz of the 242 Hz resonant frequency with the carrier frequency of 241Hz.

Figure 5.16 and 5.17 show the raw intensity data captured by the spatial phase-stepped HSSPI system and the corresponding calculated phase from the the intensity map. This was then used to calculate the velocity in Figure 5.18.

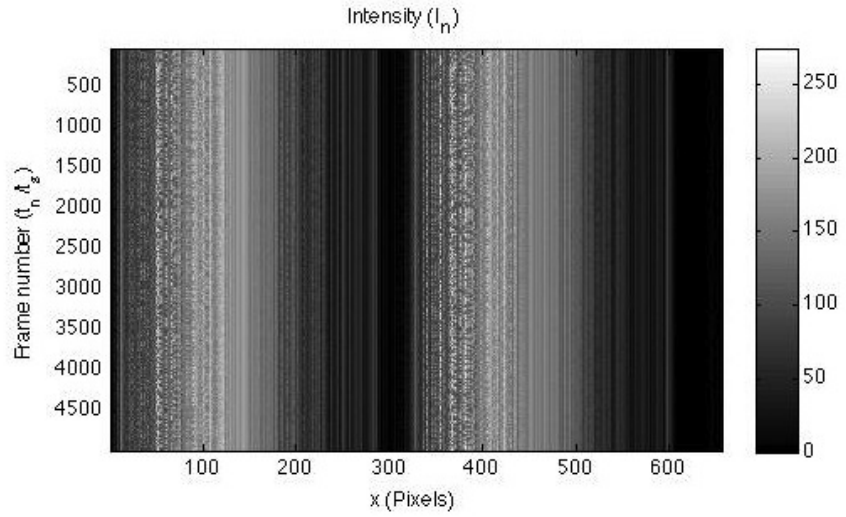

Figure 5.16: Intensity map from 242Hz with 241Hz carrier; spatial HSSPI system

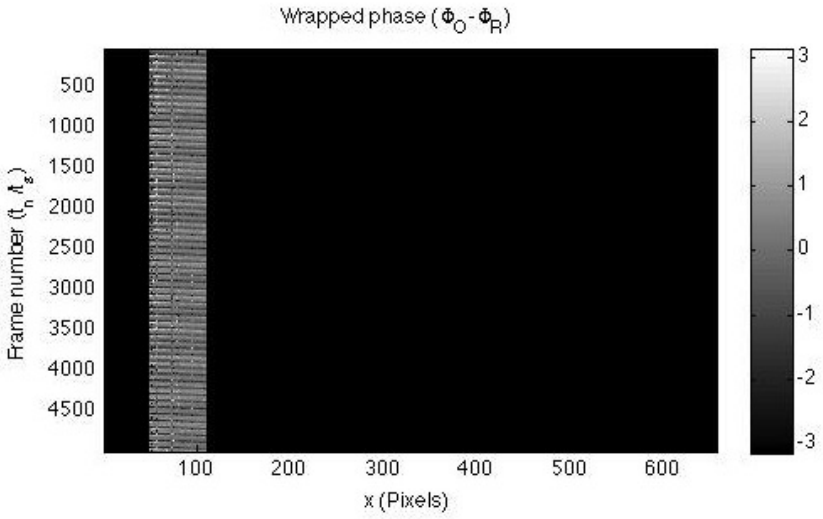

Figure 5.17: Phase map from 242Hz with 241Hz carrier; spatial HSSPI system

Applying an FFT to the velocity data provides the frequency response data. Figure 5.19 shows the absolute values of the FFT data plotted against the frequency. Showing

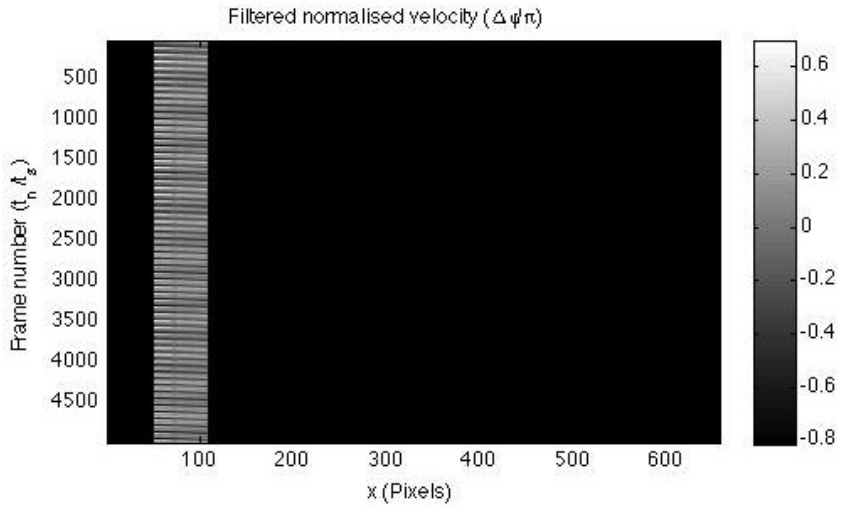

Figure 5.18: Velocity map from 242Hz with 241.5Hz carrier; spatial HSSPI system

two peaks in the frequency response: the first peak at the resonance 242Hz and the expected sideband peak of 484Hz. Only one side band is visible as the carrier frequency and the modulated signal are only 0.5 Hz different. Meaning the lower sideband cancels out: this is shown in Appendix C.

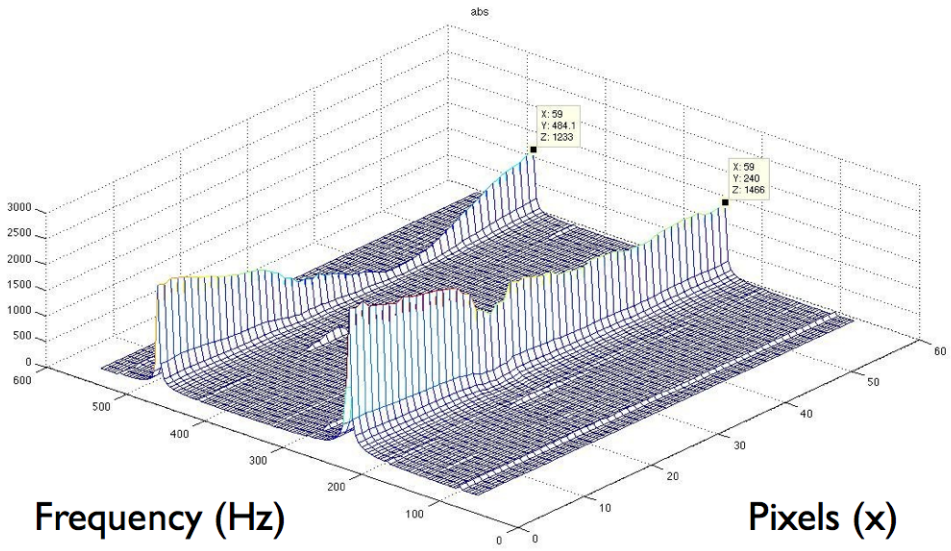

Figure 5.19: Waterfall plot of data at 242 Hz with 241 Hz carrier; spatial HSSPI system.

The frequency response data was used to plot the spatial-phase data against frequency from the multipoint HSSPI, seen in Figure 5.20, where the range of frequencies shows both the resonant frequency (242Hz) and the modulated signal (484Hz). The

phase change of π in the frequency domain is the associated with the poles of a frequency peak. The positive gradient can be seen in the spatial-phase at 242Hz, where we would expect to see a traveling wave, this shows a positive gradient going from left of the image to the right on the pixels axis.

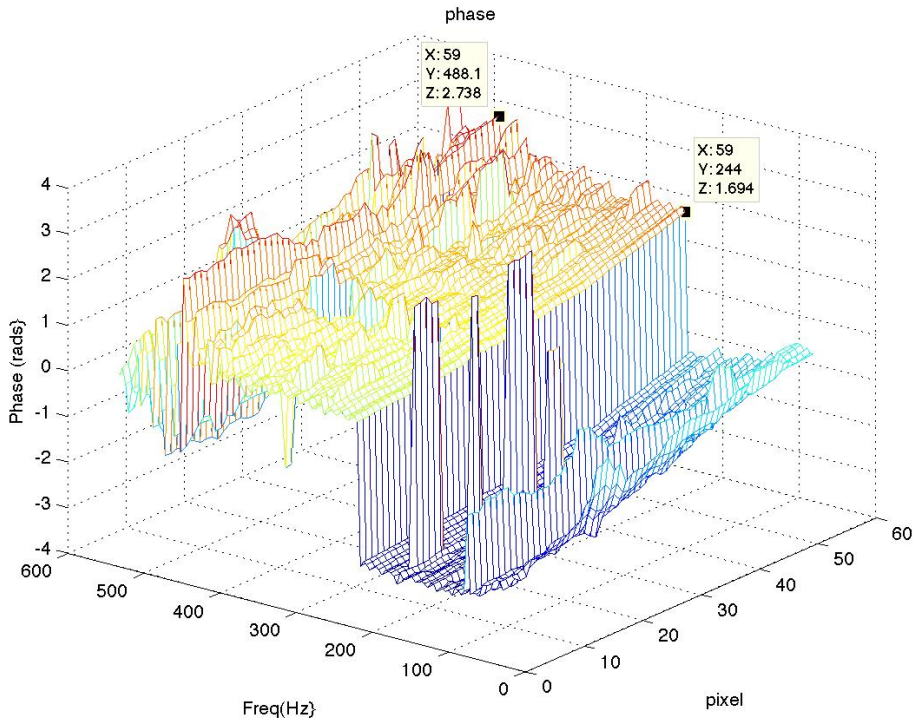

Figure 5.20: Waterfall plot of Spatial-Phase of SPI signal against Frequency

A comparison between the HSSPI and single point LDV frequency response can be seen in Figure 5.21, Where Figure 5.21a shows a side view of Figure 5.19 and Figure 5.21b shows the time series of the LDV above and the frequency response below.

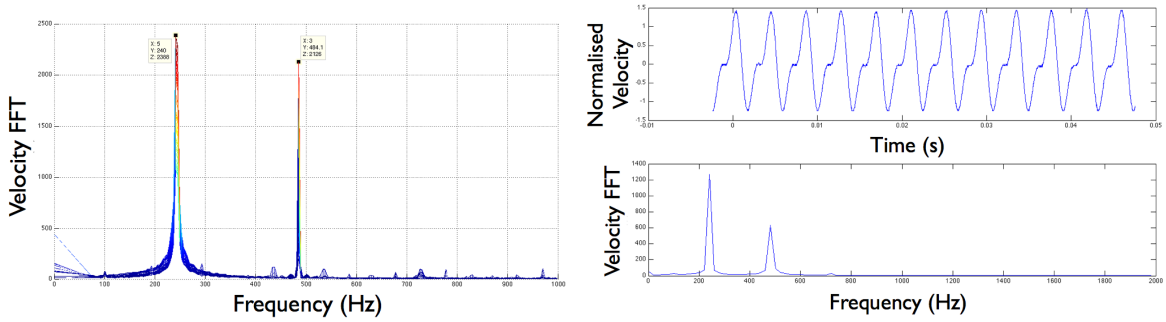

(a) FFT of Spatial SPI sideview *(b) LDV Velocity and FFT*

Figure 5.21: Frequency response comparison between SPI and LDV of 242 Hz with 241.5 Hz Carrier

Comparing the results to the form seen in the simulation work in Section 5.2 to Figure 5.22 we can see a zoomed plot of the time-resolved HSSPI array data from 241.5 Hz with 241Hz FM excitation and an overlay of the first and last column of this

data. The frequency domain of this data can be seen in Figure 5.23 where (a) shows the spatial waveshape against frequency, (b) and (c) show this spatial waveshape and spatial phase against pixel width. Plotting the real and imaginary parts on the complex plane and fitting an LMS ellipse to this data can be seen in Figure 5.23d. A zoomed region of this fit can be seen in 5.23e to show the fit. Both Figures 5.22 and 5.23 show there is a presence of a traveling wave from the positive gradient of the phase and the ellipse in the fitted data and likely to be a mixture of traveling and standing waves.

Figure 5.24 and 5.25 shows the same comparison for response measurements from 234 Hz with a 241 Hz FM excitation where there is no traveling wave present and can be seen by no gradient in the phase data and the straight line in ellipse-fit.

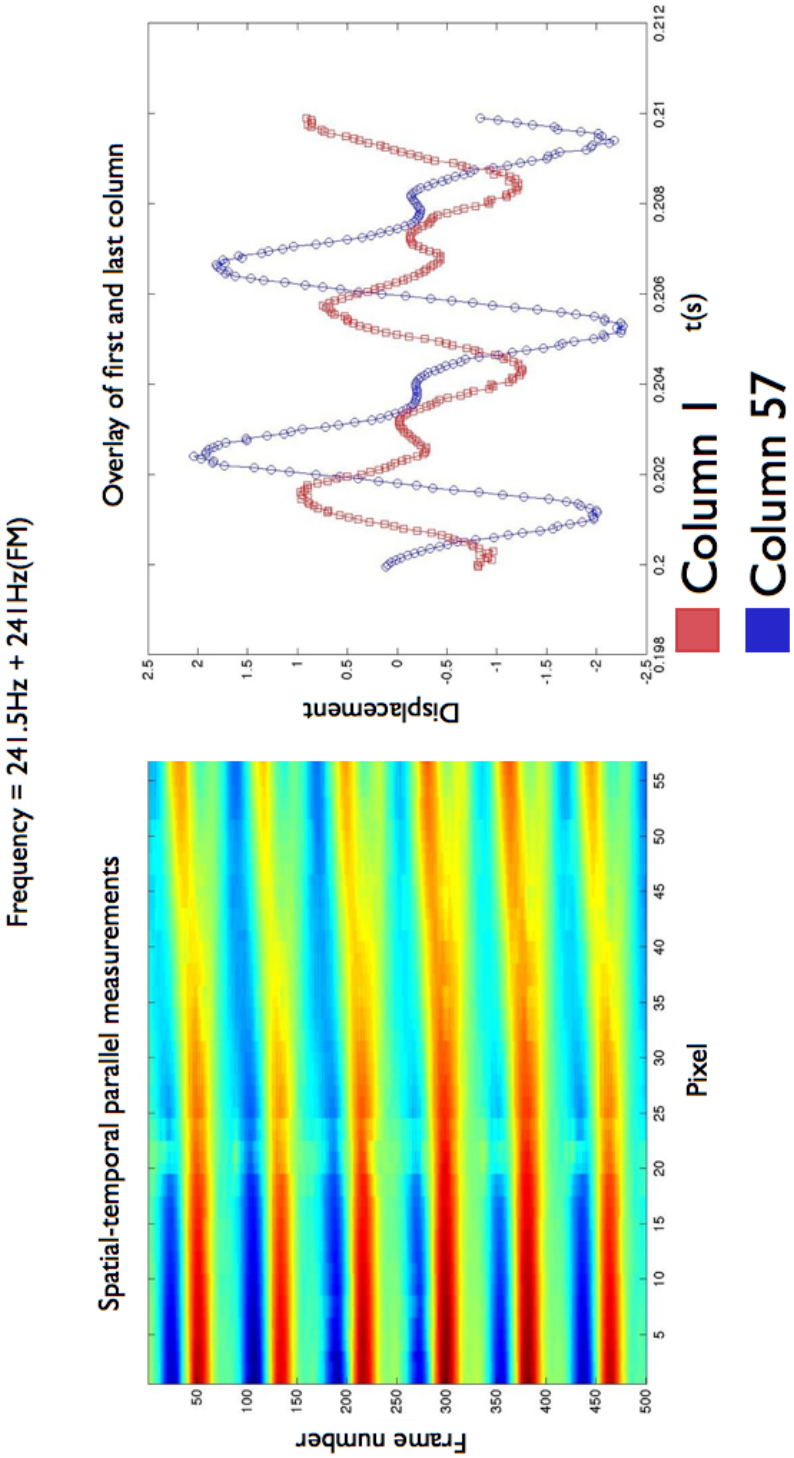

Figure 5.22: HSSPI showing time-array data and the overlay of the first and last column of 241.5 Hz and 241 Hz FM excitation signal

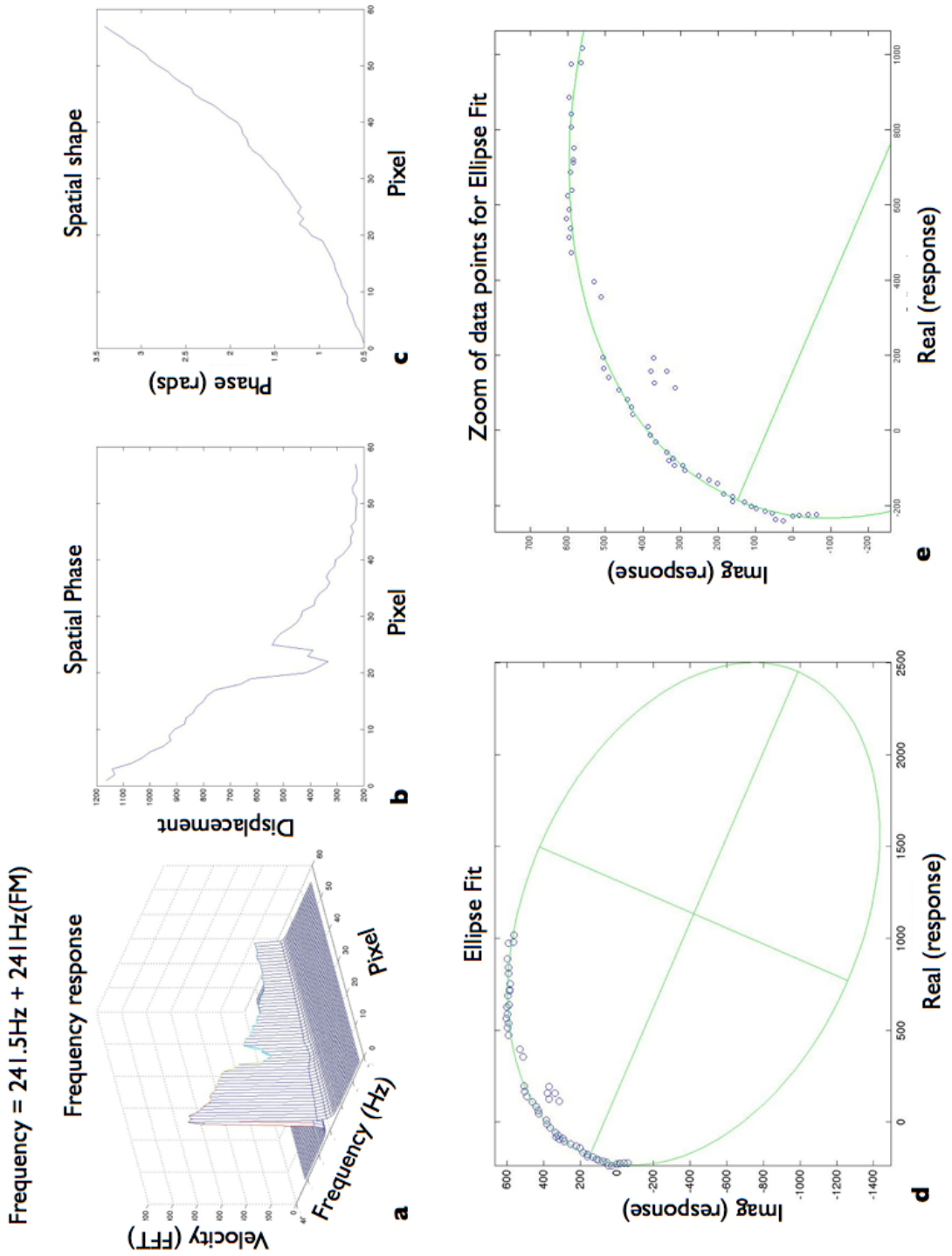

Figure 5.23: SPI HSSPI phase step results for excitation of 241.5 Hz with a 241Hz FM showing a) the abs. frequency domain of the velocity data across the array, b) a 2D plot of the associated spatial phase across the pixel array, c) 2D plot of the spatial shape across the pixel array, d) the whole data ellipse plot of the real and imaginary data and e) a zoom of the data plot for clarity of the fit.

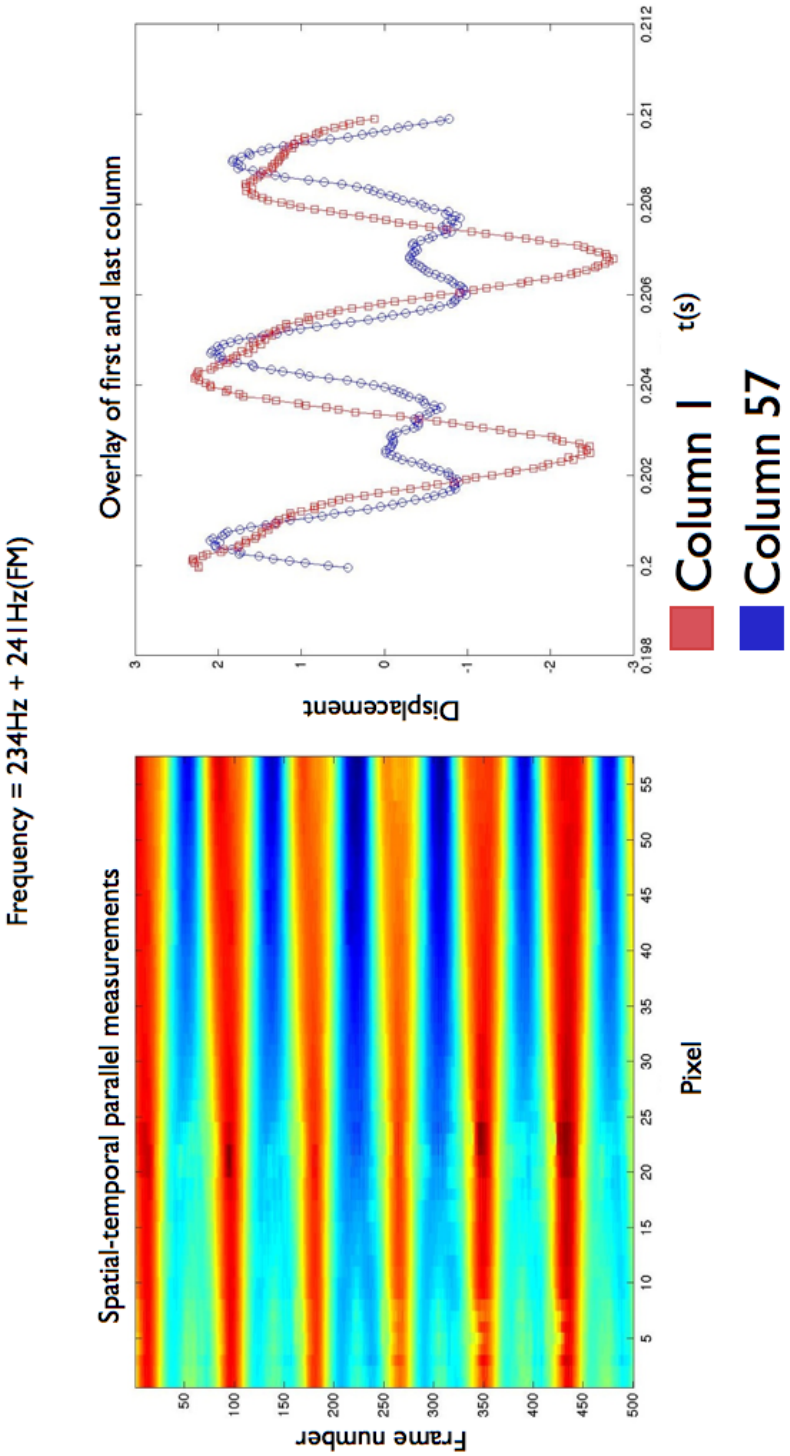

Figure 5.24: HSSPI showing time-array data and the overlay of the first and last column of 234 Hz and 241 Hz FM excitation signal

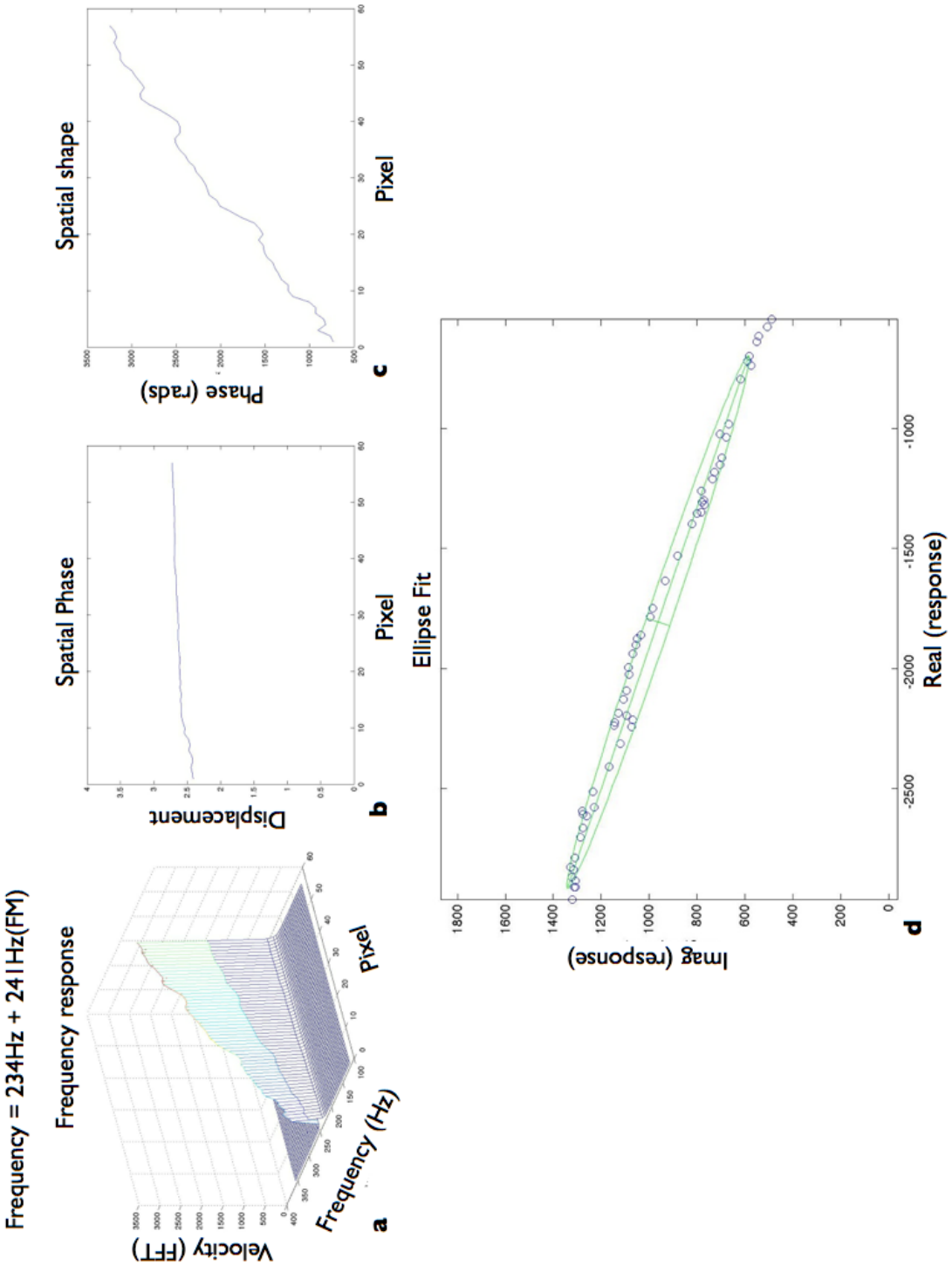

Figure 5.25: SPI HSSPI phase step results for excitation 234 Hz with a 241 Hz FM showing a) the abs. frequency domain of the velocity data across the array, b) a 2D plot of the associated spatial phase across the pixel array, c) 2D plot of the spatial shape across the pixel array, d) the failed whole data ellipse plot of the real and imaginary data

5.5 Discussion

The results from this Chapter demonstrate the use of the spatial phase-stepped HSSPI system to detect the presence of traveling waves. A Matlab model of traveling wave vibrations was developed and conditions of different types of vibrations was demonstrated. The model can be used to understand how the response data can identify the presence of traveling waves using a LMS ellipse-fit to the real and imaginary parts of the vibration. The learning from the model was then applied to demonstrate how the HSSPI spatial-phased system can be used to make multipoint parallel measurements to detect and measure traveling waves.

The experimental results shown in Figures 5.18 to 5.23 can be shown to have the presence of traveling waves through comparison to the simulation model results in Figures 5.2 to 5.8. Firstly an indication of traveling waves can be seen in the time-array images from the pure traveling wave model in Figure 5.5 and the experimental results in Figure 5.22. Where from the simulation model, a pure traveling wave would produce a constant angle in the time-data. The experimental results does show some of these lines of constant phase, but it is physically closer to the a mixture of a traveling and standing wave seen in Figure 5.3. The LMS-fit to the experimental data on the complex plane confirms this as in Figure 5.23 where the fit produced an ellipse indicating, as from the simulation results, the presence of both a standing wave and a traveling wave. The direction of the traveling wave is known from the positive gradient of the spatial-phase in Figure 5.23c, meaning the traveling wave is traveling from right to left on the viewing plane. The spatial wave shape can be extracted from the spatial-array vs frequency in Figure 5.23a and 5.23c.

In comparison, this process was applied to data that is unlikely to produce a traveling wave by analysing FM excitation data of frequencies that had a frequency gap too large to excite the degenerate modes. This was demonstrated using 241 Hz carrier frequency with the modulation frequency of 234 Hz giving a 7Hz difference in frequencies compared to the 0.5Hz difference in the data set that produced the traveling waves. The spatial-phase being constant across the pixels in Figure 5.25b and the LMS fit to the experimental data in Figure 5.25d shows a failed ellipse fit represented as a straight-line fit rather than an ellipse or circle. The analysis indicated that it was likely to be a standing wave with no traveling component.
In both cases the spatial-phase helped confirm the presence of travelling waves, by the first set of experimental data having a positive slope across the pixel-array and the second set having a constant phase across the pixel-array. The LMS-fits identified the ratio of traveling wave to standing wave but the accuracy of the LMS can be limited by the number of pixels used across the array. This can be seen in the comparison of

pixel lengths in Figure 5.8 column c where the trust given to the LMS-fit was much higher if the pixel array was longer: as the increased data already captures more features of an ellipse present. For the fit of the traveling wave experimental data in Figure 5.23 the quality of the LMS is weighted heavily on being at the end of the ellipse's primary axis to aid in the identification of the ellipse. A longer array would give more confidence to this, but the conclusion was supported by the spatial-phase and the time-array data data. For accuracy in the identification of these waves, an array should be at least a 1/4 of the wavelength's spatial waveshape being measured. Extending the length of the pixel array would also mean that a FFT could be applied directly to the spatial data to give a value for the spatial frequency instantaneously.

Limitations of the technique can be seen in modulation errors that arise form speckle techniques. Figure 5.23e shows this with the 7 points rejected from the ellipse-fit this is unavoidable in SPI methods but it will clearly effect the quality of fit.

This research can be seen as an extension of existing work on traveling waves described in Chapter 2. The work by Bucher et al [132, 133], this research would provide the spatial resolution and relative phase needed to develop and quantify models for their analysis: as opposed to the multiple testing and analysis using single point LDV and scanning LDV. This research can also be used to extend the work of Kilpatrick [107], Buckberry [105] and MacPherson [108] to understand the ratios of standing waves to traveling waves and the direction of the complex traveling waves in an attempt to extract the pure traveling wave that contribute to break squeal analysis.

5.6 Chapter summary

This Chapter has demonstrated the application of spatial phase-stepped HSSPI to the measurement and identification of traveling waves. The parallel measurement is used to instantly recognise traveling waves from the time-array data, the spatial-phase and its waveshape from the immediate data. This was then used to perform a LMS-fit to the real and complex parts of the vibration data that gave the ratio of standing wave to traveling waves. The traveling wave results were then compared to test data where there was no traveling waves present. Improvements to the accuracy were suggested for further research developments.

Chapter 6

Conclusion and Future work

This thesis presented the applications of laser transducers to vibration measurement and modal testing and has demonstrated the applications of HSSPI to impact modal testing and extended its use to the particular case of traveling wave analysis.

In Chapter 3 a temporal phase-stepped SPI system was used to perform impact modal testing of 2 plates overlapped at their edge. The response measurements were used to perform modal testing and analysis in order to quantify the experimental results in a modal model. This was compared to accelerometer tests of the same object and both were correlated against an FE model of the plates. It was demonstrated that the system could be used to perform impact modal testing to a reasonable degree of accuracy. Sources of error and the system limits were discussed, showing that the application of the system to modal analysis for impact is limited to below the Nyquist velocity of the system.

Chapter 4 extended the dynamic range of the HSSPI tests in Chapter 3 by replacing the temporal phase-step with a spatial phase-stepped SPI system. This system was used to perform impact modal testing of the same two overlapped plates as the temporal system. When correlated against an FE model the results showed that this system can be used to perform impact modal testing but with a similar performance to the temporal system. It was discussed that although the system's dynamic range had been increased with the introduction of spatial phase stepping, the extra line length needed to capture the spatial phase stepping reduces the maximum frame-rate of the CMOS detector, only bringing a relatively small increase to the system's velocity limit.

The final experimental Chapter, 5, demonstrated the use of parallel multipoint measurement of traveling waves on a centred clamped disc using HSSPI spatial phase-stepping. The direction, shape and the ratio of standing and traveling waves was identified using the HSSPI system. This was compared to other experimental data with no expected traveling waves and a theoretical model of traveling waves. Methods

to increase the accuracy and reliability of this application are discussed by extending the measurement pixel array length to ensure that the maximum spatial wave shape is captured, this could extend the applications to increase the effectiveness of traveling wave analysis.

The conclusions of this thesis are:

- Temporal phase-stepped HSSPI can be applied to successfully perform impact modal testing. The temporal phase-stepped system was shown to identify the natural frequency of the first 6 modes and was able to correlate 4 out of the first 6 mode shapes to above 80%. It was demonstrated that the temporal system's velocity limit of 1.4 mm/s needed to be extended to at least twice this to improve the system's modal analysis performance

- Spatial phase-stepped HSSPI can be applied to successfully perform impact modal testing for the first time. The spatial phase-stepped system had a velocity range three times that of the temporal phase-stepped system. The system accurately measured the first 6 natural frequencies and improved the correlation of the first 6 modes in the MAC showing a small improvement over the temporal system.

- Spatial phase-stepped HSSPI can be used to exploit their parallel vibration measurement ability to measure traveling waves and understand the ratio of standing waves to traveling waves. The multipoint system was shown to simplify the measurement process of traveling waves and extend this to identify the presence of standing and traveling waves. The multipoint functionality of the system could capture the regions of vibration without the need to do repeated tests and synchronise data that is associated with single point testing.

6.1 Future work

The limits of the system can be seen as possible research areas and could be summarised as the extension of the dynamic range, data processing and accuracy, and parallel measurement applications.

The dynamic range could be increased by exploring research areas in higher speed cameras such as Photonfocus MV-D1024E-160-CL that would improve both detectors velocity range by 40% or linear diode arrays that would dramatically increase the frame rates into the megahertz range, and increase the associated velocity limits by at least a factor of 10 for both temporal and spatial phase-stepping systems. The introduction of holographic optical elements [149, 150] could be applied to the system to simplify the alignment process for spatial phase-stepping. The use of the

unwrapping process developed by Wu [2] that allows sub-Nyquist analysis of spatial HSSPI data would increase the measurable velocity to over $4V_{Ny}$ without the need for hardware developments.

Research into the application of signal processing methods applied to the HSSPI data can improve its performance to modal analysis. This could be compared directly to the original LDV developments for modal testing [16, 65], the developments in hardware and signal processing greatly extending its performance and adoption. This could include hardware developments for data acquisition and the post-processing calculations that could extend work from Davila [116] to reduce phase errors in speckle data. An ideal vibration measurement device needs some form of pre-trigger ability that could take the form of a live buffer in order to capture crucial pieces of vibration data that simplifies the synchronization of the excitation signal to the response measurement.

The parallel measurement ability of the CMOS camera could also be expanded further by having multi-measurement regions on the sensor. This could be achieved through editing the registry of the camera, this would further reduce testing time for vibration applications and give the ability to measure more complex waves such as Kilpatrick's [64] MLV measurement device for traveling waves and close coupled waves.

Appendix A

Orthogonality and mass-normalisation of modal parameters

The modal parameters of the modal model form the dynamic characteristics of a structure. The modal model has mathematical properties that need to be defined to ensure any analysis and assumptions relating to it are clear. The first property that it possesses is its orthogonality properties, which can be stated as:

$$[\Psi]^T [M] [\Psi] = [m_r] \quad and \quad [\Psi]^T [K] [\Psi] = [k_r] \tag{A.1}$$

from which the natural frequency can be defined as:

$$\omega_r = [m_r]^{-1}[k_r] \tag{A.2}$$

where m_r and k_r are known as the modal mass and modal stiffness for mode r. The values of m_r and k_r are not unique to a particular mode due to the feature that the eigenvector solution 'directions' are unique but its magnitude is not. In analysis this tends to be simplified to ease extraction and the most effective of these is using mass-normalisation of the parameters. A mass normalised eigenvetor is denoted as $[\Phi]$ and its properties relate to the mass and stiffness by:

$$[\Phi]^T [M] [\Phi] = [I] \quad and\, gives: \quad [\Phi]^T [K] [\Phi] = [\omega_r^2] \tag{A.3}$$

The modeshape ψ_r for mode, r, can be expressed as the mass-normalised modeshape ϕ from:

$$\phi_r = \frac{\psi_r}{\sqrt{m_r}} \tag{A.4}$$

where m_r is expressed from:

$$m_r = \psi_r^T \, [M] \, \psi_r \tag{A.5}$$

or in terms of the mass-normalised eigenvector:

$$[\Phi] = [\Psi] \, [m_r^{-0.5}] \tag{A.6}$$

The orthogonality properties of the modal parameters from using the equation of motion for free vibration for a simple SDOF system:

$$[M]\{\ddot{x}\} + [K]\{x\} = 0 \tag{A.7}$$

Introducing an excitation of harmonic motion in terms of ω for the response x and its derivatives:

$$x = X \, e^{i\,\omega\,t} \quad ; \quad \dot{x} = i\,\omega\,X \, e^{i\,\omega\,t} \quad ; \quad \ddot{x} = -\omega^2 X \, e^{i\,\omega\,t} \tag{A.8}$$

inserting this into Equation A.7

$$\left([K] - \omega^2 \, [M]\right) \, \{X\} \, e^{i\,\omega\,t} = \{0\} \tag{A.9}$$

for a real mode:

$$\left([K] - \omega_r^2 \, [M]\right) \, \{\psi\}_r = \{0\} \tag{A.10}$$

pre-multiplying this by a different eigenvector transposed:

$$\{\psi\}_s^T \left([K] - \omega_r^2 \, [M]\right) \, \{\psi\}_r = \{0\} \tag{A.11}$$

For the different eigenvector we could write:

$$\left([K] - \omega_s^2 \, [M]\right) \, \{\psi\}_s = \{0\} \tag{A.12}$$

Which we can transpose and post multiply by $\{\psi\}_r$ to give:

$$\{\psi\}_s^T \left([K]^T - \omega_s^2 \, [M]^T\right) \, \{\psi\}_r = \{0\} \tag{A.13}$$

Assuming for this case and in general that both [M] and [K] are symmetrical, their identical transposes and the combined Equations A.11 and A.13 give:

$$\left(\omega_s^2 - \omega_r^2\right) \{\psi\}_s^T \, [M] \, \{\psi\}_r = \{0\} \tag{A.14}$$

which if $\omega_r \neq \omega_s$ can only be true if:

$$\{\psi\}_s^T \, [M] \, \{\psi\}_r = \{0\} \quad ; \quad r \neq s \tag{A.15}$$

With this condition, this would mean from A.11 or A.13 that:

$$\{\psi\}_s^T [K] \{\psi\}_r = \{0\} \quad ; \quad r \neq s \tag{A.16}$$

for cases where r = s or ($\omega_r = \omega_s$) both A.16 and A.15 do not apply and expanding Equation A.11 we would have:

$$\left(\{\psi\}_r^T [K] \{\psi\}_r\right) = \omega_r^2 \left(\{\psi\}_r^T [M] \{\psi\}_r\right) \tag{A.17}$$

giving:

$$\left(\{\psi\}_r^T [K] \{\psi\}_r\right) = k_r \quad and \quad \left(\{\psi\}_r^T [M] \{\psi\}_r\right) = m_r \tag{A.18}$$

that can be put together to demonstrate the relationship

$$\omega_r^2 = \frac{k_r}{m_r} \tag{A.19}$$

this can then be repeated for all combinations of r and s which leads to the full matrices seen in equations A.1

Solutions for λ and η. Using the general equation of motion:

$$[M]\{\ddot{x}\} + [K]x + i[H]\{x\} = \{F\}e^{i\omega t} \tag{A.20}$$

When there is no excitation force then F = 0 leaving:

$$[M]\{\ddot{x}\} + [K]x + i[H]\{x\} = 0 \tag{A.21}$$

if we assume a harmonic response the system can take we can say this about x and its derivatives:

$$x = X\, e^{i\,\lambda\, t} \quad ; \quad \dot{x} = i\,\lambda\, X\, e^{i\,\lambda\, t} \quad ; \quad \ddot{x} = -\lambda^2 X\, e^{i\,\lambda\, t} \tag{A.22}$$

which can be substituted into A.21:

$$-\lambda^2\, M\, X + K\, X + i\, H\, X = 0 \tag{A.23}$$

rearranging the terms we can show:

$$-\lambda^2 + \frac{K}{M} + \frac{i\, H}{M} = 0 \tag{A.24}$$

$$\lambda^2 = \frac{K}{M} + \frac{i\, H}{M} = 0 \tag{A.25}$$

substituting the relationship of ω_r we can have the above as:

$$\lambda^2 = \omega_r^2 \left(1 + \frac{i\,H}{M\,\omega_r^2}\right) \tag{A.26}$$

hysteric damping is proportional to both stiffness and mass and therefore can be expressed as:

$$H = \beta\,K + \gamma\,M \quad ; \quad \frac{i\,H}{M} = \frac{\beta\,K}{M} + \gamma = \beta\,\omega_r^2 + \gamma \tag{A.27}$$

using this in Equation A.26 and simplified:

$$\lambda^2 = \omega_r^2 \left(1 + i\left(\beta + \frac{\gamma}{\omega_r^2}\right)\right) \tag{A.28}$$

simplifications can be made to allow the imaginary parts of the equation to be the damping factor:

$$\eta = \beta + \frac{\gamma}{\omega_r^2} \tag{A.29}$$

so that Equation A.28 shows

$$\lambda^2 = \omega_r^2\,(1 + i\,\eta) \tag{A.30}$$

Solution to show orthogonal properties of FRF

$$K + i\,H - \omega^2\,M = [\alpha(\omega)]^{-1} \tag{A.31}$$

using the orthogonality properties above we have:

$$[\Phi]^T[K + i\,H - \omega^2\,M]\,[\Phi] = [\Phi]^T\,[\alpha(\omega)]^{-1}\,[\Phi] \tag{A.32}$$

taking only the LHS and rewriting the equation in terms of mass normalised parameters:

$$\frac{K}{M} + \frac{i\,H}{M} - \omega^2 \tag{A.33}$$

and substation using K and M for their relationship with ω_r

$$\omega_r^2 + \frac{i\,H}{M} - \omega^2 \tag{A.34}$$

and taking a common factor of ω_r

$$\omega_t^2(1 + \frac{i\,H}{M\,\omega_r}) - \omega^2 \tag{A.35}$$

as hysterics damping is proportional to both stiffness and mass and can be expressed as:

$$H = \beta\, K + \gamma\, M \tag{A.36}$$

which can be rewritten as:

$$\frac{H}{M} = \frac{\beta\, K}{M} + \gamma = \beta\, \omega_r^2 + \gamma \tag{A.37}$$

and substituted into A.35 gives the expression:

$$\omega_r^2(1 + i\,\beta + \frac{\gamma}{\omega_r^2}) - \omega^2 \tag{A.38}$$

this can be simplified by introducing the hysteric damping factor η:

$$\omega_r^2(1 + i\,\eta) - \omega^2 \quad ; \quad \eta = \beta + \frac{\gamma}{\omega_r^2} \tag{A.39}$$

using the relationship A.30 the substation can be made for λ

$$\lambda_r^2 - \omega^2 \quad ; \quad \lambda_r^2 = \omega_r^2(1 + i\,\eta) \tag{A.40}$$

this being the orthogonal properties of the LHS of Equation A.32 and leaves with the expression:

$$\lambda_r^2 - \omega^2 = [\Phi]^T\, [\alpha(\omega)]^{-1}\, [\Phi] \tag{A.41}$$

Appendix B

Measurement points

Node	X (co-ord)(m)	Y(co-ord) (m)
869	0.01389	0.13975
1415	0.04304	0.11697
1429	0.04534	0.03105
1674	0.10752	0.08122
1723	0.09404	0.02561
1793	0.10723	0.02614
1800	0.12055	0.05381
1856	0.13051	0.11976
2339	0.12065	0.0676
2479	0.06851	0.0994
2507	0.04959	0.08365
2605	0.13671	0.02705
2794	0.07501	0.10761
3004	0.09345	0.14381
3767	0.02	0.02468
4684	-0.0333	0.03523
4761	-0.0679	0.06337
4803	-0.0332	0.12119
4838	-0.0717	0.02706
4873	-0.0602	0.1219
4929	-0.0986	0.09486
5076	-0.1143	0.1372
5160	-0.1136	0.03253
5181	-0.1174	0.10135
5223	-0.0735	0.12144
5503	-0.00245	0.00737
5573	-0.1039	0.02884
5622	-0.0296	0.03261
5930	-0.00535	0.07276
6462	0.00102	0.076

Table B.1: Test point locations

Appendix C

FM signal sidebands

Frequency modulated signals are built with two components. A carrier frequency, ω_c and a modulation frequency, ω_{FM}. A FM signal when seen in the frequency domain has two sidebands and are a function of the carrier frequency and the modulated signal, these sidebands appear proportionally above and below the the carrier frequency and from this they get their names the "upper sideband" and "lower sideband".
The frequency location of where these sidebands occur can be calculated from:

$$Uppersideband = cos(\omega_c + \omega_{FM})\, t \tag{C.1}$$

and

$$Lowersideband = cos(\omega_c - \omega_{FM})\, t \tag{C.2}$$

In normal applications both ω_c and ω_{FM} are different but in cases where $\omega_c = \omega_{FM}$.

$$Uppersideband = cos(\omega_c + \omega_{FM})\, t = cos(\omega_c + \omega_c)\, t = cos(2\omega_c)\, t \tag{C.3}$$

and

$$Lowersideband = cos(\omega_c - \omega_{FM})\, t = cos(\omega_c - \omega_c)\, t = cos(0)\, t = 0 \tag{C.4}$$

Meaning in cases where $\omega_c = \omega_{FM}$, only an upper side band would be present

References

[1] T. Wu, J. D. C. Jones, and A. J. Moore. High-speed phase-stepped digital speckle pattern interferometry using a complementary metal-oxide semiconductor camera. *Applied Optics*, 45(23):5845, August 2006. ISSN 0003-6935. URL http://ao.osa.org/abstract.cfm?URI=ao-45-23-5845.

[2] T. Wu, J. D. Valera, and A. J. Moore. High-speed sub-Nyquist interferometry. *Optics Express*, 19(11):10111, May 2011. ISSN 1094-4087. URL http://www.opticsexpress.org/abstract.cfm?URI=oe-19-11-10111.

[3] D. J. Ewins. *Modal Testing: Theory, Practice and Application (Mechanical Engineering Research Studies: Engineering Dynamics Series)*. Wiley-Blackwell, 2000. URL http://www.amazon.co.uk/Modal-Testing-Application-Mechanical-Engineering/dp/0863802184.

[4] R. M. Lin and J. Zhu. On the relationship between viscous and hysteretic damping models and the importance of correct interpretation for system identification. *Journal of Sound and Vibration*, 325(1-2):14–33, August 2009. ISSN 0022460X. doi: 10.1016/j.jsv.2009.02.051. URL http://dx.doi.org/10.1016/j.jsv.2009.02.051.

[5] D. L. Brown, R. J. Allemang, R. Zimmerman, and M. Mergeay. Parameter estimation techniques for modal analysis. *SAE Transaction SAE Paper No 790221*, Paper 7902:828–846, 1979.

[6] P. Castellini, G. M Revel, L. Scalise, and R. M. De Andrade. Experimental and numerical investigation on structural effects of laser pulses for modal parameter measurement. *Optics and Lasers in Engineering*, 32(6):565–581, 2000. ISSN 01438166. doi: 10.1016/S0143-8166(00)00003-8. URL http://linkinghub.elsevier.com/retrieve/pii/S0143816600000038.

[7] P. Castellini. Measurement of vibrational modal parameters using laser pulse excitation techniques. *Measurement*, 35(2):163–179, March 2004. ISSN 02632241.

doi: 10.1016/j.measurement.2003.07.004. URL http://linkinghub.elsevier.com/retrieve/pii/S0263224103000848.

[8] M. Xu. Impact testing and its applications, part I. *Shock and Vibration Digest*, 29(3):8–17, 1997. URL http://www.scopus.com/scopus/inward/record.url?eid=2-s2.0-0031143971&partnerID=40&rel=R5.6.0.

[9] T. G. Carne and E. C. Stasiunas. Lessons learned in modal testing - Part 3: Transient excitation for modal testing, more than just hammer impacts. *Experimental Techniques*, 30(3):69–79, 2006. URL http://www.scopus.com/scopus/inward/record.url?eid=2-s2.0-33646765725&partnerID=40&rel=R5.6.0.

[10] R. J. Allemang. The Modal Assurance Criterion Twenty Years of Use and Abuse. *Sound And Vibration*, 37(8):14–23, 2003.

[11] M. Pastor, M. Binda, and T. áš Harčarik. Modal Assurance Criterion. *Procedia Engineering*, 48(null):543–548, January 2012. ISSN 18777058. doi: 10.1016/j.proeng.2012.09.551. URL http://dx.doi.org/10.1016/j.proeng.2012.09.551.

[12] P. R. Ind P.M. Daborn A. Tribe, K. Garraway. Development of a New Automated Modal Test Planning Algorithm. In Sds, editor, *International Conference on Noise and Vibration Engineering*, page 2483, Katholieke Universiteit Leuven, Belgium, 2006.

[13] K. G. McConnell and P. S. Varoto. *Vibration Testing: Theory and Practice*. John Wiley & Sons, 1995. URL http://www.amazon.co.uk/Vibration-Testing-Practice-Kenneth-McConnell/dp/0471304352.

[14] A. C. Pisoni, C. Santolini, D. E. Hauf, and S. Dubowsky. Displacements in a vibrating body by strain gauge measurements. In *Proceedings of the 13th International Conference on Modal Analysis*, 1995.

[15] P. Castellini, M. Martarelli, and E.P. Tomasini. Laser Doppler Vibrometry: Development of advanced solutions answering to technology's needs. *Mechanical Systems and Signal Processing*, 20(6):1265–1285, August 2006. ISSN 08883270. doi: 10.1016/j.ymssp.2005.11.015. URL http://dx.doi.org/10.1016/j.ymssp.2005.11.015.

[16] A. B. Stanbridge and D. J. Ewins. Modal testing using a scanning laser doppler vibrometer. *Mechanical Systems and Signal Processing*, 13(2):255–270, March 1999. ISSN 08883270. doi: 10.1006/mssp.1998.1209. URL http://dx.doi.org/10.1006/mssp.1998.1209.

[17] S. J. Rothberg, J. R. Baker, and N. A. Halliwell. Laser vibrometry: Pseudo-vibrations. *Journal of Sound and Vibration*, 135(3):516–522, December 1989. ISSN 0022460X. doi: 10.1016/0022-460X(89)90705-0. URL http://dx.doi.org/10.1016/0022-460X(89)90705-0.

[18] P. Castellini, N. Paone, and E. P. Tomasini. Application of a laser Doppler vibrometer to nonintrusive diagnostic of frescoes damage. *Proceedings of SPIE - The International Society for Optical Engineering*, 2358:70–77, 1994. URL http://www.scopus.com/scopus/inward/record.url?eid=2-s2.0-0028709934&partner=40&rel=R5.0.4.

[19] A. B. Stanbridge and D. J. Ewins. Measurement of translational and angular vibration using a scanning laser Doppler vibrometer. *Shock and Vibration*, 3(2):141–152, 1996. URL http://www.scopus.com/scopus/inward/record.url?eid=2-s2.0-0000314517&partnerID=40&rel=R5.6.0.

[20] A. Hocknell, R. Jones, and S. J. Rothberg. Remote vibration measurements: Compensation of waveform distortion due to whole body translations. *Journal of Sound and Vibration*, 214(2):285–307, 1998. URL http://www.scopus.com/scopus/inward/record.url?eid=2-s2.0-0039527103&partnerID=40&rel=R5.6.0.

[21] P. Castellini, E. Esposito, F. Miandro, N. Paone, C. Santolini, and E. P. Tomasini. Non-invasive measurements of structural damage by Laser Scanning Vibrometer: An experimental comparison among different exciters. In *Proceedings of the International Modal Analysis Conference - IMAC*, volume 1, pages 692–698, 1999. URL http://www.scopus.com/scopus/inward/record.url?eid=2-s2.0-0032654727&partner=40&rel=R5.0.4.

[22] R. B. Jenal, W. J. Staszewski, and A. Klepka. Structural Damage Detection Using Laser Vibrometers. *Modal Analysis*, 11:1–8, 2010. URL http://www.ndt.net/article/aero2010/papers/tu1b3.pdf.

[23] P. Castellini, F. Giovanucci, G. Nava-Mambretti, L. Scalise, and E. P. Tomasini. Vibration analysis of tyre treads: An in-plane laser vibrometry approach. In *Proceedings of the International Modal Analysis Conference - IMAC*, volume 2, pages 1732–1738, 1998. URL http://www.scopus.com/scopus/inward/record.url?eid=2-s2.0-0031701164&partner=40&rel=R5.0.4.

[24] G. M. Revel, C. Santolin, and E. P. Tomasini. Laser-Doppler vibration and acoustic intensity measurements for dynamic characterization and

noise reduction of a car window lift system. In *Proceedings of the International Modal Analysis Conference - IMAC*, volume 2, pages 1636–1642, 1997. URL http://www.scopus.com/scopus/inward/record.url?eid=2-s2.0-0031337561&partner=40&rel=R5.0.4.

[25] P. Castellini. Vibration measurements for diagnosis of structural defects on human teeth. *Measurement*, 27(1):29–42, January 2000. ISSN 02632241. doi: 10.1016/S0263-2241(99)00049-4. URL http://linkinghub.elsevier.com/retrieve/pii/S0263224199000494.

[26] P. Castellini and E. P. Tomasini. Laser technique for defects diagnostics in composite materials. In *Proceedings of the International Modal Analysis Conference - IMAC*, volume 2, pages 1745–1749, 1998. URL http://www.scopus.com/scopus/inward/record.url?eid=2-s2.0-0031675144&partner=40&rel=R5.0.4.

[27] P. Castellini, G. M. Revel, and E. P. Tomasini. Diagnostic of composite materials by laser techniques: Application on panels with different structures and shapes. *Proceedings of the International Modal Analysis Conference - IMAC*, 1:710–716, 2001. URL http://www.scopus.com/scopus/inward/record.url?eid=2-s2.0-0035046172&partner=40&rel=R5.0.4.

[28] E. P. Tomasini, F. Piazza, E. Esposito, and M. Possanzini. Non-destructive diagnostics of layered structures: Advanced signal analysis algorithms applied to vibrometric data. *Proceedings of the International Modal Analysis Conference - IMAC*, 2:1604–1610, 2000. URL http://www.scopus.com/scopus/inward/record.url?eid=2-s2.0-0033886288&partner=40&rel=R5.0.4.

[29] J. R. Bell and S. J. Rothberg. Laser Vibrometers and Contacting Transducers, Target Rotation and Six Degree-of-Freedom Vibration: What Do We Really Measure? *Journal of Sound and Vibration*, 237(2):245–261, October 2000. ISSN 0022460X. doi: 10.1006/jsvi.2000.3053. URL http://linkinghub.elsevier.com/retrieve/pii/S0022460X00930530.

[30] J. R. Bell and S. J. Rothberg. Rotational vibration measurements using laser Doppler vibrometry: comprehensive theory and practical application. *Journal of Sound and Vibration*, 238(4):673–690, 2000. URL http://www.scopus.com/scopus/inward/record.url?eid=2-s2.0-0034498044&partner=40&rel=R5.0.1.

[31] B. J. Halkon and S. J. Rothberg. Rotor vibration measurements using laser doppler vibrometry: Essential post-processing for resolution of radial and pitch/yaw vibrations. *Journal Of Vibration And Acoustics Transactions Of*

The Asme, 128(1):8–20, 2006. URL http://www.scopus.com/scopus/inward/record.url?eid=2-s2.0-33645735288&partner=40&rel=R5.0.1.

[32] D. Di Maio and D. J. Ewins. Continuous Scan, a method for performing modal testing using meaningful measurement parameters; Part I. *Mechanical Systems and Signal Processing*, 25(8):3027–3042, 2011. ISSN 08883270. doi: 10.1016/j.ymssp.2011.05.018. URL http://dx.doi.org/10.1016/j.ymssp.2011.05.018.

[33] S. J. Rothberg, B. J. Halkon, M. Tirabassi, and C. Pusey. Radial vibration measurements directly from rotors using laser vibrometry: The effects of surface roughness, instrument misalignments and pseudo-vibration. *Mechanical Systems and Signal Processing*, 33(null):109–131, November 2012. ISSN 08883270. doi: 10.1016/j.ymssp.2012.06.011. URL http://dx.doi.org/10.1016/j.ymssp.2012.06.011.

[34] T. Miles. Torsional and Bending Vibration Measurement on Rotors Using Laser Technology. *Journal of Sound and Vibration*, 226(3):441–467, September 1999. ISSN 0022460X. doi: 10.1006/jsvi.1999.2253. URL http://linkinghub.elsevier.com/retrieve/pii/S0022460X99922538.

[35] Polytec GmbH. Polytec: PSV-500-3D Scanning Vibrometer. URL http://www.polytec.com/us/products/vibration-sensors/scanning-vibrometers/psv-500-3d-scanning-vibrometer/.

[36] A. B. Stanbridge and D. J. Ewins. Measurement of translational and angular vibration using a scanning laser Doppler vibrometer. *Proceedings of SPIE - The International Society for Optical Engineering*, 2358:37–47, 1994. URL http://www.scopus.com/scopus/inward/record.url?eid=2-s2.0-0028727978&partnerID=40&rel=R5.6.0.

[37] A. B. Stanbridge and D. J. Ewins. Modal testing of rotating discs using a scanning LDV. In K W Wang, B Yang, J Q Sun, K Seto, K Yoshida, and Et Al., editors, *American Society of Mechanical Engineers Design Engineering Division Publication DE*, volume 84, pages 1207–1213, 1995. URL http://www.scopus.com/scopus/inward/record.url?eid=2-s2.0-0029428567&partnerID=40&rel=R5.6.0.

[38] A. B. Stanbridge and D. J. Ewins. Measurement of total vibration at a point using a conical-scanning LDV. In P Tomasini Enrico, editor, *Proceedings of SPIE - The International Society for Optical Engineering*, volume 2868, pages 126–136, Washington, DC, USA, 1996. ISBN 0819422649

(ISBN). URL http://www.scopus.com/scopus/inward/record.url?eid=2-s2.0-0030392993&partnerID=40&rel=R5.6.0.

[39] K. Venkatakrishnan, B. Tan, and B. K. A. Ngoi. Two-axis-scanning laser Doppler vibrometer for precision engineering. *Optics and Lasers in Engineering*, 38:153–171, 2002.

[40] R. A. Lomenzo, A. J. Barker, and A. L. Wicks. Laser vibrometry system for rotating bladed disks. In Anon, editor, *Proceedings of the International Modal Analysis Conference IMAC*, volume 1, pages 277–282. SEM, Bethel, CT, United States, 1999. URL http://www.scopus.com/inward/record.url?eid=2-s2.0-0032625368&partnerID=40&md5=8a52965e3779378e3d6fa4b6cf6d7db5.

[41] S. Vanlanduit, B. Cauberghe, P. Guillaume, and P. Verboven. Automatic vibration mode tracking using a scanning laser Doppler vibrometer. *Optics and Lasers in Engineering*, 42(3):315–326, 2004. URL http://www.scopus.com/scopus/inward/record.url?eid=2-s2.0-2142750176&partnerID=40&rel=R5.6.0.

[42] B. Halkon and S. Rothberg. Continuous Scanning Laser Vibrometry for Measurements on Rotating Structures. In M P Cartmell, editor, *Materials Science Forum*, volume 440-441, pages 245–252, Glasgow, Scotland, 2003. ISBN 02555476 (ISSN). URL http://www.scopus.com/scopus/inward/record.url?eid=2-s2.0-0345358485&partnerID=40&rel=R5.6.0.

[43] B. Halkon and S. Rothberg. Synchronised-scanning laser vibrometry. In E P Tomasini, editor, *Proceedings of SPIE - The International Society for Optical Engineering*, volume 5503, pages 260–271, Ancona, 2004. ISBN 0277786X (ISSN). URL http://www.scopus.com/scopus/inward/record.url?eid=2-s2.0-3843144957&partner=40&rel=R5.0.1.

[44] B. Halkon and S Rothberg. Vibration measurements using continuous scanning laser vibrometry: Advanced aspects in rotor applications. *Mechanical Systems and Signal Processing*, 20(6):1286–1299, 2006. ISSN 08883270. doi: 10.1016/j.ymssp.2005.11.009. URL http://linkinghub.elsevier.com/retrieve/pii/S0888327005002177.

[45] I. A. Sever, A. B. Stanbridge, and D. J. Ewins. Turbomachinery blade vibration measurements with tracking LDV under rotation. In *Proceedings of SPIE - The International Society for Optical Engineering*, volume 6345, Ancona, 2006. ISBN 0277786X (ISSN); 081946421X (ISBN); 9780819464217 (ISBN). URL http://www.scopus.com/scopus/inward/record.url?eid=2-s2.0-33748681356&partnerID=40&rel=R5.6.0.

[46] A. B. Stanbridge, M. Martarelli, and D. J. Ewins. Measuring area vibration mode shapes with a continuous-scan LDV. *Measurement*, 35(2):181–189, March 2004. ISSN 02632241. doi: 10.1016/j.measurement.2003.07.005. URL http://dx.doi.org/10.1016/j.measurement.2003.07.005.

[47] A. B. Stanbridge. Measuring area vibration mode shapes with a continuous-scan LDV. *Measurement*, 35(2):181–189, March 2004. ISSN 02632241. doi: 10.1016/j.measurement.2003.07.005. URL http://linkinghub.elsevier.com/retrieve/pii/S026322410300085X.

[48] M. Martarelli. Automated Modal Analysis By Scanning Laser Vibrometry: Problems and Uncertainties Associated With the Scanning System Calibration. *Mechanical Systems and Signal Processing*, 15(3):581–601, May 2001. ISSN 08883270. doi: 10.1006/mssp.2000.1336. URL http://linkinghub.elsevier.com/retrieve/pii/S0888327000913360.

[49] A. B. Stanbridge, M. Martarelli, and D. J. Ewins. Rotating disc vibration analysis with a circular-scanning LDV. *Proceedings of the International Modal Analysis Conference IMAC*, 1:464–469, 2001. ISSN 10466770. URL http://www.scopus.com/inward/record.url?eid=2-s2.0-0035050775&partnerID=40&md5=1f37642343a8255ee76f1f7bb7dbd1ac.

[50] M. S. Kang, A. B. Stanbridge, T. G. Chang, and H. S. Kim. Measuring mode shapes with a continuously scanning laser vibrometer - Hilbert transform approach. *Mechanical Systems and Signal Processing*, 16(2-3):201–210, 2002. URL http://www.scopus.com/scopus/inward/record.url?eid=2-s2.0-2342427554&partnerID=40&rel=R5.6.0.

[51] A. Brehmer. Measurement of real normal modes with adapted resolution by means of a continuously scanning laser vibrometer. *Mechanical Systems and Signal Processing*, 18(5):1203–1218, September 2004. ISSN 08883270. doi: 10.1016/j.ymssp.2003.10.003. URL http://linkinghub.elsevier.com/retrieve/pii/S0888327003001304.

[52] A. Khan. Detecting damage in vibrating structures with a scanning LDV. *Optics and Lasers in Engineering*, 32(6):583–592, December 2000. ISSN 01438166. doi: 10.1016/S0143-8166(00)00004-X. URL http://linkinghub.elsevier.com/retrieve/pii/S014381660000004X.

[53] A. Petreli, H. Sol, and P. Guillaume. Damage identification by inverse methods using a laser velocity scanner. In *Proceedings of the 2006 SEM Annual*

Conference and Exposition on Experimental and Applied Mechanics 2006, volume 3, pages 1417–1426, Saint Louis, MO, 2006. ISBN 091205395X (ISBN); 9780912053950 (ISBN). URL http://www.scopus.com/scopus/inward/record.url?eid=2-s2.0-33750293382&partnerID=40&rel=R5.6.0.

[54] A. Dierickx, H. Sol, and P. Guillaume. Damage identification of brittle materials using scanning laser Doppler vibrometer. In P Sas and M Munck, editors, *Proceedings of the 2004 International Conference on Noise and Vibration Engineering, ISMA*, pages 2301–2311, Leuven, 2004. ISBN 9073802822 (ISBN). URL http://www.scopus.com/scopus/inward/record.url?eid=2-s2.0-13344295041&partnerID=40&rel=R5.6.0.

[55] S. Vanlanduit, P. Guillaume, J. Schoukens, and E. Parloo. Linear and nonlinear damage detection using a scanning laser vibrometer. *Shock and Vibration*, 9(1-2):43–56, 2002. URL http://www.scopus.com/scopus/inward/record.url?eid=2-s2.0-0036261170&partnerID=40&rel=R5.6.0.

[56] S. Vanlanduit, P. Guillaume, and J. Schoukens. High spatial resolution modal parameter estimation using a parametric MLE-like algorithm. In *Proceedings of the 23rd International Conference on Noise and Vibration Engineering ISMA*, pages 997–1004, 1998. ISBN 9073802679. URL http://www.scopus.com/scopus/inward/record.url?eid=2-s2.0-13444269090&partnerID=40&rel=R5.6.0.

[57] S. Vanlanduit and P. Guillaume. An automatic scanning algorithm for high spatial resolution laser vibrometer measurements. *Mechanical Systems and Signal Processing*, 18(1):79–88, 2004. URL http://www.scopus.com/scopus/inward/record.url?eid=2-s2.0-0345134881&partnerID=40&rel=R5.6.0.

[58] B. J. Halkon and S. J. Rothberg. Rotor vibration measurements using laser doppler vibrometry: Essential post-processing for resolution of radial and pitch/yaw vibrations. *Journal of Vibration and Acoustics, Transactions of the ASME*, 128(1):8–20, 2006. URL http://www.scopus.com/scopus/inward/record.url?eid=2-s2.0-33645735288&partner=40&rel=R5.0.1.

[59] M. S. Allen and M. W. Sracic. A new method for processing impact excited continuous-scan laser Doppler vibrometer measurements. *Mechanical Systems and Signal Processing*, 24(3):721–735, April 2010. ISSN 08883270. doi: 10.1016/j.ymssp.2009.11.004. URL http://dx.doi.org/10.1016/j.ymssp.2009.11.004.

[60] S. Rothberg and B. Halkon. Laser Vibrometry meets laser speckle. In E P Tomasini, editor, *Proceedings of SPIE - The International Society for*

Optical Engineering, volume 5503, pages 280–291, Ancona, 2004. ISBN 0277786X (ISSN). URL http://www.scopus.com/scopus/inward/record.url?eid=2-s2.0-3843103574&partner=40&rel=R5.0.1.

[61] W. Zheng, R. V. Kruzelecky, and R. Changkakoti. Multichannel laser vibrometer and its applications. In Enrico P. Tomasini, editor, *Third International Conference on Vibration Measurements by Laser Techniques: Advances and Applications*, pages 376–384, June 1998. doi: 10.1117/12.307722. URL http://proceedings.spiedigitallibrary.org/proceeding.aspx?articleid=954110.

[62] E. Cupido; D. Smith; Image Automation Ltd.; S. Morel. Multipoint Laser Doppler Vibrometer for Transient Analysis, 2003. URL http://www.sem.org/Proceedings/ConferencePapers-Paper.cfm?ConfPapersPaperID=25792.

[63] L. Scalise and R. Di Sante. Single-mode optical fiber interferometer for surface vibration measurement. In Brian Culshaw, James A. Harrington, Michael A. Marcus, and Mohammed Saad, editors, *Environmental and Industrial Sensing*, pages 115–123, March 2001. doi: 10.1117/12.417400. URL http://proceedings.spiedigitallibrary.org/proceeding.aspx?articleid=895289.

[64] J. Kilpatrick and V. Markov. Multi-Pixel (Matrix) Laser Vibrometer. *Imaging*, (iii):2–4, 2010.

[65] M. Martarelli, G. M. Revel, and C. Santolini. On the use of Laser Doppler Vibrometry for modal analysis. In *Proceedings of the International Modal Analysis Conference IMAC*, volume 2, pages 1750–1757. SEM, Bethel, CT, United States, 1998. URL http://www.scopus.com/inward/record.url?eid=2-s2.0-0031679334&partnerID=40&md5=e42f8c94ecca77f6e1416e474dc5efe8.

[66] A. B. Stanbridge and D. J. Ewins. Scanning laser Doppler vibrometer measurements for vibrating beam model updating. In *Proceedings of the International Modal Analysis Conference - IMAC*, volume 2, pages 1498–1504, Santa Barbara, CA, USA, 1998. SEM. ISBN 10466770 (ISSN). URL http://www.scopus.com/scopus/inward/record.url?eid=2-s2.0-0031675140&partnerID=40&rel=R5.6.0.

[67] A. B. Stanbridge, M. Martarelli, and D. J. Ewins. Measuring area mode shapes with a scanning laser Doppler vibrometer. In Anon, editor, *Proceedings of the International Modal Analysis Conference IMAC*, volume 1, pages 980–985. Citeseer, 1999. URL http://citeseerx.ist.psu.edu/viewdoc/download?doi=10.1.1.18.3753&rep=rep1&type=pdf.

[68] A. B. Stanbridge and D. J. Ewins. Extraction of damped and undamped natural mode shapes from area-scan ODSs. In *Proceedings of SPIE - The International Society for Optical Engineering*, volume 6345, Ancona, 2006. ISBN 0277786X (ISSN); 081946421X (ISBN); 9780819464217 (ISBN). URL http://www.scopus.com/scopus/inward/record.url?eid=2-s2.0-33748687651&partner=40&rel=R5.0.4.

[69] E. B. Skrodzka and A. P. Sk. Comparison of modal parameters of loudspeakers in different working conditions. *Applied Acoustics*, 60(3):267–277, July 2000. ISSN 0003682X. doi: 10.1016/S0003-682X(99)00050-X. URL http://dx.doi.org/10.1016/S0003-682X(99)00050-X.

[70] J. L. Potter and C. D. VanKarsen. Comparison of Modal Analysis Between Laser Vibrometry and NAH Measurements. *Topics in Modal Analysis*, 30:471–480, 2012. doi: 10.1007/978-1-4614-2425-3. URL http://www.springerlink.com/index/10.1007/978-1-4614-2425-3.

[71] J. Chen and D. Jiang. Modal analysis of wind turbine tower, 2010. URL http://link.aip.org/link/JSEEDO/v124/i4/p364/s1&Agg=doi.

[72] R. B. Adamson, C. L. McKnight, W. A. Alian, M. L. Bance, D. A. Doman, and J. A. Brown. Three-dimensional laser Doppler vibrometry of the dry human skull. *Journal of the Acoustical Society of America*, 128(4):2363, 2010.

[73] A. B. Stanbridge, A. Z. Khan, and D. J. Ewins. Modal testing using impact excitation and a scanning LDV. *Shock and Vibration*, 7(2):91–100, 2000. URL http://www.scopus.com/scopus/inward/record.url?eid=2-s2.0-0033705073&partnerID=40&rel=R5.6.0.

[74] R. Ribichini; D. Di Maio; A.B. Stanbridge; D. J. Ewins. Impact Testing With a Continuously-Scanning LDV, 20. URL http://sem-proceedings.com/26i/sem.org-IMAC-XXVI-Conf-s11p01-Impact-Testing-With-Continuously-scanning-LDV.pdf.

[75] R. L. Powell and K. A. Stetson. Interferometric vibration analysis by wavefront reconstruction. *Journal of the Optical Society of America*, 55(12):1593–1598, 1965. ISSN 00303941. doi: 10.1364/JOSA.55.001593. URL http://www.opticsinfobase.org/abstract.cfm?&id=52861.

[76] A. K. STETSON and R. L. POWELL. Interferometric Hologram Evaluation and Real-Time Vibration Analysis of Diffuse Objects. *Journal of the Optical Society of America*, 55(12):1694, December 1965. ISSN 0030-3941. doi:

10.1364/JOSA.55.001694. URL http://www.opticsinfobase.org/abstract.cfm?URI=josa-55-12-1694.

[77] J. Bulabois, M. E. Guillaume, and J. C. Viénot. Applications of the speckle pattern techniques to the visualization of modulation transfer functions and quantitative study of vibrations of mechanical structures. *Applied Optics*, 12 (7):1686–1692, 1973. doi: 10.1364/AO.12.001686.

[78] H. J. Tiziani and J. Klenk. Vibration analysis by speckle techniques in real time. *Applied Optics*, 20(8):1467–1470, 1981. doi: 10.1364/AO.20.001467.

[79] K. Høgmoen and O. J. Løkberg. Detection and measurement of small vibrations using electronic speckle pattern interferometry. *Applied Optics*, 16(7):1869, July 1977. ISSN 0003-6935. doi: 10.1364/AO.16.001869. URL http://ao.osa.org/abstract.cfm?URI=ao-16-7-1869.

[80] C. Wykes. Use Of Electronic Speckle Pattern Interferometry (ESPI) In The Measurement Of Static And Dynamic Surface Displacements. *Optical Engineering*, 21(3):213400, June 1982. ISSN 0091-3286. doi: 10.1117/12.7972922. URL http://opticalengineering.spiedigitallibrary.org/article.aspx?articleid=1222311.

[81] K. Creath. Vibration-observation techniques for digital speckle-pattern interferometry. *JOSA A*, 2(10):1629–1636, 1985. ISSN 10847529. doi: 10.1364/JOSAA.2.001629. URL http://www.opticsinfobase.org/abstract.cfm?URI=josaa-2-10-1629.

[82] J. D. R. Valera and J. D. C. Jones. Vibration analysis by modulated time-averaged speckle shearing interferometry. *Measurement Science and Technology*, 6(7):965–970, 1995. URL http://www.scopus.com/scopus/inward/record.url?eid=2-s2.0-0029344999&partnerID=40&rel=R5.6.0.

[83] O. J. Løkberg and K. Høgmoen. Vibration phase mapping using electronic speckle pattern interferometry. *Applied optics*, 15(11):2701–4, November 1976. ISSN 0003-6935. URL http://www.ncbi.nlm.nih.gov/pubmed/20165478.

[84] O. J. Løkberg, K. Høgmoen, and O. M. Holje. Vibration measurement on the human ear drum in vivo. *Applied Optics*, 18(6):763–765, 1979. doi: 10.1364/AO.18.000763.

[85] K. A. Stetson and W. R. Brohinsky. Electro-optic holography system for vibration analysis and nondestructive testing. *Opt eng*, 26(12):1234–1239, 1987.

[86] O. J. Løkberg, J. T. Malmo, and A. Strand. TV-HOLOGRAPHY - A TOOL FOR VIBRATION MEASUREMENTS. *Noise vibration control worldwide*, 18(9):286–289, 1987. URL http://www.scopus.com/scopus/inward/record.url?eid=2-s2.0-0023434363&partnerID=40&rel=R5.6.0.

[87] T. Ng and F. Chau. A digital shearing speckle interferometry technique for modal analysis. *Applied Acoustics*, 42(2):175–185, 1994. ISSN 0003682X. doi: 10.1016/0003-682X(94)90006-X. URL http://linkinghub.elsevier.com/retrieve/pii/0003682X9490006X.

[88] C. H. Buckberry, D. P. Towers, B. C. Stockley, B. Tavender, M. P. Jones, J. D. C. Jones, and J. D. R. Valera. Whole-field optical diagnostics for structural analysis in the automotive industry. *Optics and Lasers in Engineering*, 25(6 SPEC. ISS.):433–453, 1996. URL http://www.scopus.com/scopus/inward/record.url?eid=2-s2.0-0030527697&partnerID=40&rel=R5.6.0.

[89] W. O. Wong. Vibration-mode Shape Visualization with a Time Average TV Holography System *. *Computer*, 14(4):241–247, 1998.

[90] H. Vold, B. Schwarz, and M. Richardson. Measuring operating deflection shapes under non-stationary conditions. In *Proceedings of the International Modal Analysis Conference IMAC*, volume 2, pages 1655–1660. SEM, United States, 2000. URL http://www.scopus.com/inward/record.url?eid=2-s2.0-0033887190&partnerID=40&md5=1f0131fa1a95c1388dd977ddfb2eab89.

[91] P. Picart, J. Levai, J. C. Pascal, J. P. Boileau, M. Grill, J. M. Breteau, B. Gautier, and S. Gillet. 2D full field vibration analysis with multiplexed digital holograms. *Optics Express*, 13(22):8882–8892, 2005. URL http://www.scopus.com/scopus/inward/record.url?eid=2-s2.0-27544439016&partner=40&rel=R5.0.4.

[92] H. Y. Lin and C. C. Ma. The influence of electrode designs on the resonant vibrations for square piezoceramic plates. *IEEE Transactions on Ultrasonics, Ferroelectrics, and Frequency Control*, 53(5):825–837, 2006. URL http://www.scopus.com/scopus/inward/record.url?eid=2-s2.0-33744724337&partner=40&rel=R5.0.1.

[93] T. Eck, S. J. Walsh, M. Dale, and N. Taylor. Vibrational power flow measurement in a beam using electronic speckle pattern interferometry. *Acta Acustica united with Acustica*, 92(5):765–776, 2006. URL http://www.scopus.com/scopus/inward/record.url?eid=2-s2.0-33750315893&partner=40&rel=R5.0.4.

[94] L. Bingleman and G. S. Schajer. ESPI measurements in the presence of large lateral displacements. In *Society for Experimental Mechanics SEM Annual Conference and Exposition on Experimental and Applied Mechanics 2010*, volume 2, pages 1039–1047, 2010.

[95] T. J. Cookson, J. N. Butters, and H. C. Pollard. Pulsed lasers in electronic speckle pattern interferometry. *Optics & Laser Technology*, 10(3):119–124, June 1978. ISSN 00303992. doi: 10.1016/0030-3992(78)90057-9. URL http://dx.doi.org/10.1016/0030-3992(78)90057-9.

[96] F. M. Santoyo, M. C. Shellabear, and J. R. Tyrer. Whole field in-plane vibration analysis using pulsed phase-stepped ESPI. *Applied Optics*, 30(7):717–721, 1991. doi: 10.1364/AO.30.000717. URL http://www.ncbi.nlm.nih.gov/pubmed/20582050.

[97] F. M. Santoyo, G. Pedrini, S. Schedin, and H. J. Tiziani. 3D displacement measurements of vibrating objects with multi-pulse digital holography. 10:1305–1308, 1999.

[98] J. Chambard. Pulsed TV-holography recording for vibration analysis applications. *Optics and Lasers in Engineering*, 38(3-4):131–143, October 2002. ISSN 01438166. doi: 10.1016/S0143-8166(02)00006-4. URL http://linkinghub.elsevier.com/retrieve/pii/S0143816602000064.

[99] A. F. Doval. A systematic approach to tv holography. *Measurement Science and Technology*, 11(1):R1, 2000. URL http://stacks.iop.org/0957-0233/11/i=1/a=201.

[100] S. Nakadate. Vibration measurement using phase-shifting speckle-pattern interferometry. *Applied Optics*, 25(22):2810–2816, 1987. doi: 10.1364/AO.26.002810. URL http://www.opticsinfobase.org/abstract.cfm?&id=30500.

[101] M. P. Georges and P. C. Lemaire. Real-time stroboscopic holographic interferometry using sillenite crystals for the quantitative analysis of vibrations, January 1998. ISSN 00304018. URL http://linkinghub.elsevier.com/retrieve/pii/S0030401897004598.

[102] G. M. Brown and G. H. Smith. Dynamic computer aided video holometry, 1990. URL http://dx.doi.org/10.1117/12.962729.

[103] A. J. Moore, D. P. Hand, J. S. Barton, and J. D. Jones. Transient deformation measurement with electronic speckle pattern interferometry and a high-speed

camera. *Applied optics*, 38(7):1159–62, March 1999. ISSN 0003-6935. URL http://www.ncbi.nlm.nih.gov/pubmed/18305726.

[104] C. Ai and J. C. Wyant. Effect of piezoelectric transducer nonlinearity on phase shift interferometry. *Appl. Opt.*, 26(6):1112–1116, Mar 1987. doi: 10.1364/AO.26.001112. URL http://ao.osa.org/abstract.cfm?URI=ao-26-6-1112.

[105] C. Buckberry, M. Reeves, A. J. Moore, D. P. Hand, J. S. Barton, and J. D. C. Jones. The application of high-speed TV-holography to time-resolved vibration measurements. *Optics and Lasers in Engineering*, 32(4):387–394, 2000. URL http://www.sciencedirect.com/science/article/B6V4G-400X0RC-C/2/d52193b5afb08717026746232b48217f.

[106] J. M. Huntley, G. H. Kaufmann, and D. Kerr. Phase-shifted dynamic speckle pattern interferometry at 1 kHz. *Applied optics*, 38(31):6556–6563, 1999. URL http://www.ncbi.nlm.nih.gov/pubmed/18324189.

[107] J. M. Kilpatrick, A. J. Moore, J. S. Barton, J. D. C. Jones, M. Reeves, and C. Buckberry. Measurement of complex surface deformation by high-speed dynamic phase-stepped digital speckle pattern interferometry. *Optics Letters*, 25(15):1068, August 2000. ISSN 0146-9592. URL http://ol.osa.org/abstract.cfm?URI=ol-25-15-1068.

[108] W. N. MacPherson, M. Reeves, D. P. Towers, A. J. Moore, J. D. C. Jones, M. Dale, and C. Edwards. Multipoint laser vibrometer for modal analysis. *Applied Optics*, 46(16):3126, June 2007. ISSN 0003-6935. URL http://ao.osa.org/abstract.cfm?URI=ao-46-16-3126.

[109] M. V. Aguanno. Full-field laser vibrometry employing a novel CMOS-DSP camera. *Proceedings of SPIE*, pages 123–132, 2002. ISSN 0277786X. doi: 10.1117/12.468145. URL http://link.aip.org/link/?PSI/4827/123/1&Agg=doi.

[110] J. Burke, T. Bothe, H. Helmers, C. Kunze, R. S. Sirohi, and V. Wilkens. Spatial Phase shifting in ESPI: Influence of second-order Speckle Statistics on Fringe Quality. *Fringe 97 Automatic Processing of Fringe Patterns*, 97:111–116, 1997.

[111] A. J. Moore and C. P.-Lopez. Fringe carrier methods in double-pulsed addition ESPI. *Optics Communications*, 141(3-4):203–212, 1997. URL http://www.sciencedirect.com/science/article/B6TVF-3SR43PT-1B/2/3d88b9b2476cf9e221b25eef733941f8.

[112] B. B. Garcia, A. J. Moore, C. Perez-Lopez, L. Wang, and T. Tschudi. Spatial phase-stepped interferometry using a holographic optical element. *Optical Engineering*, 38(12):2069–2074, 1999. doi: 10.1117/1.602313. URL http://dx.doi.org/10.1117/1.602313.

[113] B. Barrientos García, A. J. Moore, C. Pérez-López, L. Wang, and T. Tschudi. Transient deformation measurement with electronic speckle pattern interferometry by use of a holographic optical element for spatial phase stepping. *Applied Optics*, 38(28):5944–5947, 1999. URL http://www.ncbi.nlm.nih.gov/pubmed/18324112.

[114] J. Huntley. Random phase measurement errors in digital speckle pattern interferometry. *Optics and Lasers in Engineering*, 26(2-3):131–150, February 1997. ISSN 01438166. doi: 10.1016/0143-8166(95)00109-3. URL http://linkinghub.elsevier.com/retrieve/pii/0143816695001093.

[115] A. Davila, P.D. Ruiz, G.H. Kaufmann, and J.M. Huntley. Measurement of subsurface delaminations in carbon fibre composites using high-speed phase-shifted speckle interferometry and temporal phase unwrapping. *Optics and Lasers in Engineering*, 40(5-6):447–458, November 2003. ISSN 01438166. doi: 10.1016/S0143-8166(02)00082-9. URL http://dx.doi.org/10.1016/S0143-8166(02)00082-9.

[116] A. Davila, J. M. Huntley, G. H. Kaufmann, and D. Kerr. High-speed dynamic speckle interferometry: phase errors due to intensity, velocity, and speckle decorrelation. *Applied Optics*, 44(19):3954, July 2005. ISSN 0003-6935. doi: 10.1364/AO.44.003954. URL http://ao.osa.org/abstract.cfm?URI=ao-44-19-3954.

[117] A. Svanbro, J. M. Huntley, and A. Davila. Optimal re-referencing rate for in-plane dynamic speckle interferometry. *Applied Optics*, 42(2):251–258, 2003. URL http://ao.osa.org/abstract.cfm?URI=ao-42-2-251.

[118] P. D. Ruiz, J. M. Huntley, Y. Shen, C. R. Coggrave, and G. H. Kaufmann. Vibration-induced phase errors in high-speed phase-shifting speckle-pattern interferometry. *Applied Optics*, 40(13):2117–2125, 2001. URL http://www.ncbi.nlm.nih.gov/pubmed/18357218.

[119] P. D. Ruiz, J. M. Huntley, Y. Shen, C. R. Coggrave, and G. H. Kaufmann. Effects of random vibration in high-speed phase-shifting speckle pattern interferometry. *Applied Optics*, 41(19):3941–3949, 2002. URL http://www.ncbi.nlm.nih.gov/pubmed/18224002.

[120] G. Graham, J. N. Petzing, M. Lucas, and J. R. Tyrer. Whole-field modal analysis using electronic speckle pattern interferometry. In P Tomasini Enrico, editor, *Proceedings of SPIE - The International Society for Optical Engineering*, volume 2868, pages 352–361, Washington, DC, USA, 1996. ISBN 0819422649 (ISBN). URL http://www.scopus.com/scopus/inward/record.url?eid=2-s2.0-0030407809&partnerID=40&rel=R5.6.0.

[121] G. Graham, J. N. Petzing, and M. Lucas. Extracting modal parameters of ultrasonic bar horns from ESPI FRF data. *Ultrasonics*, 37(3):231–238, 1999. URL http://www.sciencedirect.com/science/article/B6TW2-3W1B3CN-6/2/6245fcebf9bd506cee1c5b28b03a564f.

[122] G. Graham, J. Petzing, M. Lucas, and J. Tyrer. Quantitative modal analysis using electronic speckle pattern interferometry. *Optics and Lasers in Engineering*, 31(2):147–161, 1999. URL http://www.sciencedirect.com/science/article/B6V4G-3X3THGW-6/2/596d958799c69891c89b7361dfad669b.

[123] H. Van der Auweraer. Structural dynamics modeling using modal analysis: applications, trends and challenges. *IMTC 2001. Proceedings of the 18th IEEE Instrumentation and Measurement Technology Conference. Rediscovering Measurement in the Age of Informatics (Cat. No.01CH 37188)*, pages 1502–1509, 2001. doi: 10.1109/IMTC.2001.929456. URL http://ieeexplore.ieee.org/lpdocs/epic03/wrapper.htm?arnumber=929456.

[124] H. Van Der Auweraer, H. Steinbichler, S. Vanlanduit, C. Haberstok, R. Freymann, D. Storer, and V. Linet. Application of stroboscopic and pulsed-laser electronic speckle pattern interferometry (ESPI) to modal analysis problems. *Review Literature And Arts Of The Americas*, 13:451–463, 2002.

[125] G. Romero, L. Alvarez, E. Alanis, L. Nallim, and R. Grossi. Study of a vibrating plate: comparison between experimental (ESPI) and analytical results. *Optics and Lasers in Engineering*, 40(1-2):81–90, 2003. URL http://www.sciencedirect.com/science/article/B6V4G-45TTN8M-H/2/63157bbd1844c5114c7cb91c690e743a.

[126] A. Giraudeau, B. Guo, and F. Pierron. Stiffness and damping identification from full field measurements on vibrating plates. *Experimental Mechanics*, 46(6):777–787, 2006. URL http://www.scopus.com/scopus/inward/record.url?eid=2-s2.0-33845870398&partnerID=40&rel=R5.6.0.

[127] A. Morrison and T. Rossing. Chladni patterns to holograms: Apparatus for modal analysis of vibrating plates. *Journal of the Acoustical Society of America*, 126(4):2294, 2009.

[128] H. Oztürk and J. G. McDaniel. Spatial mapping of modal damping in vibrating plates. *Journal of the Acoustical Society of America*, 126(4):2244, 2009.

[129] A. Martínez, J. A. Rayas, and R. Cordero. Measurement of in plane strain with shearography and electronic speckle pattern interferometry. In J Buytaert and J Dirckx, editors, *Optical Measurement Techniques for Structures Systems*, volume 7387 of *Speckle 2010: Optical Metrology*, page 73870C (10 pp.). Shaker Publishing, 2010. ISBN 9789042303669. doi: 10.1117/12.870678. URL http://link.aip.org/link/PSISDG/v7387/i1/p73870C/s1&Agg=doi.

[130] S. Earl, T. Wu, J. D. C. Jones, and A. J. Moore. High-speed multipoint vibrometer for modal analysis. In *Proceedings of SPIE - The International Society for Optical Engineering*, volume 6345, Ancona, 2006. ISBN 0277786X (ISSN); 081946421X (ISBN); 9780819464217 (ISBN). URL http://www.scopus.com/scopus/inward/record.url?eid=2-s2.0-33748705417&partner=40&rel=R5.0.4.

[131] S. Earl, T. Wu, J. D. C. Jones, A. J. Moore, (Heriot-Watt University); P. Daborn , A. Tribe, P. Hayden, P. Ind, G. Smith, and (Atomic Weapons Establishment). Impact Testing With a High-speed Multipoint Vibrometer. 2008. URL http://www.sem.org/Proceedings/ConferencePapers-Paper.cfm?ConfPapersPaperID=20174.

[132] I. Bucher. Estimating the ratio between travelling and standing vibration waves under non-stationary conditions. *Journal of Sound and Vibration*, 270(1-2): 341–359, February 2004. ISSN 0022460X. URL http://dx.doi.org/10.1016/S0022-460X(03)00539-X.

[133] R. Gabai and I. Bucher. Excitation and sensing of multiple vibrating traveling waves in one-dimensional structures. *Journal of Sound and Vibration*, 319(1-2):406–425, 2009. ISSN 0022460X. doi: 10.1016/j.jsv.2008.06.013. URL http://www.sciencedirect.com/science/article/B6WM3-4T3CR23-3/2/8e83af7dc6400abd658ceeb780ee2140.

[134] M. Kuribayashi. Excitation conditions of flexural traveling waves for a reversible ultrasonic linear motor. *The Journal of the Acoustical Society of America*, 77 (4):1431, April 1985. ISSN 00014966. doi: 10.1121/1.392037. URL http://link.aip.org/link/?JASMAN/77/1431/1.

[135] B. G. Loh and P. I. Ro. An object transport system using flexural ultrasonic progressive waves generated by two-mode excitation. *IEEE transactions on ultrasonics, ferroelectrics, and frequency control*, 47(4):994–9, January 2000. ISSN 0885-3010. doi: 10.1109/58.852083. URL http://www.ncbi.nlm.nih.gov/pubmed/18238634.

[136] A. Minikes, R. Gabay, I. Bucher, and M. Feldman. On the sensing and tuning of progressive structural vibration waves. *IEEE Transactions on Ultrasonics Ferroelectrics and Frequency Control*, 52(9):1565–1576, 2005. ISSN 08853010. doi: 10.1109/TUFFC.2005.1516029. URL http://www.ncbi.nlm.nih.gov/pubmed/16285455.

[137] K. M. AHMIDA and J. R. F. ARRUDA. On the relation between complex modes and wave propagation phenomena. *Journal of Sound and Vibration*, 255 (4):663–684, August 2002. ISSN 0022460X. doi: 10.1006/jsvi.2001.4183. URL http://dx.doi.org/10.1006/jsvi.2001.4183.

[138] C. W. Lee and M. E. Kim. Use of dFRFs for Separation and Identification of Travelling Wave Modes in Rotating Disk. *Society of Photo-Optical Instrumentation Engineers (SPIE) Conference Series*, 2460:1368, 1995. ISSN 0277-786X. URL http://adsabs.harvard.edu/abs/1995SPIE.2460.1368L.

[139] C. W. Lee and M. E. Kim. Separation and identification of travelling wave modes in rotating disk via directional spectral analysis. *Journal of Sound and Vibration*, 187(5):851–864, November 1995. ISSN 0022460X. doi: 10.1006/jsvi.1995.0568. URL http://dx.doi.org/10.1006/jsvi.1995.0568.

[140] D. J. Ewins A. B. Stanbridge, M. Martarelli. Analysis of Close Mode Shapes Using a Scanning LDV, 2001. URL http://www.sem.org/Proceedings/ConferencePapers-Paper.cfm?ConfPapersPaperID=26553.

[141] J. C. Pascal, X. Carniel, V. Chalvidan, and P. Smigielski. Determination of phase and magnitude of vibration for energy flow measurements in a plate using holographic interferometry. *Optics and Lasers in Engineering*, 25(4-5):343–360, October 1996. ISSN 01438166. doi: 10.1016/0143-8166(95)00080-1. URL http://linkinghub.elsevier.com/retrieve/pii/0143816695000801.

[142] D. Williams M. Reeves, N. Taylor, C. Edwards and C. H. Buckberry. A study of brake disc modal behaviour during squeal generation using high-speed electronic speckle pattern interferometry and near-field sound pressure measurements, 2000. URL http://pid.sagepub.com/cgi/content/long/214/3/285.

[143] P. Carré. Installation et utilisation du comparateur photoélectrique et interférentiel du Bureau International des Poids et Mesures. *Metrologia*, 2 (1):13–23, 1966. ISSN 00261394. doi: 10.1088/0026-1394/2/1/005. URL http://stacks.iop.org/0026-1394/2/i=1/a=005.

[144] J. M. Kilpatrick, A. J. Moore, J. S. Barton, J. D. Jones, M. Reeves, and C. Buckberry. Measurement of complex surface deformation by high-speed dynamic phase-stepped digital speckle pattern interferometry. *Optics letters*, 25 (15):1068–1070, 2000. URL http://www.ncbi.nlm.nih.gov/pubmed/18064273.

[145] D. G. Duffy. *Advanced Engineering Mathematics with MATLAB, Second Edition*. Chapman and Hall/CRC, 2003. URL http://www.amazon.com/Advanced-Engineering-Mathematics-MATLAB-Edition/dp/1584883499.

[146] P. Somers, H. Van Brug. A single camera, dual image real-time-phase-stepped shearing speckle interferometer. In Wolfgang Osten, editor, *Proceedings Fringe 2001*, pages 573–580, Berlin/Heidelberg, 2001. Elsevier (2001). ISBN 3-540-26037-4. doi: 10.1007/3-540-29303-5. URL http://www.springerlink.com/index/10.1007/3-540-29303-5.

[147] J. E. Greivenkamp. Sub-Nyquist interferometry. *Applied Optics*, 26(24):5245, December 1987. ISSN 0003-6935. doi: 10.1364/AO.26.005245. URL http://ao.osa.org/abstract.cfm?URI=ao-26-24-5245.

[148] R. Gabai and I. Bucher. Spatial and Temporal Excitation to Generate Traveling Waves in Structures. *Journal of Applied Mechanics*, 77(2):021010, March 2010. ISSN 00218936. doi: 10.1115/1.3176999. URL http://appliedmechanics.asmedigitalcollection.asme.org/article.aspx?articleid=1474630.

[149] M. J. Connelly, P. M. Szecówka, R. Jallapuram, Suzanne Martin, Vincent Toal, and Maurice P. Whelan. Multipoint laser Doppler vibrometry using holographic optical elements and a CMOS digital camera. *Optics Letters*, 33 (4):330, February 2008. ISSN 0146-9592. doi: 10.1364/OL.33.000330. URL http://ol.osa.org/abstract.cfm?URI=ol-33-4-330.

[150] V. Bavigadda, E. Mihaylova, R. Jallapuram, and V. Toal. Vibration phase mapping using holographic optical element-based electronic speckle pattern interferometry. *Optics and Lasers in Engineering*, 50(8):1161–1167, August 2012. ISSN 01438166. doi: 10.1016/j.optlaseng.2012.01.020. URL http://dx.doi.org/10.1016/j.optlaseng.2012.01.020.